From Computational Mechanics to Computational Control: Automated Control Synthesis for Elastic Tethered Space Systems

Qi Zhang

A Dissertation Submitted To
The Faculty Of Graduate Studies
In Partial Fulfillment Of The Requirements
For The Degree Of

Doctor Of Philosophy

Graduate Program In
Earth And Space Science And Engineering
York University
Toronto, Ontario

June 2026

© Qi Zhang, 2026

Abstract

This dissertation proposes a unified computational framework for the modeling, state estimation, and control of flexible tethered space systems with strongly coupled orbital and structural dynamics. Although these problems are fundamentally interconnected, existing studies have largely addressed them in isolation, and a consistent, scalable framework for treating them in an integrated manner remains unavailable. To fill this gap, this work establishes a finite-element-based framework that unifies high-fidelity dynamic modeling, distributed state estimation, and computational control for advanced tethered space systems.

First, a high-fidelity unified elastic dynamic modeling framework is developed based on the Nodal Position Finite Element Method (NPFEM). By expressing the kinetic and potential energies entirely in terms of finite element nodal positions, the proposed formulation preserves elasticity in both spacecraft and tether components, avoids explicit rigid-body coordinate separation and complex interface constraints, and incorporates orbital disturbance effects directly at the element level. The framework is validated through representative tether mission scenarios, demonstrating its ability to capture strongly coupled orbital-structural responses in large-scale tethered systems.

Second, a robust Finite Element-Kalman (FE-Kalman) state estimation framework is developed for systems with limited sensing. A scalable hybrid measurement model integrates endpoint position and velocity measurements, distributed fiber-optic strain sensing, and model-based virtual sensing. A novel inverse nodal position finite element

method is introduced to reconstruct internal nodal states from strain data. The resulting estimator enables distributed state reconstruction, with observability, stability, and robustness established analytically.

Third, a computational optimal feedback control framework is constructed by integrating the finite element model and FE-Kalman estimator within a moving horizon optimal control formulation. The control problem is posed directly in finite element form and recast, via Hamilton's variational principle, into canonical equations represented as a two-point boundary-value problem with a moving terminal condition. Numerical results demonstrate effective regulation of tether configurations and extensibility to other flexible systems.

Finally, an automated element-level control synthesis methodology is proposed to enable scalable full-order control without reduced-order modeling. Local element controllers are assembled into a global feedback law using standard finite element procedures, preserving nonlinear dynamics while enabling modular implementation. A dual-loop architecture enhances robustness, combining an outer sliding mode controller for reference generation with an inner proportional-derivative tracking loop. Coupled with FE-Kalman state reconstruction, this yields a fully automated pipeline for modeling, estimation, and control. Stability is established using Lyapunov-based analysis, and simulations demonstrate the effectiveness of the proposed approach.

Dedication

I dedicate my dissertation work to my family.

Acknowledgements

It is with profound gratitude that I acknowledge all those whose kindness, guidance, and encouragement have accompanied me throughout the doctoral journey culminating in this dissertation. What began as a research endeavor evolved, over time, into one of the most meaningful chapters of my life, sustained by the generosity and support of many people to whom I remain deeply indebted.

First and foremost, I am profoundly grateful to my supervisor, Professor George Z.H. Zhu, for his rigorous guidance, invaluable insight, and unwavering support throughout the course of this research. His intellectual generosity, exacting standards, and thoughtful mentorship have left an enduring mark on both this dissertation and my development as a scholar.

I also wish to express my sincere appreciation to the members of my supervisory committee, Professor Regina Lee and Professor Jinjun Shan, for their careful reading, constructive criticism, and insightful suggestions. Their expertise and perspectives have greatly strengthened the depth, quality, and clarity of this work.

My gratitude further extends to my colleagues and collaborators in the Space Engineering Design Laboratory, especially Dr. Gangqiang Li, Dr. Junjie Kang, Dr. Chonggang Du, Dr. Dickson Wong, Dr. Weiliang Zhu, Mr. Zhengze Liu, Mr. Fuzhen Yao, Mr. El Ghali Asri, Mr. Jason Li, and many others, for their encouragement and the stimulating discussions that enriched this research experience.

Above all, I am deeply thankful to my family and friends for their love, patience, and unwavering faith in me. Their support sustained me in ways that words cannot fully capture, and this dissertation stands as much as a testament to their devotion as it does to my own perseverance.

Table of Contents

Abstract ii

Dedication iv

Acknowledgements v

Table of Contents vii

List of Tables xii

List of Figures xiii

List of Symbols xx

List of Abbreviations xxv

Chapter 1 Introduction and Justification 1

1.1. Background 1

1.2. Justification of Research 6

1.2.1 Full elastic Dynamic Modeling of Tethered Space Systems 7

1.2.2 Configuration Control of Space Tethers 9

1.3. Objectives of Proposed Research 12

1.4. Methodology of Approach 13

1.5. Outline of Dissertation 16

1.6. List of Publications 17

Chapter 2 Literature Review 20
2.1. Dynamic Modeling of Tethered Space Systems 20
2.2. State Estimation of Flexible Space Tethers 23
2.3. Configuration Control of Flexible Space Tethers 26
Chapter 3 Mathematical Modeling Using Nodal Position Finite Element Method 29
3.1. Description of the Tethered Space System 29
3.2. Tether Element Nodal Position Finite Element Method 31
3.3. Solid Element Nodal Position Finite Element Method 34
3.3.1 Nodal Position Finite Element Method Formulation with Incompatible Mode 34
3.3.2 Numerical Verification of a Cantilevered Regular Beam 46
3.3.3 Numerical Verification of a Twisted Blade 51
3.3.4 Dynamic Analysis of a Rotating Twisted Blade 58
3.4. Full elastic Dynamic Model of the Tethered Space System 64
3.5. Numerical Simulation 65
3.5.1 Steady Orbital Motion of Tethered Spacecraft System .. 65
3.5.2 Dynamic Analysis of Momentum Exchange Tether for Cross-Orbit Payload Delivery 73
3.5.3 Dynamic Analysis of Hub-Spoke Tethered Spacecraft

Formation 82

Chapter 4 Finite Element Kalman State Estimator of Space Tethers..... 91

4.1. Preliminaries..... 91

4.2. Dynamic Model of Space Tethers 93

4.3. Measurement Model 94

4.3.1 Position and Velocity Sensor Model..... 95

4.3.2 FOSS Model..... 95

4.3.3 Virtual Sensor Model 98

4.3.4 Augmented Measurement Model of System 100

4.4. Implementation of State Estimator Algorithm..... 100

4.5. Stability, Observability and Robustness of FE-Kalman State Estimator..... 101

4.5.1 Stability and Observability..... 102

4.5.2 Robustness..... 104

4.6. Simulation and Discussion 105

Chapter 5 Global Computational Control Framework of Space Tethers .. 119

5.1. Preliminaries..... 119

5.2. Computational Feedback Optimal Control..... 121

5.3. Simulation and Discussion 132

Chapter 6 Co-Located Computational Control Framework of Space Tethers

..... 138

6.1. Preliminaries..... 138

6.2. System Model with Disturbance 140

6.3. Design of Element Outer Loop Control..... 141

6.4. Design of Element Inner Loop Control 142

6.5. Controllability Analysis 147

6.6. Stability and Robustness Analysis 148

6.7. Simulation and Discussion 151

6.7.1 Straightening an Initially Bent Space Tether..... 152

6.7.2 Orbit and Attitude Maintenance of Momentum-Exchange Tethers 158

Chapter 7 Conclusion and Future Work..... 166

7.1. General Conclusion..... 166

7.2. Thesis Contribution 167

7.2.1 Unified Elastic Dynamic Model of TSS..... 167

7.2.2 Robust FE-Kalman State Estimator for Flexible Space Tethers 168

7.2.3 Global Computational Control Framework for Flexible Space Tethers 168

7.2.4 Co-Located Computational Control for Flexible Space

Tether 169

7.3. Future work 170

Bibliography 172

List of Tables

Table 3-1 Physical properties and geometric parameters of the rectangular beam..... 46

Table 3-2 The nodal displacement at the tip of the beam. 48

Table 3-3 First three bending modal frequencies of the cantilevered rectangular beam .. 50

Table 3-4 Physical properties and geometric parameters of the blade..... 52

Table 3-5 The nodal displacement of the blade tip (Node 16). 54

Table 3-6 The Von Mises stress of 5 selected nodes. 54

Table 3-7 The first six modal frequencies of the cantilevered blade 55

Table 3-8 Physical parameters of the TSS 66

Table 3-9 Tether's properties 66

Table 3-10 Physical parameters of the momentum exchanged TSS 75

Table 3-11 Physical parameters of the HS-TSF 83

Table 4-1 Physical properties of the flexible tether [49]..... 106

Table 5-1 Physical properties of the TSS..... 132

Table 6-1 Physical parameters of the TSS 151

List of Figures

Figure 1-1 In-orbit tethered space system. Credit: E.T.Pack 2

Figure 1-2 Methodology of approach. 16

Figure 3-1 The finite element discretized model of TSS in orbit. 30

Figure 3-2 Deformation of the two-node tether element. 31

Figure 3-3 Deformation of the eight-node solid element..... 36

Figure 3-4. The boundary and loading conditions of a cantilevered rectangular beam.... 46

Figure 3-5 Convergence of NPFEM with and without incompatible modes..... 49

Figure 3-6 The first three bending modal shapes of the cantilevered rectangular beam. 50

Figure 3-7 Frequency spectrum of flexural vibration of the beam. 51

Figure 3-8 The boundary and loading conditions of a cantilevered blade..... 52

Figure 3-9 The FE mesh of the blade..... 53

Figure 3-10 The nodal displacements U_y in the labelled section of the blade. 54

Figure 3-11 Modal shapes of the blade. The dashed lines represent the undeformed blade. 56

Figure 3-12 The time histories of nodal positions of the blade tip (Node No.17) in the local frame. 57

Figure 3-13 The frequency spectra of the blade tip (Node No.17) subjected to the period tip loads. 58

Figure 3-14 Schematic of a twisted rotating turbine blade 59

Figure 3-15 Time histories of the blade tip's position (Node No. 17) in the global frame. 61

Figure 3-16 Time history of elastic displacement of the blade tip (Node No.17) in the local body-fixed coordinate frame. 62

Figure 3-17 Frequency spectrum of the vibrating blade in the local body-fixed coordinate frame. 63

Figure 3-18 Schematic and discretized model of the TSS. 66

Figure 3-19 Time histories of orbital altitude variation and out-of-plane motion of spacecraft and mid-node of the tether: (a) Main spacecraft; (b) Sub spacecraft; (c) Mid-node of the tether. 68

Figure 3-20 Time histories of attitudes of the main spacecraft in ECI frame. 70

Figure 3-21 Time histories of attitudes of the sub spacecraft in the ECI frame. 70

Figure 3-22 Time histories of the tether length. 71

Figure 3-23 Tether tension of each tether element. 72

Figure 3-24 Time histories of the von Mises stress at the connection nodes between the

tether and spacecraft: (a) Connection node between the tether and main spacecraft; (b) Connection node between the tether and sub spacecraft..... 73

Figure 3-25 The schematic and the discretized model of momentum-exchange tethers.. 75

Figure 3-26 Time histories of orbital altitude variation and out-of-plane motion of Node C on the main spacecraft, Mid-node of the tether and the mass point of the sub spacecraft. 77

Figure 3-27 Time histories of the attitudes of the main spacecraft in ECI frame. 78

Figure 3-28 Time histories of the angular velocities of the main spacecraft in ECI frame. 78

Figure 3-29 Time histories of the tether length. 80

Figure 3-30 Tether tension of each tether element. 80

Figure 3-31 Time histories of the von Mises stress at the connection nodes between the tether and spacecraft. 81

Figure 3-32 Tether configurations at different time instants after payload release. 81

Figure 3-33 The schematic and the discretized model of HS-TSF. 82

Figure 3-34 Time histories of the orbital altitude variation and out-of-plane motion of the center of mass on the central spacecraft. 85

Figure 3-35 Time histories of the spin angles of the central hub. 86

Figure 3-36 Time histories of the spin rates of the central hub. 86

Figure 3-37 Time histories of the length of each tether. 87

Figure 3-38 Tether tension of each tether element. 89

Figure 3-39 Time histories of the von Mises stress at the connection nodes between the tethers and the central hub. 90

Figure 3-40 The configuration of HS-TSF at different time instants. 90

Figure 4-1 Schematic of the discretized FE model and states. 93

Figure 4-2 Flowchart of the state estimation algorithm. 101

Figure 4-3 The schematic diagram of TSS model. 106

Figure 4-4 Comparison of position estimation at the 3rd node: (a) *X*-Axis (b) *Y*-Axis. . 107

Figure 4-5 Comparison of position estimation at the 5th node: (a) *X*-Axis (b) *Y*-Axis. . 108

Figure 4-6 Comparison of position estimation at the 7th node: (a) *X*-Axis (b) *Y*-Axis. . 108

Figure 4-7 Comparison of velocity estimation at the 3rd node: (a) *X*-Axis (b) *Y*-Axis. . 109

Figure 4-8 Comparison of velocity estimation at the 5th node: (a) *X*-Axis (b) *Y*-Axis. ..110

Figure 4-9 Comparison of velocity estimation at the 7th node: (a) *X*-Axis (b) *Y*-Axis. ..110

Figure 4-10 Errors of the current and reference method in different directions. 112

Figure 4-11 Comparison of position estimation errors of the 3rd node by the previous method and the proposed method in different directions. 113

Figure 4-12 Comparison of position estimation errors of the 5th node by the previous method and the proposed method in different directions. 114

Figure 4-13 Comparison of position estimation errors of the 7th node by the previous method and the proposed method in different directions. 115

Figure 4-14 Comparison of velocity estimation errors of the 3rd node by the previous method and the proposed method in different directions. 116

Figure 4-15 Comparison of velocity estimation errors of the 5th node by the previous method and the proposed method in different directions. 117

Figure 4-16 Comparison of velocity estimation errors of the 7th node by the previous method and the proposed method in different directions. 118

Figure 5-1. Evolution diagram of global computational control. 120

Figure 5-2. Schematic diagram of the TSS model. 121

Figure 5-3 Flowchart of the implementation of computational optimal control with state estimator. 131

Figure 5-4 The initial and desired geometrical profiles of the flexible tether. 133

Figure 5-5 Geometric profiles of the tether with and without control at different time instances. 134

Figure 5-6 Time histories of the position error of Main spacecraft (Node 1). 135

Figure 5-7 Time histories of the position error of Sub spacecraft (Node 5). 135

Figure 5-8 Time histories of the position error of the mid-node..... 136

Figure 5-9 Time history of tether tension. 137

Figure 5-10 Time history of control input..... 137

Figure 6-1 Evolution diagram of the co-located computational control. 139

Figure 6-2 Schematic of the TSS in space. 140

Figure 6-3 Schematic of computational control framework. 146

Figure 6-4 Initial and desired tether geometric configurations. 153

Figure 6-5 Tether configurations at different time instances with and without control input. 155

Figure 6-6 Main spacecraft position error in the global frame. 156

Figure 6-7 Sub spacecraft position error in the global frame. 156

Figure 6-8 Mid-node position error in the local frame. 157

Figure 6-9 Time histories of tether tension in tether elements under computational control. 157

Figure 6-10 Time histories of computational control input at the main spacecraft and sub spacecraft. 158

Figure 6-11 Spinning tether geometric configurations. 159

Figure 6-12 The trajectory of tether motion under the computational controller. 161

Figure 6-13 Tether configurations at different time instants with and without control. . 162

Figure 6-14 Main spacecraft position error in the global frame. 163

Figure 6-15 Sub spacecraft position error in the global frame. 163

Figure 6-16 Mid-node position error in the local frame. 164

Figure 6-17 Time histories of tether tension of each element. 165

Figure 6-18 Time histories of control input at the main spacecraft and sub spacecraft.. 165

List of Symbols

$\boldsymbol{A}_d$ = State transition matrix

A_t = Cross-sectional area of space tethers

$\boldsymbol{B}$ = Control mapping matrix

$\boldsymbol{B}_d$ = State mapping matrix

$\boldsymbol{B}_s$ = Total strain matrix (spacecraft)

$\boldsymbol{B}_{s,L}$ = Linear strain matrix of (spacecraft)

$\boldsymbol{B}_{s,N}$ = Nonlinear strain matrix of (spacecraft)

$\boldsymbol{B}_t$ = Strain matrix in the global frame (Space tether)

$\boldsymbol{B}_t^0$ = Strain matrix of in the local frame (Space tether)

$\boldsymbol{C}$ = Damping matrix of tethered space systems

$\boldsymbol{C}_s$ = Damping matrix of the spacecraft

$\boldsymbol{C}_t$ = Damping matrix of space tether

$\boldsymbol{d}$ = Bounded disturbance of the system

$\boldsymbol{D}_s$ = Elastic coefficient matrix (spacecraft)

$\boldsymbol{e}$ = Tracking error

$\boldsymbol{e}_0$ = Initial position errors

E_s = Young's modulus of the spacecraft material

E_t = Young's modulus of tether material

$\boldsymbol{F}^0$ = Equivalent elastic force of tethered space system

$\boldsymbol{F}_{s,K}^0$ = Equivalent elastic force accounting for incompatible shape functions for flexural bending modes

$\boldsymbol{F}_t^0$ = Equivalent elastic force of space tethers

$\boldsymbol{F}^{ext}$ = External force vector of tethered space systems

$\boldsymbol{F}_s^e$ = External force applied on spacecraft

$\boldsymbol{F}_t^e$ = External force of space tether

$\boldsymbol{F}^d$ = Atmospheric drag force applied to tethered space systems

$\boldsymbol{F}_t^d$ = Atmospheric drag force applied to space tethers

$\boldsymbol{F}^g$ = Gravity force applied to tethered space systems

$\boldsymbol{F}_t^g$ = Gravity force applied to space tethers

$\boldsymbol{H}$ = Observation matrix

$\boldsymbol{J}_s$ = Transformation Jacobian matrix (spacecraft)

$\boldsymbol{K}$ = Stiffness matrix of tethered space systems

$\boldsymbol{K}^d$ = Differential control gain matrix

$\boldsymbol{K}_t^{inv}$ = Inverse stiffness matrix (space tether)

$\boldsymbol{K}^p$ = Proportional control gain matrix

K_i^s = Switching gain of the sliding mode controller

$\boldsymbol{K}_s$ = Stiffness matrix of the spacecraft

$\boldsymbol{K}_t$ = Stiffness matrix of space tethers

L_t = Instantaneous length of space tethers

L_{t0} = Original length of space tethers

$\boldsymbol{M}$ = Mass matrix of tethered space systems

$\boldsymbol{M}_s$ = Mass matrix of the spacecraft

$\boldsymbol{M}_t$ = Mass matrix of space tethers

$\boldsymbol{N}_s$ = Shape function (spacecraft)

$\boldsymbol{N}_t$ = Shape function (space tether)

$\boldsymbol{Q}_s$ = Coordinate translation matrix (solid element)

$\boldsymbol{Q}_t$ = Coordinate transformation matrix (Rod element)

$\overline{\boldsymbol{r}}_s$ = Position vector of an arbitrary point P (spacecraft)

$\boldsymbol{s}$ = Sliding surface

t = time

T_t = Kinetic energy of space tethers

$\boldsymbol{u}_t$ = Control input

U_s = Strain energy (spacecraft)

$\boldsymbol{U}_s$ = Displacement vector of the spacecraft in the local frame

U_t = Strain energy of space tethers

V = Lyapunov function

$\tilde{\boldsymbol{V}}$ = Measurement noise

$\tilde{\boldsymbol{W}}$ = Model noise

$\tilde{\boldsymbol{X}}$ = State vector

$\boldsymbol{X}^d$ = Desired trajectory

$\boldsymbol{X}^r$ = Reference trajectory generated by the outer loop controller

$\bar{\boldsymbol{X}}_s$ = Vector of the nodal coordinates of the undeformed spacecraft

$\boldsymbol{X}_t$ = Vector of the nodal coordinates of space tether

$\boldsymbol{X}_t^M$ = Estimated position vector of internal nodes of space tethers

$\boldsymbol{Y}$ = Vector of the measured state

$\boldsymbol{\alpha}_s$ = Parameter vector of the incompatible displacement modes

Δt = Time step

$\boldsymbol{\varepsilon}_s$ = Green-Lagrangian strain of (solid element)

$\boldsymbol{\varepsilon}_t$ = Green-Lagrangian strain (rod element)

ε_t^M = Average of the measured strain vector

ν_s = Poisson's ratio of the spacecraft material

ξ_s = Natural coordinates (spacecraft)

ξ_t = Natural coordinates (space tether)

ρ_s = Density of the spacecraft material

ρ_t = Density of the tether material

List of Abbreviations

1D	=	1-Dimensional
3D	=	3-Dimensional
ALE	=	Arbitrary Lagrangian–Eulerian
ANCF	=	Absolute Nodal Coordinate Formulation
ECI	=	Earth-Centered Inertial
DAE	=	Differential Algebraic Equation
FEM	=	Finite Element Method
FE-Kalman	=	Finite Element-Kalman
FOSS	=	Fiber Optic Sensing System
HS-TSF	=	Hub-Spoke Tethered Spacecraft Formations
iNPFEM	=	inverse Nodal Position Finite Element Method
NPFEM	=	Nodal Position Finite Element Method
PBH	=	Popov-Belevitch-Hautus
PD	=	Proportional-Derivative
PID	=	Proportional-Integral-Derivative

ROM	=	Reduced-Order Model
SMC	=	Sliding Mode Control
TPBVP	=	Two-Point Boundary Value Problem
TSS	=	Tethered Space Systems

Chapter 1 INTRODUCTION AND JUSTIFICATION

Summary: This chapter introduces the background to dynamics and control of tethered space systems. It then presents the motivation for the research and summarizes the research objectives and methodologies. Finally, it outlines the structure of the dissertation and provides a complete list of publications resulting from this doctoral research.

1.1. Background

As shown in Figure 1-1, a space tether is a long and flexible cable, typically fabricated from high-strength fibers, that is used to mechanically connect spacecraft or other orbital bodies [1]. Through this mechanical linkage, energy and momentum can be directly exchanged between the connected masses. Space tethers are characterized by extremely large aspect ratios, with lengths ranging from several hundred meters to tens of kilometers while maintaining very small cross-sectional diameters. This structural configuration enables tethered systems to span large distances in orbit while contributing relatively little mass to the spacecraft system.

The conceptual origin of tethered space structures can be traced back more than a century. The conceptual foundation of space tethers dates back to 1895, when Konstantin Tsiolkovsky first proposed a Celestial Castle connected to Earth by a long cable [2], which later evolved into tensile space elevator concepts proposed during the 1960s [3]. Significant developments in tether research occurred in the 1970s, when the orbital mechanics of

gravity-gradient stabilized tether systems were formally established, and their electrodynamic interactions with the space environment were investigated [4]. Since then, tether technology has been studied extensively as a means of enabling novel space operations that exploit the mechanical coupling between orbiting bodies. [5–8]



Figure 1-1 In-orbit tethered space system. Credit: E.T.Pack

In recent years, tethered space systems (TSS) have attracted increasing attention in the context of On-Orbit Servicing (OOS) and other advanced space missions. TSS configurations have been investigated for a range of applications [9,10], including orbital maneuvering [11–14], space debris removal [15–18], artificial gravity generation [19–22], satellite formation flying [23–26], and cross-orbital payload transfer without relying on conventional propulsion systems [27–30]. By exploiting their extended spatial scale, TSS can interact with gravitational, aerodynamic, and electromagnetic forces in ways that

enable propellant-efficient mission architectures [31]. These potential applications have motivated extensive studies on the dynamics and control of TSS.

From a dynamical perspective, a tethered space system typically consists of two or more rigid bodies connected by a long, flexible tether, forming a coupled orbital–structural dynamical system. During operation, the end masses follow orbital trajectories, while the tether undergoes elastic deformation, leading to strong coupling between rigid-body motion and flexible structural dynamics. A typical mission profile includes tether deployment, station-keeping, and tether retrieval phases, each of which involves different dynamic characteristics associated with tether motion, tension variation, and libration behavior.

The dynamics of flexible tethers used to be described using distributed-parameter models, where the tether is treated as a continuous elastic body governed by nonlinear partial differential equations [32]. These formulations capture the propagation of longitudinal and transverse waves along the tether and describe the coupling between deformation, tension, and orbital motion. However, in practical orbital environments, system dynamics are further influenced by external perturbations such as Earth's oblateness, atmospheric drag in low Earth orbit, solar radiation pressure, and gravitational perturbations from other celestial bodies. These effects can modify the orbital motion of the end masses and introduce additional excitation to the tether structure, thereby affecting the tension distribution and vibration characteristics of the system. Since analytical solutions of the governing equations are generally not available under such conditions,

numerical modeling approaches are widely used for dynamic analysis and simulation. One commonly used approach is the lumped-mass model, in which the tether is discretized into a sequence of point masses connected by massless springs or viscoelastic elements [33–35]. This representation provides a computationally efficient description of the primary stretching dynamics of the tether. Another widely adopted approach is the finite element method (FEM), where the tether is discretized into beam or rod elements capable of representing axial deformation, bending, and torsional effects [36–38]. In addition, multibody dynamic formulations treat the tether as a chain of interconnected rigid rods, enabling the system to be analyzed within a general multibody dynamics framework [39]. More advanced continuum descriptions based on geometrically exact rod theories, such as Cosserat rod formulations, have also been used to capture large deformations and nonlinear coupling effects [40]. These modeling approaches provide the foundation for predicting tether motion, tension distribution, and vibration behavior under various operational conditions.

In parallel with the development of dynamic models, substantial research has been devoted to the control of TSS to regulate system motion and maintain stable operation during different mission phases. Control strategies are typically designed to achieve objectives such as controlled tether deployment and retrieval, suppression of tether libration, attenuation of structural vibrations, and precise orbital maneuvering. Because TSS possess many degrees of freedom while actuation is generally limited to the tether end, control approaches are formulated to regulate the coupled orbital–structural dynamics

using a relatively small number of control inputs. A variety of control methodologies have been investigated for tether applications. Linear control approaches, including Proportional-Integral-Derivative (PID) control [41] and LQR designs [42], have been used to regulate small oscillations around equilibrium configurations obtained through system linearization. For systems exhibiting stronger nonlinear behavior, nonlinear control techniques have been widely studied. For example, sliding mode control (SMC) has been applied to tether systems as a robust control strategy capable of maintaining stability in the presence of disturbances and modeling uncertainties [43–45]. The State-Dependent Riccati Equation (SDRE) approach [46] provides a systematic framework for nonlinear optimal control and has been used to regulate tether libration and trajectory motion. In addition, adaptive control methods have been developed to accommodate uncertainties in system parameters [47], while energy-based control strategies have been employed to reduce oscillatory motion and regulate tether tension during deployment and retrieval operations [48]. These control methodologies provide effective tools for maintaining system stability and ensuring desired dynamic performance in tethered satellite missions.

Another important aspect of TSS research concerns state estimation and system monitoring. In practical missions, sensors are typically installed on the end masses, while measurements along the tether itself are generally unavailable. As a result, the internal dynamic states of the tether cannot be directly measured. To address this limitation, observer-based estimation techniques have been developed to reconstruct quantities such as tether tension, vibration states, and libration angles using limited measurement data

[49,50]. These estimation methods provide essential information for feedback control and system monitoring, contributing to the reliable operation of TSS.

1.2. Justification of Research

A typical TSS consists of two spacecraft interconnected by a flexible tether and exhibits highly complex dynamic behavior arising from the strong coupling of orbital motion, tether elasticity, and environmental disturbances. The reliable operation of TSS is fundamentally impeded by a series of challenges inherent in the tether's distinctive structural characteristics. Specifically, the tether's continuous elasticity, extreme slenderness, and capacity for large deformation render conventional rigid–flexible modeling frameworks, which depend on artificially imposed constraints, inadequate for ensuring numerical robustness and for accurately capturing high-frequency flexible dynamics. Concurrently, the tether's large spatial extent and slender geometry make dense distributed sensing impractical, thereby precluding the direct measurement and real-time feedback of the internal states of tether nodes. Consequently, control design cannot be founded on high-fidelity full-state information and must instead rely on limited endpoint measurements and reduced-order representations, both of which are highly susceptible to noise, model uncertainty, and spillover effects arising from neglected flexible modes. For an underactuated system characterized by infinitely many vibration modes, these limitations can readily excite unmodeled high-frequency dynamics, thereby inducing unstable librational motion and severe tension oscillations. Taken together, these

interconnected challenges underscore the absence of a unified framework capable of consistently supporting high-fidelity modeling, effective state estimation, and robust control of TSS. To address this gap, this dissertation develops a modular unified framework for modeling, state estimation, and computational control, thereby enabling the accurate, scalable, and robust operation of tethered spacecraft under realistic orbital conditions.

1.2.1 Full elastic Dynamic Modeling of Tethered Space Systems

1.2.1.1 Challenges

The motion of TSS involves strong coupling among large rigid-body orbital dynamics, tether elastic deformation, and various environmental disturbances, which poses significant challenges for accurate modeling and dynamic analysis.

(i) **Inherent nonlinearity**: The dynamics of TSS exhibits pronounced nonlinear behavior arising from state-dependent tether tension, large geometric deformations, and strong coupling between spacecraft attitude and orbital motion. Energy exchange between tether libration and orbital dynamics can produce complex responses, including large-amplitude oscillations, parametric resonance, and, under certain conditions, chaotic motion.

(ii) **High-dimensional flexible dynamics**. Long space tethers behave as distributed flexible continua rather than rigid connectors. Accurate representation of axial elasticity, bending deformation, and wave propagation along the tether generally requires high-fidelity spatial discretization techniques, such as FEM. These

approaches substantially increase the dimensionality of the governing equations and consequently raise the computational cost of dynamic simulations.

(iii) **Rigid–Flexible dynamic coupling**: Tethered spacecraft systems are highly coupled multibody systems consisting of massive end bodies connected by a compliant tether. Accurate dynamic modeling therefore requires rigid–flexible coupling formulations that satisfy kinematic compatibility and dynamic equilibrium at the tether–spacecraft interfaces. Such formulations often result in large systems of Differential Algebraic Equations (DAEs), which increase computational complexity and may reduce numerical robustness in long-duration simulations. In addition, neglecting the structural flexibility of the spacecraft components can further diminish model fidelity.

1.2.1.2 Limitations of Existing Studies

Existing research on TSS has gradually evolved from simplified rigid-body representations to more refined flexible formulations, thereby improving the ability to describe tether deformation and vibration effects. This progression has provided a stronger foundation for understanding the complex dynamic behavior of space tethers under realistic operating conditions. Owing to the strong nonlinearity of tether motion, the complexity of boundary conditions, and the influence of environmental disturbances, however, high-fidelity analysis generally relies on numerical discretization methods rather than closed-form analytical solutions. Within such numerical frameworks, the tether is commonly

modeled as a flexible body, whereas the connected spacecraft are still represented as rigid bodies, leading most existing studies to adopt a rigid–flexible coupling strategy. Although this treatment is computationally practical and has supported a wide range of dynamic analyses, it does not provide a fully consistent representation of the structural flexibility of the entire system. In particular, the interaction between tether elasticity and spacecraft deformation cannot be captured within a unified formulation, and compatibility between components often needs to be introduced through additional constraints, which increase computational complexity and may reduce numerical robustness in long-duration simulations. ***As a result, the capability of current models to characterize the coupled dynamics and load transfer of increasingly large, lightweight, and flexible spacecraft remains limited***, which suggests the necessity of developing a unified full elastic modeling framework for TSS.

1.2.2 Configuration Control of Space Tethers

1.2.2.1 Challenges

Discrete tether models have been developed to represent tether dynamics with greater fidelity by discretizing the tether into interconnected rigid rods, elastic links, or finite elements. While these models improve physical realism, they also introduce substantial control challenges arising from high dimensionality, strong nonlinear coupling, distributed flexibility, underactuation, and sensitivity to environmental disturbances. Collectively, these characteristics complicate state estimation, controller design, stability assurance, and

real-time implementation. The main control design challenges can be summarized as follows.

(i) **State estimation for distributed systems**: State estimation in TSS is challenging due to their distributed and high-dimensional nature. Many internal states, including tether deformation and tension distributions, cannot be measured directly in space. In addition, limited sensing and communication capabilities restrict the availability of real-time measurements. Consequently, accurate reconstruction of the full state is difficult, posing significant challenges for the implementation of reliable feedback control, guidance, and navigation strategies.

(ii) **Underactuated system**: TSS are inherently underactuated, as control inputs are generally applied only at the tethered spacecraft through actuators such as thrusters, reaction wheels, or tether length control mechanisms, while the tether itself has no distributed actuation capability. Consequently, a large number of internal degrees of freedom must be regulated using a limited number of control inputs. This structural underactuation considerably increases the difficulty of stabilization and trajectory tracking, particularly for tether configuration regulation and suppression of distributed vibration modes.

(iii) **Uncertainty**: The dynamics of tethered spacecraft systems are subject to significant uncertainties arising from both environmental disturbances and imperfect knowledge of system parameters. External perturbations, such as atmospheric drag, gravity-gradient effects, solar radiation pressure, and

electrodynamic interactions, may introduce distributed disturbances along the tether. Meanwhile, uncertainties in tether material and geometric properties, as well as modeling errors associated with spatial discretization, can lead to discrepancies between the mathematical model and the actual system behavior. These uncertainties complicate controller design and highlight the need for robust control strategies capable of ensuring stability and satisfactory performance.

1.2.2.2 Limitations of Existing Studies

Many studies have investigated the control of TSS, advancing the regulation of tether deployment, retrieval, and attitude motion and establishing a solid theoretical foundation for TSS control. However, the effectiveness of many existing approaches remains dependent on simplified dynamic models that do not fully represent the physical behavior of practical tethered systems. In realistic operations, tether elasticity, slack–taut transitions, underactuation, and tension saturation introduce strong nonlinearities and constraints that significantly affect system response and control performance. To capture these effects, high-fidelity finite element models have been developed, but their discretized nature leads to large-scale systems with many degrees of freedom, which greatly increases the difficulty of controller synthesis. This challenge is further compounded by the limited availability of distributed sensing along the tether, making full-state feedback difficult to realize in practice. Although reduced-order models (ROMs) are often employed to simplify controller design, they may not preserve the essential flexible dynamics of the original

system under varying operating conditions. Consequently, the development of a control framework that can be applied directly to high-fidelity discretized TSS models while accommodating limited sensing and the flexible dynamics of the tethers remains an important unresolved issue.

1.3. Objectives of Proposed Research

To address the existing challenges and limitations in TSS, this dissertation investigates advanced methodologies for dynamic modeling, state estimation, and control. The main research objectives are as follows:

(i) Develop a novel 8-node isoparametric hexahedral element within the Nodal Position Finite Element Method (NPFEM) for the elastodynamic analysis of rotating solids, including high-speed rotating wind-turbine blades and low-speed rotated spacecraft.

(ii) Establish a high-fidelity, unified, full elastic NPFEM model for TSS, in which both the tether and spacecraft are modeled within a single finite element framework, thereby avoiding complex interface constraints and coordinate transformations.

(iii) Develop a state estimation methodology for flexible space tethers by fusing position and velocity measurements with fiber optic sensing systems (FOSS) and virtual sensors.

(iv) Formulate a computational control framework for flexible space tethers with actuation applied only at the tether-end spacecraft, integrating finite element

modeling, state estimation, and optimal receding-horizon control.

(v) Introduce an automated element-level computational control synthesis framework, inspired by the FEM, in which local controllers are designed at the element level and assembled into a global feedback law through the standard finite element assembly process.

Accordingly, this dissertation presents a modular, unified framework encompassing modeling, state estimation, and control, enabling accurate, scalable, and robust operation of TSS under realistic orbital conditions.

1.4. Methodology of Approach

This dissertation begins with the development of a dynamic modeling framework for TSS, which provides the foundation for subsequent state estimation and control design. In contrast to conventional rigid-flexible formulations, in which the tether is modeled as elastic and the spacecraft as rigid bodies, the proposed approach retains elasticity in both the tether and the spacecraft within a unified finite element formulation. This unified representation eliminates the need for complex enforcement of interface constraints and avoids cumbersome coordinate transformations that separate global rigid-body motion from local elastic deformation, thereby establishing a consistent computational basis for system analysis, observation, and control.

Building upon this modeling framework, a state estimation methodology is developed for space tethers. In such systems, many internal states, particularly the distributed

deformation and tension along the tether, are not directly measurable, while available measurements are typically limited to the system boundaries. This incomplete measurability poses a fundamental challenge for accurate state reconstruction. To address this issue, heterogeneous measurements are integrated, including position and velocity data at the tether endpoints and distributed strain measurements obtained from fiber-optic sensors along the tether. These measurements are incorporated into a finite element-based Kalman filtering framework, in which the system dynamics are formulated directly in the finite element domain. By leveraging the spatial discretization inherent in the finite element model, the estimator systematically fuses measurement data with the underlying dynamics to reconstruct both nodal states and distributed deformation. The resulting formulation is inherently modular and scalable, and is shown to satisfy key properties including observability, stability, and robustness with respect to measurement noise and modeling uncertainties.

Based on the observed or estimated states, two computational control frameworks are developed to achieve configuration regulation of flexible space tethers. The first is a unified computational feedback control framework formulated entirely within the finite element domain, integrating system dynamics, state estimation, and moving horizon optimal control into a single computational procedure. The control objective is to regulate the geometric configuration of the tether, with the optimal control problem posed directly in finite element form. By invoking Hamilton's variational principle, the problem is transformed into a system of canonical equations, leading to a two-point boundary value

problem (TPBVP) with a moving terminal boundary condition. The control inputs are computed numerically from the canonical equations and implemented in closed-loop form using a moving horizon strategy.

The second framework adopts a modular structure that enables systematic controller synthesis in the finite element domain through an algorithmic procedure analogous to that used in computational mechanics. This approach facilitates automated, system-level controller design for space tethers, where conventional methods are often difficult to apply. To enhance robustness, a dual-loop control architecture is introduced, in which an outer-loop sliding-mode controller generates robust element-wise reference trajectories and an inner-loop PD controller ensures trajectory tracking. Using the estimated system states as feedback, the framework achieves robust tether configuration regulation in the presence of external disturbances. Stability and robustness are rigorously established through Lyapunov-based analysis, and the framework is seamlessly integrated with a high-fidelity finite element model for application to complex tethered spacecraft configurations.

Finally, as shown in Figure 1-2, by organizing dynamic modeling, state estimation, and control within a unified and modular computational architecture, this dissertation establishes a comprehensive methodology for the analysis and regulation of tethered spacecraft systems. The resulting framework enables accurate, scalable, and robust operation, and is demonstrated through high-fidelity simulations of representative tethered spacecraft missions.

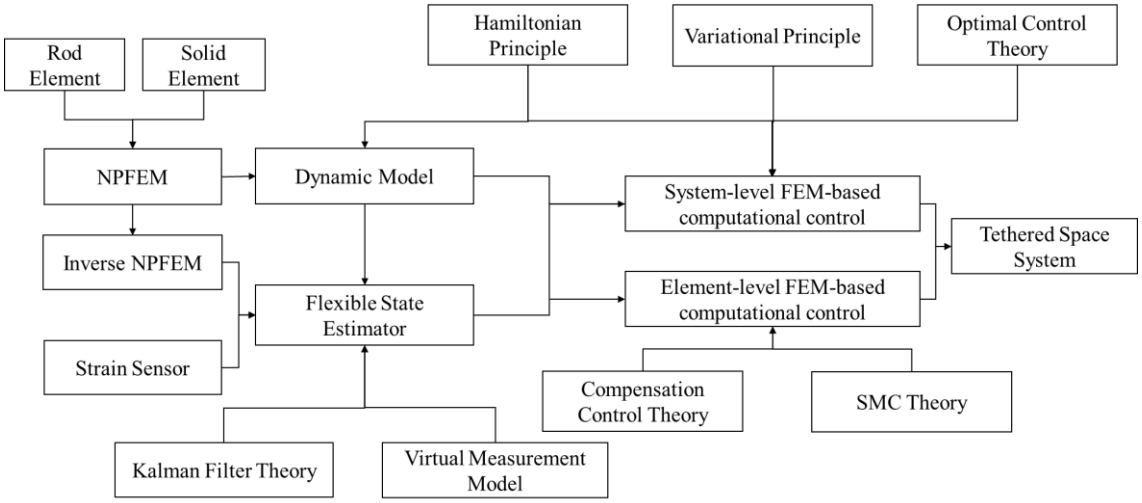

Figure 1-2 Methodology of approach.

1.5. Outline of Dissertation

This dissertation is organized into seven chapters. Chapter 1 introduces the research background, motivation, and significance of the study. Chapter 2 presents a comprehensive review of the literature on dynamic modeling and control of tethered spacecraft systems. Chapter 3 develops a high-fidelity, unified, full elastic dynamic model for TSS based on the 1D and 3D NPFEM. Chapter 4 presents a state estimation approach for flexible space tethers by integrating position and velocity measurements at the tether ends, distributed fiber-optic strain measurements along the tether, and estimated position and velocity information obtained through a finite element-based Kalman filter. Chapter 5 investigates the optimal control problem formulated based on the finite element model of space tethers. Chapter 6 develops an automated element-level computational control synthesis framework that emulates the NPFEM by constructing local controllers for individual

elements and assembling them into a system-level feedback law through standard finite element assembly procedures. Chapter 7 concludes the dissertation by summarizing the major contributions of the research and identifying promising directions for future work.

1.6. List of Publications

The thesis has resulted in the following eight peer-reviewed journal papers and three conference papers.

Peer-reviewed Journal Papers:

(1) **Zhang Qi**, Asri El Ghali, Zhu Zheng H. Space tether system state estimation using distributed fibre optical strain measurement, inverse finite element method and Kalman filter. Acta Astronautica 2023;211:435–46.
DOI: 10.1016/j.actaastro.2023.06.020.

(2) **Zhang Qi**, Zhu Zheng H. Elastodynamic analysis of rotating solids by novel nodal position finite element method. European Journal of Mechanics - A/Solids 2025;109:105478.
DOI: 10.1016/j.euromechsol.2024.105478.

(3) **Zhang Qi**, Zhu Zheng H. Computational control framework for tethered space systems using finite element method. Acta Astronautica 2025;228:595–606.
DOI: 10.1016/j.actaastro.2024.12.013.

(4) Liu Zhengze, **Zhang Qi**, Zhu George Z. H. A comprehensive review on computational control. Trans Can Soc Mech Eng 2026;50:1–16.

DOI: 10.1139/tcsme-2025-0049.

(5) Zhu Weiliang, Liu Zhengze, **Zhang Qi**, Pang Zhaojun, Zhu Zheng H. Development of pseudo-celestial navigation and tracking system for planar air-bearing satellite simulators. Aerospace Science and Technology 2026;169:111462.

DOI: 10.1016/j.ast.2025.111462.

(6) **Zhang Qi**, Zhu Zheng H. Co-located Finite Element Modeling and Computational Control for Tethered Space Systems. Chinese Journal of Aeronautics 2026. (In press)

(7) **Zhang Qi,** Zhu ZH. Orbital-Structural Coupling Effects in Tethered Space Systems Using Unified Elastic Dynamic Modeling. Aerospace Science and Technology. 2026; 113105.

DOI: https://doi.org/10.1016/j.ast.2026.113105

(8) Yao Fuzhen, **Zhang Qi**, Zhu Zheng H. Near-surface lunar observation by tethered orbital platform for high-resolution long-duration exploration. Acta Astronautica 2026;246:778–83. DOI: 10.1016/j.actaastro.2026.04.047.

Conference Papers and Presentations:

(1) **Zhang Qi ,** Zhu Zheng H. Computational control framework for flexible cable based on finite element methods. In *Canadian Society for Mechanical Engineering Congress*, Toronto, Canada, 2024.

(2) **Zhang Qi ,** Zhu Zheng H. Computational control for flexible cable systems with a finite element state estimator. In *The 7th International Conference on Tethers in Space*, Toronto, Canada, 2024.

(3) Zhang Qi, Zhu Zheng H. Deployment Dynamics of a Spinning Hub–Spoke Tethered Spacecraft Formation Using Arbitrary Lagrange–Euler Nodal Position Finite Element Method. In *The Fifth International Nonlinear Dynamics Conference*, Roma, Italy, 2026. (Accepted)

Chapter 2 LITERATURE REVIEW

Summary: This chapter presents a comprehensive literature review of TSS dynamic modeling, state estimation, and control. It examines the major research developments in these areas and highlights the methods most relevant to the present study.

2.1. Dynamic Modeling of Tethered Space Systems

The practical implementation of TSS remains challenging due to strong nonlinear orbital-structural coupling. This coupling involves tight interactions among large rigid-body orbital motion, tether elastic deformation, and environmental disturbances, complicating accurate modeling and dynamic analysis.

Early studies of TSS commonly idealized the tether as a rigid, massless link and the spacecraft were modelled as lumped point masses, leading to the well-known dumbbell model [51,52]. Although this simplified representation is adequate for analyzing basic tethered motions, such as deployment, momentum exchange, and formation flying, it cannot capture crucial orbital-structural coupling effects, including tether elastic elongation and longitudinal and lateral vibration, that are essential to stable and reliable system operation. To improve model fidelity, flexible tether formulations were subsequently developed to account for tether elasticity, such as the continuous string model governed by partial differential equations [53]. However, analytical solutions for this highly nonlinear model are generally infeasible due to strong nonlinearities, complex boundary conditions,

orbital-structural coupling, and environmental perturbations.

To overcome these difficulties, numerical methods based on discretized tether representations have been developed. These methods typically employ discrete tether models in which the tether motion is described by nodal positions. One early example is the bead-string model and/or mass-spring-dashpot model [54] that approximates the tether as a sequence of lumped masses connected by elastic springs and dashpots, enabling the capture of both longitudinal oscillations and lateral vibrational modes of tethers. Building on this idea and the generality of FEM, NPFEM was introduced as a generic and systematic approach for modeling flexible cable or tether systems [55]. In parallel, another finite element formulation, the Absolute Nodal Coordinate Formulation (ANCF) [56,57], was also applied to tether or cable systems. Unlike ANCF, which uses both nodal positions and slopes as state variables and is therefore not directly compatible with standard FEM implementations, NPFEM employs only nodal positions as state variables. This architectural simplicity makes NPFEM naturally compatible with the standard FEM, allowing for seamless incorporation into established finite element programs. Furthermore, the simplification also results in computational reduction [58], which has led to its widespread use for the dynamic analysis of TSS. In further NPFEM developments, Li et al. [59] proposed a variable-length element formulation with the Arbitrary Lagrangian–Eulerian (ALE) description (NPFEM-ALE) to model partial space elevators performing cross-orbital payload transport along the tether, revealing that elastic tether dynamics can induce significant high-frequency oscillations that must be accounted for safe operation.

Du and Zhu [60] employed a high-fidelity NPFEM-based elastic tether model to investigate stability and control of an axisymmetric electric solar wind sail considering spin-rate limits and configuration stability under solar-wind fluctuations. In addition, NPFEM has been extended to planar [61] and solid elements [62,63], further broadening its applicability to complex and large-scale flexible structures.

Although separate advances in finite element modeling of elastic tether and spacecraft structures, TSS dynamic analyses still heavily rely on rigid-flexible coupling formulations to capture the orbital-structural coupling between the tether and the connected spacecraft. In these approaches, the tether is modeled as one or a series of elastic elements, whereas the spacecraft are treated as rigid bodies. For example, Lu et al. [64] developed a rigid-flexible coupled model for a spinning electrodynamic tether system, in which the tether was represented using a bead-spring representation and the spacecraft was modeled as a rigid body with quaternions. Based on this framework, they designed a spin-up control strategy by an adaptive sliding-mode controller with a high-gain saturated attitude controller to suppress tether deformation and stabilize the spacecraft motion in orbit. Similarly, Du et al. [65] examined the attitude stability of an electric solar wind sail using a rigid-flexible coupling model. In their approach, elastic tether dynamics was captured by NPFEM, while the spacecraft attitude was described by a natural coordinate formulation that couples the elastic tether with rigid spacecraft. Their study revealed that the sail's stability is strongly influenced by orbital-structural coupling effects.

Despite their effectiveness, rigid-flexible coupling frameworks inherently rely on

artificial constraints, such as Lagrange multipliers or explicit constraint equations, to enforce compatibility between rigid spacecraft and flexible tethers. These constraints increase the complexity of the governing equations by destroying their symmetry and introducing numerical singularities, which can degrade numerical stability, particularly in long-duration simulations. Furthermore, as spacecraft become larger, lighter, and more flexible, neglecting spacecraft structural elasticity reduces physical fidelity and can lead to inaccurate predictions of dynamic tether-spacecraft load transfer via the constraints in the presence of orbital-structural coupling.

2.2. State Estimation of Flexible Space Tethers

Most current studies assume that space tethers are straight and inextensible, which is used as a basis for controller design [66]. Under this idealization, stability analysis is typically reduced to the librational motion of a straight tether with only two degrees of freedom, namely the in-plane and out-of-plane libration angles. In practice, however, a tether is flexible and may undergo lateral deflection, bending, and rotation about the axis connecting the end spacecraft when subjected to lateral loading or large libration motion. Under such conditions, the straight-tether assumption becomes invalid, and control strategies derived from it cannot in general guarantee system stability [67]. Alternatively, discrete tether models have been developed in the literature to better predict the dynamic behavior of the tether by discretizing it into a series of interconnected rigid rods [68], elastic links or elements [69]. While these models are more accurate, they make the existing

control methodologies based on a single straight tether no longer applicable, as the tether discretization results in a set of libration angles for each element. Controlling a bent tether to its desired shape requires feedback on the full state of all elements or on libration angles, which is practically infeasible due to the tether's extremely thin nature and the difficulty of placing sensors on individual elements along its length.

Some state estimation algorithms have been developed to control the lateral flexural motion of space tethers [49,66,70–73]. For instance, Netzer and Kane [66] modeled a flexible tether as multiple rigid rods to represent its in-plane libration. The lateral flexural motion of the tether was represented by a series of angles between the rods. Using the poses and rates of the two spacecraft at the tether’s two ends, a state estimator was proposed to estimate these angles and angular velocities based on the dynamic model of the discretized tether. The estimator was solved and propagated simultaneously with a model-based proportional feedback control applied at the main satellite. The observability of the estimator and the controllability with this feedback were proved. Williams [70] later extended the estimation problem to three-dimensional tether motion by modeling the tether as a series of point masses connected by rigid, massless links and using an unscented filter to recursively estimate the internal mass positions from end-position and tension measurements.

However, both approaches neglected the tether's elasticity, which may result in high-frequency longitudinal oscillations under external loads and control actions, leading to unstable tether motion. To overcome this limitation, Li and Zhu [49,72] developed a finite

element state estimator based on NPFEM and Kalman filter. In their approach, the tether was discretized into a series of massive elastic tensile-only elements in 3D space, and the positions and velocities of the internal element nodes along the tether were estimated by solving the nonlinear finite element model using known positions and velocities at two ends of the tether. To avoid singularity or ambiguity in the estimation that would occur if the number of internal nodes is greater than two, the tether's state (nodal position and velocity) was then propagated in the temporal domain by an extended Kalman filter. The measurement model was augmented by combining the estimated internal nodal positions and velocities with the measured positions and velocities at the two ends. The observability of the finite element state estimator was proven, and it was applied with model predictive control to effectively control a bent electrodynamic tether into a straight one [49]. Later, Fang et al. estimated the state of the mid spacecraft in an elastic double-pendulum tethered spacecraft system using an unscented Kalman filter [73], which can be seen as a special case of Li and Zhu's approach [49,72].

It is noteworthy that Refs. [49,72] present the only state estimation algorithm dedicated to space tethers based on FEM. Other state estimation schemes for tethers were not designed to estimate the deformed shape of tethers, but the attitude of TSS and the distance between spacecraft in spacecraft formation flying, where tethers were assumed straight. To address this challenge, Zhang and El Ghali, et al. [74] propose a novel robust FE-Kalman state estimator for full-state reconstruction of flexible tethers from partial measurements. They integrated distributed strain sensing, inverse NPFEM, and FEM

virtual sensing into a unified Kalman filtering framework. The resulting estimator not only enables complete tether-state estimation, but also provides theoretical guarantees of boundedness under measurement noise and observability.

2.3. Configuration Control of Flexible Space Tethers

As the most important component of TSS, the configuration control of space tethers faces significant challenges due to tether flexibility, geometrical nonlinearity, underactuation, and space environmental disturbances [75]. These factors make stable configuration control difficult, complicate accurate tether profile measurement, reduce control authority, and demand high computational efficiency. As a result, these issues significantly hinder the effective application of TSS in space missions.

Various control schemes have been developed for the effective control of space tethers, e.g., sliding mode control [76], optimal control [77], fractional-order control [78], and artificial intelligence-based methods [79]. Notably, Sun and Zhu [80] pioneered the fractional-order control framework for managing both in-plane and out-of-plane tether deployment and retrieval in TSS. Li et al. [81] extended the fractional-order control with a neural network-augmented adaptive super-twisting controller. Zhang et al. [82] demonstrated the superiority of a fractional-order robust fixed-time SMC strategy in controlling the in-plane libration of TSS, while Kang and Zhu [83] implemented a passivity-based model predictive control for de-spinning a rotating object in a central gravity field by a tethered micro-tug. Su et al. [84] further investigated the configuration

stability control of a triangular TSS by a radial basis function neural network controller to ensure robust tracking performance under system uncertainties. However, many of the aforementioned approaches rely on oversimplified dynamic models that overlook critical factors in space tethers: (i) tether elasticity-induced oscillations between slack/taut states, which violate the fundamental assumption of tether's incompressibility in the simplified model, and (ii) challenges related to underactuation and tension saturation, which remain inadequately addressed.

Recently, researchers have developed high-fidelity tether models by FEM to capture their flexural bending accurately. However, the discretization process transforms the space tethers into an underactuated dynamic system with high degrees of freedom (DOF), rendering conventional control strategies based on a simplified model ineffective.

While high-fidelity modeling for TSS via FEM is mature, controller synthesis for such large-scale discretized dynamics remains challenging. Furthermore, the full-state feedback control in FE models requires state information at every node, overlooking the practical challenges that sensors cannot be placed along the thin tether. Li and Zhu [72] proposed a model predictive control scheme for maintaining the geometric profile of an electrodynamic tether system by accurately tracking a straight-tether trajectory. Their method achieves full actuation by modulating the electric current along the tether, thereby generating distributed Lorentz forces. However, the space tethers are fully actuated by Lorentz forces acting along the tether length by controlling the electric current in the tether.

To address these challenges, Zhang and Zhu [77] propose a novel computational

optimal feedback control framework for flexible space tethers that replaces closed-form analytical control laws with numerically generated feedback control. By incorporating a robust Finite Element-Kalman (FE-Kalman) state estimator, the framework establishes the relationship between measurable states at the tether ends and the unmeasurable states of the tether profile, thereby enabling full-state feedback control from sparse boundary measurements. Unlike conventional optimal control approaches that require repeated nonlinear programming, the proposed method reformulates the problem into Hamilton's canonical equations via the variational principle, thereby enabling the dynamic generation of control inputs for online implementation.

To further overcome the limitations of continuous-system control formulations, we develop a co-located computational control framework that is fully compatible with high-fidelity finite element discretization. This framework lies in the direct formulation of control at the element level, the systematic assembly of local controllers into a global control law using the standard finite element procedure, and the incorporation of finite-element-based state estimation for closed-loop implementation under sparse sensing. The proposed framework adopts a dual-loop architecture: an outer loop generates robust element-wise reference trajectories via SMC, while an inner loop efficiently tracks these trajectories by a proportional-derivative controller with dynamic compensation. In this way, the method provides a practical control strategy for underactuated flexible space tethers, enabling boundary actuation at the tether ends to regulate distributed interior dynamics without the need for actuators or sensors along the tether length.

Chapter 3 MATHEMATICAL MODELING USING NODAL POSITION FINITE ELEMENT METHOD

Summary: This chapter develops a unified, full elastic dynamic model for tethered space systems. A nodal position-based two-node tether element is formulated for the elastodynamic analysis of the tether, while an eight-node isoparametric hexahedral element is developed for the elastodynamic analysis of the spacecraft. The eight-node isoparametric hexahedral element, based on the nodal position finite element method and detailed in Section 3.3, was first proposed by the author and is published in **Reference (2)** listed in Section 1.6. These two elements are then integrated to establish a full elastic representation of tethered space systems. This work is based on the manuscript listed as Reference (7) in Section 1.6.

3.1. Description of the Tethered Space System

A TSS operating in a circular Earth orbit is considered, as schematically illustrated in Figure 3-1. The system consists of a main spacecraft and a sub-spacecraft interconnected by a long, flexible tether. To accurately capture the structural deformation and dynamic interaction between the two bodies, a full elastic model is developed based on the following assumptions: (1) the large spacecraft is modeled as an elastic cubic body composed of an isotropic, homogeneous material, allowing for deformation under external and internal

loads; (2) the tether is assumed to be made of an isotropic elastic material that can sustain only tensile forces, neglecting compressive and bending stiffness due to its slender geometry; (3) In the high-fidelity representation, the spacecraft are discretized into m eight-node solid finite elements to capture their three-dimensional elastic behavior, while the tether is discretized into n nodes connected by $(n-1)$ tensile elements to represent its longitudinal deformation. To describe the overall motion of the TSS in orbit, an Earth-centered inertial (ECI) coordinate frame O-XYZ is established. The origin O of this frame is located at the center of the Earth, with the Z-axis aligned with the Earth's rotational axis, the X-axis pointing toward the vernal equinox, and the Y-axis completing a right-handed orthogonal coordinate system. Within this reference frame, the dynamic behavior of TSS is characterized by the positions and velocities of each discretized node, which collectively define both the translation motion of the system and the elastic deformation of its components.

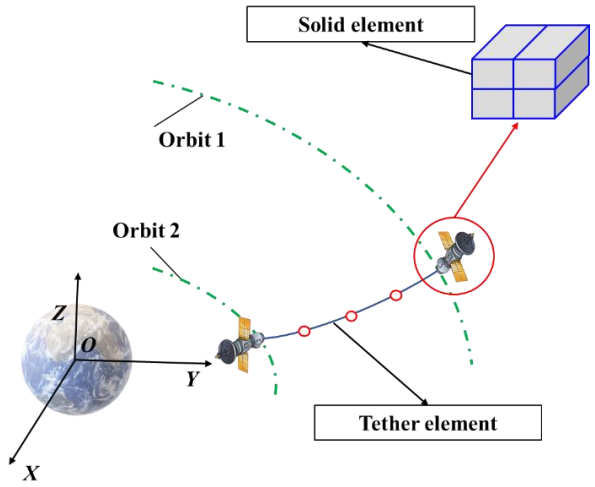

Figure 3-1 The finite element discretized model of TSS in orbit.

3.2. Tether Element Nodal Position Finite Element Method

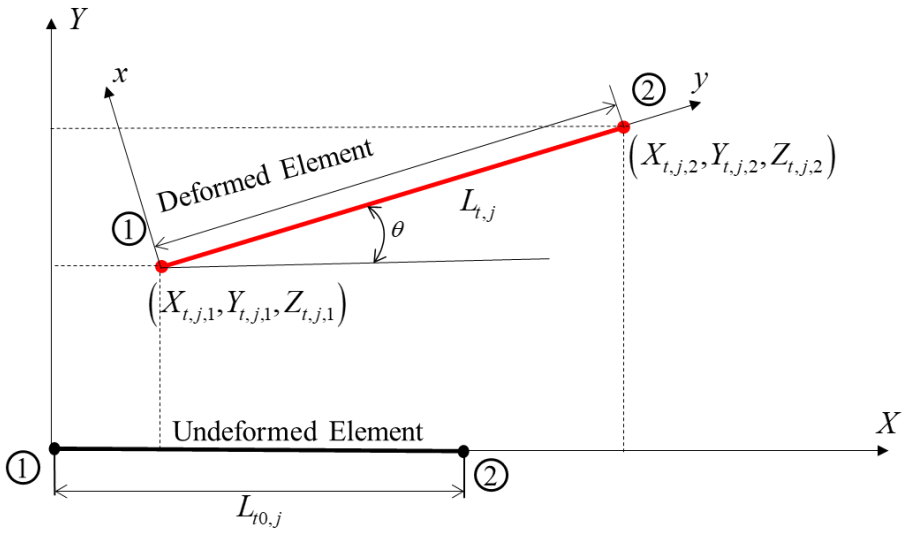

Figure 3-2 Deformation of the two-node tether element.

Consider a two-node straight tether element in the global frame, as illustrated in Figure 3-2. The local frame is defined as follows. The x-axis is aligned with the jth element and points from the $(j+1)^{th}$ node to the jth node, the z-axis is perpendicular to the x-axis, and the mean velocity vector of the element, and the y-axis completes a right-hand coordinate system. Here, the mean velocity vector of the element is defined as the mean velocity of two nodal velocities. Thus, the geometry and motion of the element can be described by nodal positions $\boldsymbol{X}_t$, velocities $\dot{\boldsymbol{X}}_t$, and accelerations $\ddot{\boldsymbol{X}}_t$ in the global frame, such that,

$$\boldsymbol{X}_t = \boldsymbol{N}_{t,j}\boldsymbol{X}_{t,j}, \dot{\boldsymbol{X}}_t = \boldsymbol{N}_{t,j}\dot{\boldsymbol{X}}_{t,j}, \ddot{\boldsymbol{X}}_t = \boldsymbol{N}_{t,j}\ddot{\boldsymbol{X}}_{t,j} \tag{3.1}$$

where the subscript j denotes the jth tether element in this chapter,

$\boldsymbol{X}_{t,j} = \left(X_{t,j,1}^{\mathrm{T}}, Y_{t,j,1}^{\mathrm{T}}, Z_{t,j,1}^{\mathrm{T}}, X_{t,j,2}^{\mathrm{T}}, Y_{t,j,2}^{\mathrm{T}}, Z_{t,j,2}^{\mathrm{T}} \right)^{\mathrm{T}}$ is the nodal coordinate vector, and the symbol of overhead dot denotes the derivatives with respect to time. The shape function matrix $\boldsymbol{N}_{t,j}$ is defined as

$$\boldsymbol{N}_{t,j} = \begin{bmatrix} 1-\xi_{t,j} & 0 & 0 & \xi_{t,j} & 0 & 0 \\ 0 & 1-\xi_{t,j} & 0 & 0 & \xi_{t,j} & 0 \\ 0 & 0 & 1-\xi_{t,j} & 0 & 0 & \xi_{t,j} \end{bmatrix} \tag{3.2}$$

where $\xi_{t,j} = L_{X,j} / L_{t,j}$, $L_{t,j} = \sqrt{\left(X_{t,j,2} - X_{s,j,1} \right)^2 + \left(Y_{t,j,2} - Y_{t,j,1} \right)^2 + \left(Z_{t,j,2} - Z_{t,j,1} \right)^2}$ is the instantaneous length of the jth element and $L_{X,j}$ is the distance between an arbitrary point along the element and the jth node.

The Green-Lagrangian strain of the jth element can be written as

$$\varepsilon_{t,j} = \frac{L_{t,j} - L_{t0,j}}{L_{t0,j}} = \boldsymbol{B}_{t,j} \boldsymbol{X}_{t,j} - 1 \tag{3.3}$$

where $L_{t0,j}$ are the original length of the jth element and $\boldsymbol{B}_{t,j}$ is the strain matrix. The strain matrix can be expressed as the product of the strain matrix $\boldsymbol{B}_{t,j}^{0}$ in the local frame and the coordinate transformation matrix $\boldsymbol{Q}_{t,j}$, such that,

$$\boldsymbol{B}_{t,j} = \boldsymbol{B}_{t,j}^{0} \boldsymbol{Q}_{t,j} \tag{3.4}$$

where

$$\boldsymbol{B}_{t,j}^{0} = \begin{bmatrix} -\dfrac{1}{L_{t0,j}} & 0 & 0 & \dfrac{1}{L_{t0,j}} & 0 & 0 \end{bmatrix}$$

$$\boldsymbol{Q}_{t,j}=\begin{bmatrix}\cos\theta_{x,j} & \cos\theta_{y,j} & \cos\theta_{z,j} & 0 & 0 & 0\\ 0 & 0 & 0 & 0 & 0 & 0\\ 0 & 0 & 0 & 0 & 0 & 0\\ 0 & 0 & 0 & \cos\theta_{x,j} & \cos\theta_{y,j} & \cos\theta_{z,j}\\ 0 & 0 & 0 & 0 & 0 & 0\\ 0 & 0 & 0 & 0 & 0 & 0\end{bmatrix}$$

$$\cos\theta_{x,j}=\frac{X_{t,j,2}-X_{t,j,1}}{L_{t,j}},\ \cos\theta_{y,j}=\frac{Y_{t,j,2}-Y_{t,j,1}}{L_{t,j}},\ \cos\theta_{z,j}=\frac{Z_{t,j,2}-Z_{t,j,1}}{L_{t,j}}$$

The strain energy can be derived as

$$\begin{aligned}U_{t,j}&=\frac{1}{2}\int_0^{L_{t,j}}E_{t,j}A_{t,j}\varepsilon_{t,j}^2ds\\&=\frac{1}{2}\boldsymbol{X}_{t,j}^{\mathrm{T}}\boldsymbol{K}_{t,j}\boldsymbol{X}_{t,j}-\boldsymbol{X}_{t,j}^{\mathrm{T}}\boldsymbol{F}_{t,j}^{0}+\frac{1}{2}E_tA_tL_{t0,j}\end{aligned}\tag{3.5}$$

where $E_{t,j}$ is the Young's modulus and $A_{t,j}$ represents the cross-sectional area. The stiffness matrix of the element $\boldsymbol{K}_{t,j}$, and the generalized nodal force vector $\boldsymbol{F}_{t,j}^{0}$ arising from the element's elasticity in the global frame, can be formulated as follows:

$$\boldsymbol{K}_{t,j}=E_{t,j}A_{t,j}\boldsymbol{Q}_{t,j}^{\mathrm{T}}\left(\boldsymbol{B}_{t,j}^{0}\right)^{\mathrm{T}}\boldsymbol{B}_{t,j}^{0}\boldsymbol{Q}_{t,j}\ \text{and}\ \boldsymbol{F}_{t,j}^{0}=E_{t,j}A_{t,j}L_{t0,j}\boldsymbol{Q}_{t}^{\mathrm{T}}\left(\boldsymbol{B}_{t,j}^{0}\right)^{\mathrm{T}}\tag{3.6}$$

The kinetic energy $T_{t,j}$ of the element is calculated as

$$T_{t,j}=\int_0^{L_{t,j}}\frac{1}{2}\left(\frac{d\boldsymbol{X}_t}{dt}\right)^{\mathrm{T}}\frac{d\boldsymbol{X}_t}{dt}\rho A_tds=\frac{1}{2}\left(\frac{d\boldsymbol{X}_{t,j}}{dt}\right)^{\mathrm{T}}\boldsymbol{M}_{t,j}\frac{d\boldsymbol{X}_{t,j}}{dt}\tag{3.7}$$

where $\rho_{t,j}$ is the material density and the element mass matrix $\boldsymbol{M}_{t,k}$ is expressed as

$$\boldsymbol{M}_{t,j}=\int_0^{L_{t,j}}\frac{1}{2}\rho_{t,j}A_{t,j}\boldsymbol{N}_{t,j}^{\mathrm{T}}\boldsymbol{N}_{t,j}ds\tag{3.8}$$

The mass matrices $\boldsymbol{M}_{t,j}$ can be expressed as

$$\boldsymbol{M}_{t,j} = \frac{\rho_{t,j} A_{t,j} L_{t,j}}{6} \begin{bmatrix} 2 & 0 & 0 & 1 & 0 & 0 \\ 0 & 2 & 0 & 0 & 1 & 0 \\ 0 & 0 & 2 & 0 & 0 & 1 \\ 1 & 0 & 0 & 2 & 0 & 0 \\ 0 & 1 & 0 & 0 & 2 & 0 \\ 0 & 0 & 1 & 0 & 0 & 2 \end{bmatrix}$$

Based on the principle of virtual work, one has

$$\delta U_{t,j} - \delta T_{t,j} - \delta \boldsymbol{X}_{t,j}^{\mathrm{T}} (\boldsymbol{f}_{t,j}^{e} + \boldsymbol{F}_{t,j}^{0}) = 0 \tag{3.9}$$

where $\boldsymbol{f}_{t,j}^{e}$ refers to the external force.

Substituting Eqs. (3.5)-(3.7) into Eq.(3.9) yields

$$\boldsymbol{M}_{t,j} \ddot{\boldsymbol{X}}_{t,j} + \boldsymbol{K}_{t,j} \boldsymbol{X}_{t,j} - \boldsymbol{f}_{t,j}^{e} - \boldsymbol{F}_{t,j}^{0} = \boldsymbol{0} \tag{3.10}$$

Considering the damping effect, Eq.(3.10) can be reformulated as

$$\boldsymbol{M}_{t,j} \ddot{\boldsymbol{X}}_{t,j} + \boldsymbol{K}_{t,j} \boldsymbol{X}_{t,j} + \boldsymbol{C}_{t,j} \dot{\boldsymbol{X}}_{t,j} - \boldsymbol{f}_{t,j}^{e} - \boldsymbol{F}_{t,j}^{0} = \boldsymbol{0} \tag{3.11}$$

where $\boldsymbol{C}_{t,j} = \alpha_t \boldsymbol{M}_{t,j} + \beta_t \boldsymbol{K}_{t,j}$ is the Rayleigh damping with damping coefficients (α_t , β_t).

The global finite element equation can be assembled by the standard assembly procedure in the traditional FEM, such that

$$\boldsymbol{M}_t \ddot{\boldsymbol{X}}_t + \boldsymbol{K}_t \boldsymbol{X}_t + \boldsymbol{C}_t \dot{\boldsymbol{X}}_t - \boldsymbol{F}_t^{0} - \boldsymbol{F}_t^{e} = \boldsymbol{0} \tag{3.12}$$

3.3. Solid Element Nodal Position Finite Element Method

3.3.1 Nodal Position Finite Element Method Formulation with Incompatible Mode

Consider an isoparametric 8-node hexahedral element in the global coordinate frame $OXYZ$ as shown in Figure 3-3. The nodal positions of the undeformed element are defined by their coordinates in $OXYZ$ as $\bar{\boldsymbol{X}}_{s,k,i} = \left(\bar{X}_{s,k,i}, \bar{Y}_{s,k,i}, \bar{Z}_{s,k,i}\right)^{\mathrm{T}} \in \mathbb{R}^{3\times 1}$ (i = 1, 2, …, 8), where the subscript k denotes the kth solid element in this chapter. Accordingly, the position vector $\bar{\boldsymbol{r}}_{s,k}$ of an arbitrary point P inside the element is assumed to be defined through interpolation of the nodal positions as

$$\bar{\boldsymbol{r}}_{s,k} = \bar{\boldsymbol{X}}_{s,k} = \boldsymbol{N}_{s,k}\bar{\boldsymbol{X}}_{s,k} \tag{3.13}$$

$$\boldsymbol{N}_{s,k} = \begin{bmatrix} N_{s,k,1}\mathbf{I}_3 & N_{s,k,2}\mathbf{I}_3 & N_{s,k,3}\mathbf{I}_{3\times 3} & N_{s,k,4}\mathbf{I}_{3\times 3} & N_{s,k,5}\mathbf{I}_{3\times 3} & N_{s,k,6}\mathbf{I}_{3\times 3} & N_{s,k,7}\mathbf{I}_{3\times 3} & N_{s,k,8}\mathbf{I}_{3\times 3} \end{bmatrix} \tag{3.14}$$

$$N_{s,k,i} = \left(1+\xi_{s,k,i}\xi_{s,k}\right)\left(1+\eta_{s,k,i}\eta_{s,k}\right)\left(1+\zeta_{s,k,i}\zeta_{s,k}\right)/8 \quad (i = 1,\ 2,\ \ldots,\ 8) \tag{3.15}$$

where $\boldsymbol{N}_{s,k} \in \mathbb{R}^{3\times 24}$ is the shape function matrix for the element, $\mathbf{I}_{3\times 3} \in \mathbb{R}^{3\times 3}$ is an identity matrix, $N_{s,k,i}$ is the trilinear shape function in terms of natural coordinates $\left(\xi_{s,k}, \eta_{s,k}, \zeta_{s,k}\right) \in [-1,\ 1]$, $\bar{\boldsymbol{X}}_{s,k} = \left(\bar{\boldsymbol{X}}_{s,k,1}^{\mathrm{T}}, \bar{\boldsymbol{X}}_{s,k,2}^{\mathrm{T}}, \cdots, \bar{\boldsymbol{X}}_{s,k,8}^{\mathrm{T}}\right)^{\mathrm{T}} \in \mathbb{R}^{24\times 1}$ is the nodal position vector,

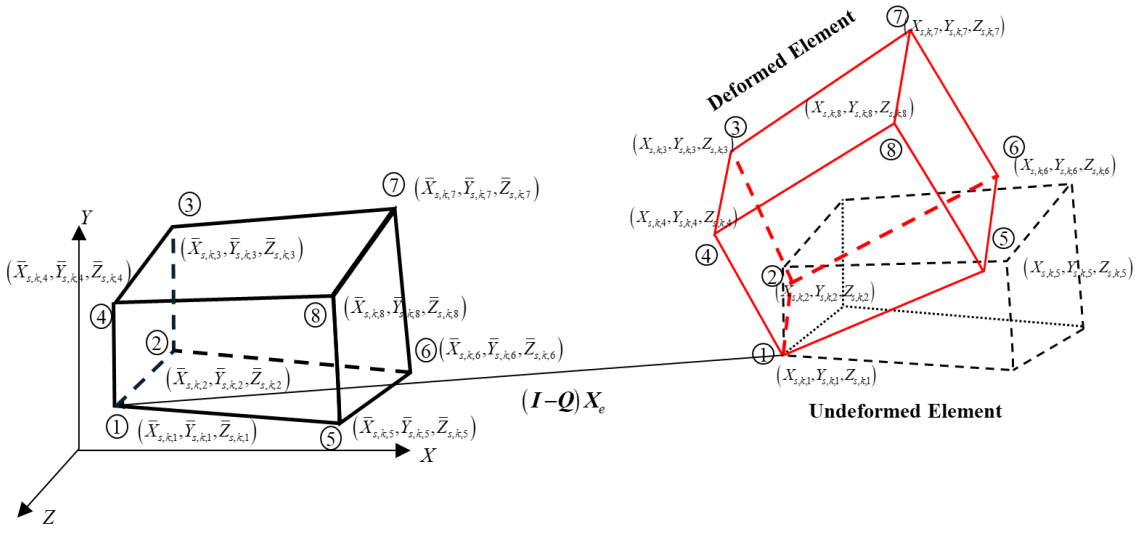

Figure 3-3 Deformation of the eight-node solid element.

Assume the element experienced a translational and rotational deformation into a new position, denoted by a new nodal position vector $\boldsymbol{X}_{s,k}=\left(X_{s,k,1},Y_{s,k,1},Z_{s,k,1},X_{s,k,2},Y_{s,k,2},Z_{s,k,2},\cdots,X_{s,k,8},Y_{s,k,8},Z_{s,k,8}\right)^{\mathrm{T}}$. Accordingly, the arbitrary point P is moved to a new position P' in the global frame $OXYZ$,

$$\boldsymbol{r}_s=\boldsymbol{X}_s=\boldsymbol{N}_{s,k}\boldsymbol{X}_{s,k} \tag{3.16}$$

Since the rigid-body translation does not induce any strain in the deformed element, such rigid-body motion can be easily removed from the elastic deformation calculation by moving the undeformed element from its node 1 translationally to node 1 of the deformed element, as shown in Figure 3-3. Accordingly, the nodal position vector of the undeformed element relative to the nodal position vector of the deformed element can be expressed as

$$\bar{\boldsymbol{X}}_{s,k}=\boldsymbol{Q}_{s,k}\boldsymbol{X}_{s,k}+\boldsymbol{X}_{s,k,0}\quad\text{and}\quad\boldsymbol{X}_{s,k,0}=\left(\mathbf{I}_{24\times24}-\boldsymbol{Q}_{s,k}\right)\bar{\boldsymbol{X}}_{s,k} \tag{3.17}$$

where $\boldsymbol{X}_{s,k,0}$ is the nodal position vector of the undeformed element relative to node 1, and the matrix $\boldsymbol{Q}_{s,k}$ reflects the rigid-body translation

$$\boldsymbol{Q}_{s,k}=\begin{bmatrix}\mathbf{I}_{3\times3} & \mathbf{0} & \mathbf{0} & \mathbf{0} & \mathbf{0} & \mathbf{0} & \mathbf{0} & \mathbf{0}\\ \mathbf{I}_{3\times3} & \mathbf{0} & \mathbf{0} & \mathbf{0} & \mathbf{0} & \mathbf{0} & \mathbf{0} & \mathbf{0}\\ \mathbf{I}_{3\times3} & \mathbf{0} & \mathbf{0} & \mathbf{0} & \mathbf{0} & \mathbf{0} & \mathbf{0} & \mathbf{0}\\ \mathbf{I}_{3\times3} & \mathbf{0} & \mathbf{0} & \mathbf{0} & \mathbf{0} & \mathbf{0} & \mathbf{0} & \mathbf{0}\\ \mathbf{I}_{3\times3} & \mathbf{0} & \mathbf{0} & \mathbf{0} & \mathbf{0} & \mathbf{0} & \mathbf{0} & \mathbf{0}\\ \mathbf{I}_{3\times3} & \mathbf{0} & \mathbf{0} & \mathbf{0} & \mathbf{0} & \mathbf{0} & \mathbf{0} & \mathbf{0}\\ \mathbf{I}_{3\times3} & \mathbf{0} & \mathbf{0} & \mathbf{0} & \mathbf{0} & \mathbf{0} & \mathbf{0} & \mathbf{0}\\ \mathbf{I}_{3\times3} & \mathbf{0} & \mathbf{0} & \mathbf{0} & \mathbf{0} & \mathbf{0} & \mathbf{0} & \mathbf{0}\end{bmatrix}\in\mathbb{R}^{24\times24} \tag{3.18}$$

Based on Eq. (3.17), the displacement vector $\boldsymbol{U}_{s,k}$ of point *P* can be written as

$$\boldsymbol{U}_{s,k}=\boldsymbol{N}_{s,k}\left(\boldsymbol{X}_{s,k}-\bar{\boldsymbol{X}}_{s,k}\right)=\boldsymbol{N}_{s,k}\left[\left(\mathbf{I}_{24\times24}-\boldsymbol{Q}_{s,k}\right)\boldsymbol{X}_{s,k}-\boldsymbol{X}_{s,k,0}\right] \tag{3.19}$$

Subsequently, the Green-Lagrangian strain $\boldsymbol{\varepsilon}_{s,k}\in\mathbb{R}^{6}$ can be derived as [85]

$$\boldsymbol{\varepsilon}_{s,k}=\left[\frac{\boldsymbol{r}_x'^{\mathrm{T}}\boldsymbol{r}_x'-1}{2}\quad\frac{\boldsymbol{r}_y'^{\mathrm{T}}\boldsymbol{r}_y'-1}{2}\quad\frac{\boldsymbol{r}_z'^{\mathrm{T}}\boldsymbol{r}_z'-1}{2}\quad\boldsymbol{r}_x'^{\mathrm{T}}\boldsymbol{r}_y'\quad\boldsymbol{r}_y'^{\mathrm{T}}\boldsymbol{r}_z'\quad\boldsymbol{r}_z'^{\mathrm{T}}\boldsymbol{r}_x'\right]^{\mathrm{T}} \tag{3.20}$$

where

$$\frac{\partial\bar{\boldsymbol{r}}}{\partial\boldsymbol{X}}=\left[\boldsymbol{r}_x'\quad\boldsymbol{r}_y'\quad\boldsymbol{r}_z'\right]=\mathbf{I}_{3\times3}+\frac{\partial\boldsymbol{U}_{s,k}}{\partial\boldsymbol{X}}=\mathbf{I}_{3\times3}+\frac{\partial\boldsymbol{N}_{s,k}}{\partial\boldsymbol{X}}\left[\left(\mathbf{I}_{24\times24}-\boldsymbol{Q}_{s,k}\right)\boldsymbol{X}_{s,k}-\boldsymbol{X}_{s,k,0}\right] \tag{3.21}$$

Substituting Eq. (3.21) into Eq. (3.20) yields the strain expressed in terms of nodal positions,

$$\boldsymbol{\varepsilon}_{s,k} = \boldsymbol{B}_{s,k}\left[\left(\mathbf{I}_{24\times 24} - \boldsymbol{Q}_{s,k}\right)\boldsymbol{X}_{s,k} - \boldsymbol{X}_{s,k,0}\right], \quad \boldsymbol{B}_{s,k} = \boldsymbol{B}_{s,k,L} + \boldsymbol{B}_{s,k,N} \tag{3.22}$$

where $\boldsymbol{B}_{s,k} \in \mathbb{R}^{6\times 24}$ is the total strain matrix, and ($\boldsymbol{B}_{s,k,L} \in \mathbb{R}^{6\times 24}, \boldsymbol{B}_{s,k,N} \in \mathbb{R}^{6\times 24}$) are the linear and nonlinear strain matrices, respectively,

$$\boldsymbol{B}_{s,k,L} = \left[\boldsymbol{B}^{1}_{s,k,L}, \cdots, \boldsymbol{B}^{8}_{s,k,L}\right], \boldsymbol{B}^{i}_{s,k,L} = \begin{bmatrix} \dfrac{\partial N_{s,k,i}}{\partial X_{s,k}} & 0 & 0 \\ 0 & \dfrac{\partial N_{s,k,i}}{\partial Y_{s,k}} & 0 \\ 0 & 0 & \dfrac{\partial N_{s,k,i}}{\partial Z_{s,k}} \\ \dfrac{\partial N_{s,k,i}}{\partial Y_{s,k}} & \dfrac{\partial N_{s,k,i}}{\partial X_{s,k}} & 0 \\ \dfrac{\partial N_{s,k,i}}{\partial Z_{s,k}} & 0 & \dfrac{\partial N_{s,k,i}}{\partial X_{s,k}} \\ 0 & \dfrac{\partial N_{s,k,i}}{\partial Z_{s,k}} & \dfrac{\partial N_{s,k,i}}{\partial Y_{s,k}} \end{bmatrix} \tag{3.23}$$

$$\boldsymbol{B}_{s,k,N}=\begin{bmatrix}\frac{1}{2}\left[\boldsymbol{X}_{s,k}^{\mathrm{T}}\left(\mathbf{I}_{24\times24}-\boldsymbol{Q}^{\mathrm{T}}\right)-\boldsymbol{X}_{s,k,0}^{\mathrm{T}}\right]\left(\frac{\partial \boldsymbol{N}_{s,k}}{\partial \boldsymbol{X}}\right)^{\mathrm{T}}\frac{\partial \boldsymbol{N}_{s,k}}{\partial \boldsymbol{X}}\\ \frac{1}{2}\left[\boldsymbol{X}_{s,k}^{\mathrm{T}}\left(\mathbf{I}_{24\times24}-\boldsymbol{Q}^{\mathrm{T}}\right)-\boldsymbol{X}_{s,k,0}^{\mathrm{T}}\right]\left(\frac{\partial \boldsymbol{N}_{s,k}}{\partial \boldsymbol{Y}}\right)^{\mathrm{T}}\frac{\partial \boldsymbol{N}_{s,k}}{\partial \boldsymbol{Y}}\\ \frac{1}{2}\left[\boldsymbol{X}_{s,k}^{\mathrm{T}}\left(\mathbf{I}_{24\times24}-\boldsymbol{Q}^{\mathrm{T}}\right)-\boldsymbol{X}_{s,k,0}^{\mathrm{T}}\right]\left(\frac{\partial \boldsymbol{N}_{s,k}}{\partial \boldsymbol{Z}}\right)^{\mathrm{T}}\frac{\partial \boldsymbol{N}_{s,k}}{\partial \boldsymbol{Z}}\\ \left[\boldsymbol{X}_{s,k}^{\mathrm{T}}\left(\mathbf{I}_{24\times24}-\boldsymbol{Q}^{\mathrm{T}}\right)-\boldsymbol{X}_{s,k,0}^{\mathrm{T}}\right]\left(\frac{\partial \boldsymbol{N}_{s,k}}{\partial \boldsymbol{X}}\right)^{\mathrm{T}}\frac{\partial \boldsymbol{N}_{s,k}}{\partial \boldsymbol{Y}}\\ \left[\boldsymbol{X}_{s,k}^{\mathrm{T}}\left(\mathbf{I}_{24\times24}-\boldsymbol{Q}^{\mathrm{T}}\right)-\boldsymbol{X}_{s,k,0}^{\mathrm{T}}\right]\left(\frac{\partial \boldsymbol{N}_{s,k}}{\partial \boldsymbol{Y}}\right)^{\mathrm{T}}\frac{\partial \boldsymbol{N}_{s,k}}{\partial \boldsymbol{Z}}\\ \left[\boldsymbol{X}_{s,k}^{\mathrm{T}}\left(\mathbf{I}_{24\times24}-\boldsymbol{Q}^{\mathrm{T}}\right)-\boldsymbol{X}_{s,k,0}^{\mathrm{T}}\right]\left(\frac{\partial \boldsymbol{N}_{s,k}}{\partial \boldsymbol{Z}}\right)^{\mathrm{T}}\frac{\partial \boldsymbol{N}_{s,k}}{\partial \boldsymbol{X}}\end{bmatrix} \tag{3.24}$$

Assuming the element obeys Hooke's law, the strain energy of the element is defined as

$$U_{s,k}=\frac{1}{2}\int_{V_{0,k}}\boldsymbol{\varepsilon}_{s,k}^{\mathrm{T}}\boldsymbol{D}_{s,k}\boldsymbol{\varepsilon}_{s,k}dV=\frac{1}{2}\left[\boldsymbol{X}_{s,k}^{\mathrm{T}}\left(\mathbf{I}_{24\times24}-\boldsymbol{Q}_{s,k}^{\mathrm{T}}\right)-\boldsymbol{X}_{s,k,0}^{\mathrm{T}}\right]\boldsymbol{K}_{s,k,0}\left[\left(\mathbf{I}_{24\times24}-\boldsymbol{Q}_{s,k}\right)\boldsymbol{X}_{s,k}-\boldsymbol{X}_{s,k,0}\right] \tag{3.25}$$

$$\boldsymbol{K}_{s,0,k}=\int_{V_{0,k}}\boldsymbol{B}_{s,k}^{\mathrm{T}}\boldsymbol{D}_{s,k}\boldsymbol{B}_{s,k}dV \tag{3.26}$$

$$\boldsymbol{D}_{s,k}=\frac{E_{s,k}}{\left(1+\nu_{s,k}\right)\left(1-2\nu_{s,k}\right)}\begin{bmatrix}1-\nu_{s,k} & \nu_{s,k} & \nu_{s,k} & 0 & 0 & 0\\ \nu_{s,k} & 1-\nu_{s,k} & \nu_{s,k} & 0 & 0 & 0\\ \nu_{s,k} & \nu_{s,k} & 1-\nu_{s,k} & 0 & 0 & 0\\ 0 & 0 & 0 & \frac{1-2\nu_{s,k}}{2} & 0 & 0\\ 0 & 0 & 0 & 0 & \frac{1-2\nu_{s,k}}{2} & 0\\ 0 & 0 & 0 & 0 & 0 & \frac{1-2\nu_{s,k}}{2}\end{bmatrix} \tag{3.27}$$

where $\boldsymbol{D}_{s,k}\in\mathbb{R}^{6\times 6}$ is the elastic coefficient matrix, $E_{s,k}$ is the Young's Modulus, $\nu_{s,k}$ is the Poisson's ratio, $V_{0,k}$ is the volume of the undeformed element, and $\boldsymbol{K}_{s,k,0}$ is the element stiffness matrix.

It is worth noting here that the expression of $\boldsymbol{K}_{s,0,k}$ is the same as that in conventional FEM. Since the shape function $\boldsymbol{N}_{s,k}$ is defined in the natural coordinates $\left(\xi_{s,k},\eta_{s,k},\zeta_{s,k}\right)$, its derivative with respect to $\boldsymbol{X}_{s,k}$ must be calculated through the isoparametric transformation [86], such that

$$\begin{bmatrix}\frac{\partial N_{s,k,i}}{\partial X}\\ \frac{\partial N_{s,k,i}}{\partial Y}\\ \frac{\partial N_{s,k,i}}{\partial Z}\end{bmatrix}=\boldsymbol{J}_{s,k}\left(\frac{X_{s,k},Y_{s,k},Z_{s,k}}{\xi_{s,k},\eta_{s,k},\zeta_{s,k}}\right)^{-1}\begin{bmatrix}\frac{\partial N_{s,k,i}}{\partial \xi_{s,k}}\\ \frac{\partial N_{s,k,i}}{\partial \eta_{s,k}}\\ \frac{\partial N_{s,k,i}}{\partial \zeta_{s,k}}\end{bmatrix} \tag{3.28}$$

where $\boldsymbol{J}_{s}$ is the transformation Jacobian matrix can be evaluated by

$$\boldsymbol{J}_{s,k}\left(\frac{X_{s,k},Y_{s,k},Z_{s,k}}{\xi_{s,k},\eta_{s,k},\zeta_{s,k}}\right)=\left[\frac{\partial \boldsymbol{N}_{s,k}}{\partial \xi_{s,k}}\boldsymbol{X}_{s,k}\quad \frac{\partial \boldsymbol{N}_{s,k}}{\partial \eta_{s,k}}\boldsymbol{X}_{s,k}\quad \frac{\partial \boldsymbol{N}_{s,k}}{\partial \zeta_{s,k}}\boldsymbol{X}_{s,k}\right]^{\mathrm{T}} \tag{3.29}$$

Accordingly, the integration of the stiffness matrix $\boldsymbol{K}_{s,0,k}$ is transformed from the physical space *OXYZ* into the natural coordinate space $o\xi_s\eta_s\zeta_s$, such that,

$$\boldsymbol{K}_{s,k,0}=\int_{V_0}\boldsymbol{B}_{s,k}^{\mathrm{T}}\boldsymbol{D}_{s,k}\boldsymbol{B}_{s,k}dV=\int_{-1}^{1}\int_{-1}^{1}\int_{-1}^{1}\boldsymbol{B}_{s,k}^{\mathrm{T}}\boldsymbol{D}_{s,k}\boldsymbol{B}_{s,k}\left|\boldsymbol{J}\right|d\xi_{s,k}d\eta_{s,k}d\zeta_{s,k}=\boldsymbol{K}_{s,k,0L}+\boldsymbol{K}_{s,k,0LN}+\boldsymbol{K}_{s,k,0N} \tag{3.30}$$

$$\begin{aligned}
\boldsymbol{K}_{s,k,0L}&=\int_{-1}^{1}\int_{-1}^{1}\int_{-1}^{1}\boldsymbol{B}_{s,L,k}^{\mathrm{T}}\boldsymbol{D}_{s,k}\boldsymbol{B}_{s,L,k}\left|\boldsymbol{J}\right|d\xi_{s,k}d\eta_{s,k}d\zeta_{s,k}\\
\boldsymbol{K}_{s,k,0LN}&=\int_{-1}^{1}\int_{-1}^{1}\int_{-1}^{1}\left(\boldsymbol{B}_{s,L,k}^{\mathrm{T}}\boldsymbol{D}_{s,k}\boldsymbol{B}_{s,N,k}+\boldsymbol{B}_{s,N,k}^{\mathrm{T}}\boldsymbol{D}_{s,k}\boldsymbol{B}_{s,L,k}\right)\left|\boldsymbol{J}_{s,k}\right|d\xi_{s,k}d\eta_{s,k}d\zeta_{s,k}\\
\boldsymbol{K}_{s,k,0N}&=\int_{-1}^{1}\int_{-1}^{1}\int_{-1}^{1}\boldsymbol{B}_{s,N,k}^{\mathrm{T}}\boldsymbol{D}_{s,k}\boldsymbol{B}_{s,N,k}\left|\boldsymbol{J}\right|d\xi_{s,k}d\eta_{s,k}d\zeta_{s,k}
\end{aligned} \tag{3.31}$$

where $\boldsymbol{K}_{s,k,0L}$ is the linear stiffness matrix and $\boldsymbol{K}_{s,k,0N}$ and $\boldsymbol{K}_{s,k,0LN}$ are the nonlinear and linear-nonlinear coupling stiffness matrices, respectively. If the geometric nonlinearity is not considered, the stiffness matrices $\boldsymbol{K}_{s,k,0N}$ and $\boldsymbol{K}_{s,k,0LN}$ can be removed from Eq. (3.30).

Substituting Eq. (3.30) into Eq. (3.25) leads to the strain energy in terms of nodal positions

$$\begin{aligned}
U_{s,k}&=\frac{1}{2}\boldsymbol{X}_{s,k}^{\mathrm{T}}\left(\mathbf{I}_{24\times24}-\boldsymbol{Q}_{s,k}^{\mathrm{T}}\right)\boldsymbol{K}_{s,k,0}\left(\mathbf{I}_{24\times24}-\boldsymbol{Q}_{s,k}^{\mathrm{T}}\right)\boldsymbol{X}_{s,k,0}\\
&\quad-\boldsymbol{X}_{s,k}^{\mathrm{T}}\left(\mathbf{I}_{24\times24}-\boldsymbol{Q}_{s,k}^{\mathrm{T}}\right)\boldsymbol{K}_{s,k,0}\boldsymbol{X}_{s,0,k}+\frac{1}{2}\boldsymbol{X}_{s,k,0}^{\mathrm{T}}\boldsymbol{K}_{s,k,0}\boldsymbol{X}_{s,k,0}\\
&=\frac{1}{2}\boldsymbol{X}_{s,k}^{\mathrm{T}}\left(\mathbf{I}_{24\times24}-\boldsymbol{Q}_{s,k}^{\mathrm{T}}\right)\boldsymbol{K}_{s,k,0}\left(\mathbf{I}_{24\times24}-\boldsymbol{Q}_{s,k}^{\mathrm{T}}\right)\boldsymbol{X}_{s,k}-\boldsymbol{X}_{s,k}^{\mathrm{T}}\boldsymbol{F}_{s,k}^{0}+\frac{1}{2}\boldsymbol{X}_{s,k,0}^{\mathrm{T}}\boldsymbol{K}_{s,k,0}\boldsymbol{X}_{s,k,0}
\end{aligned}$$

(3.32)

where $\boldsymbol{F}_{s,k}^{0}=\left(\mathbf{I}_{24\times 24}-\boldsymbol{Q}_{s,k}^{\mathrm{T}}\right)\boldsymbol{K}_{s,k,0}\boldsymbol{X}_{s,k,0}$ is the unique equivalent elastic force term in the NPFEM approach.

The above stiffness matrix $\boldsymbol{K}_{s,k,0}$ does not include the flexural bending mode and will lead to shear locking due to the trilinear shape function in Eq. (3.15). To mitigate the limitation, introduce incompatible modes that represent the flexural bending modes into the displacement field in the element as per [87], such that,

$$\boldsymbol{U}_{s,k}=\boldsymbol{N}_{s,k}\left[\left(\mathbf{I}_{24\times 24}-\boldsymbol{Q}_{s,k}\right)\boldsymbol{X}_{s,k}-\boldsymbol{X}_{s,k,0}\right]+\left[P_{s,k,1}\mathbf{I}_{3\times 3}\quad P_{s,k,2}\mathbf{I}_{3\times 3}\quad P_{s,k,3}\mathbf{I}_{3\times 3}\right]\boldsymbol{\alpha}_{s,k} \tag{3.33}$$

where $P_{s,k,1}=1-\xi_s^2$, $P_{s,k,2}=1-\eta_s^2$, $P_{s,k,3}=1-\zeta_s^2$, and $\boldsymbol{\alpha}_{s,k}=\left(\alpha_{s,k}^{11},\alpha_{s,k}^{21},\alpha_{s,k}^{31},\alpha_{s,k}^{12},\alpha_{s,k}^{22},\alpha_{s,k}^{32},\alpha_{s,k}^{13},\alpha_{s,k}^{23},\alpha_{s,k}^{33}\right)^{\mathrm{T}}$ is the parameter vector of the incompatible displacement modes that will be determined by the static condensation method as follows

Then, the corresponding strain field with the flexural bending modes is derived as

$$\boldsymbol{\varepsilon}_{s,k}=\boldsymbol{B}_{s,k}\left[\left(\mathbf{I}_{24\times 24}-\boldsymbol{Q}_{s,k}\right)\boldsymbol{X}_{s,k}-\boldsymbol{X}_{s,k,0}\right]+\boldsymbol{G}_{s,k}\boldsymbol{\alpha}_{s,k} \tag{3.34}$$

$$\boldsymbol{G}_{s,k}=\left[\boldsymbol{G}_{s,k,1},\boldsymbol{G}_{s,k,2},\boldsymbol{G}_{s,k,3}\right] \quad \text{and} \quad \boldsymbol{G}_{s,k,i}=\begin{bmatrix} \frac{\partial P_{s,k,i}}{\partial X_s} & 0 & 0 \\ 0 & \frac{\partial P_{s,k,i}}{\partial Y_s} & 0 \\ 0 & 0 & \frac{\partial P_{s,k,i}}{\partial Z_s} \\ \frac{\partial P_{s,k,i}}{\partial Y_s} & \frac{\partial P_{s,k,i}}{\partial X_s} & \\ & \frac{\partial P_{s,k,i}}{\partial Z_s} & \frac{\partial P_{s,k,i}}{\partial Y_s} \\ \frac{\partial P_{s,k,i}}{\partial Z_s} & & \frac{\partial P_{s,k,i}}{\partial X_s} \end{bmatrix} \tag{3.35}$$

Substituting Eq. (3.34) into Eq. (3.25) yields the strain energy including flexural bending modes

$$\begin{aligned} U_{s,k}=&\frac{1}{2}\boldsymbol{X}_{s,k}^{\mathrm{T}}\left(\mathbf{I}_{24\times 24}-\boldsymbol{Q}_{s,k}^{\mathrm{T}}\right)\boldsymbol{K}_{s,k,0}\left(\mathbf{I}_{24\times 24}-\boldsymbol{Q}_{s,k}\right)\boldsymbol{X}_{s,k}-\boldsymbol{X}_{s,k}^{\mathrm{T}}\boldsymbol{F}_{s,k}^{0}+\frac{1}{2}\boldsymbol{X}_{s,k,0}^{\mathrm{T}}\boldsymbol{K}_{s,k,0}\boldsymbol{X}_{s,k,0}+\frac{1}{2}\boldsymbol{\alpha}_{s,k}^{\mathrm{T}}\boldsymbol{K}_{\alpha\alpha,k}\boldsymbol{\alpha}_{s,k}\\ &+\frac{1}{2}\boldsymbol{X}_{s,k}^{\mathrm{T}}\left(\mathbf{I}_{24\times 24}-\boldsymbol{Q}_{s,k}^{\mathrm{T}}\right)\boldsymbol{K}_{x\alpha,k}^{0}\boldsymbol{\alpha}_{s,k}+\frac{1}{2}\boldsymbol{\alpha}_{s,k}^{\mathrm{T}}\left(\boldsymbol{K}_{x\alpha,k}^{0}\right)^{\mathrm{T}}\left(\mathbf{I}_{24\times 24}-\boldsymbol{Q}_{s,k}^{\mathrm{T}}\right)\boldsymbol{X}_{s,k}-\boldsymbol{\alpha}_{s,k}^{\mathrm{T}}\boldsymbol{F}_{a,k}^{0} \end{aligned} \tag{3.36}$$

where

$$\boldsymbol{K}_{x\alpha,k}^{0}=\int_{-1}^{1}\int_{-1}^{1}\int_{-1}^{1}\boldsymbol{B}_{s,k}^{\mathrm{T}}\boldsymbol{D}_{s,k}\boldsymbol{G}_{s,k}\left|\boldsymbol{J}\right|d\xi_{s,k}d\eta_{s,k}d\zeta_{s,k} \tag{3.37}$$

$$\boldsymbol{K}_{\alpha\alpha,k}^{0}=\int_{-1}^{1}\int_{-1}^{1}\int_{-1}^{1}\boldsymbol{G}_{s,k}^{\mathrm{T}}\boldsymbol{D}_{s,k}\boldsymbol{G}_{s,k}\left|\boldsymbol{J}_{s,k}\right|d\xi_{s,k}d\eta_{s,k}d\zeta_{s,k} \tag{3.38}$$

$$\boldsymbol{F}_{a,k}^{0}=\left(\boldsymbol{K}_{xa,k}^{0}\right)^{\mathrm{T}}\boldsymbol{X}_{s,k,0} \tag{3.39}$$

Applying the principle of virtual work leads to the static equilibrium equation, such

that

$$\begin{aligned} \boldsymbol{K}_{xx,k}\boldsymbol{X}_{s,k} + \boldsymbol{K}_{x\alpha,k}\boldsymbol{\alpha}_{s,k} &= \boldsymbol{F}^{e}_{s,k} + \boldsymbol{F}^{0}_{s,k} \\ \boldsymbol{K}^{\mathrm{T}}_{x\alpha,k}\boldsymbol{X}_{s,k} + \boldsymbol{K}_{\alpha\alpha,k}\boldsymbol{\alpha}_{s,k} &= \boldsymbol{F}^{0}_{\alpha,k} \end{aligned} \tag{3.40}$$

where $\boldsymbol{K}_{xx,k} = \left(\mathbf{I}_{24\times 24} - \boldsymbol{Q}^{\mathrm{T}}_{s,k}\right)\boldsymbol{K}_{s,k,0}\left(\mathbf{I}_{24\times 24} - \boldsymbol{Q}_{s,k}\right)$, $\boldsymbol{K}_{x\alpha,k} = \left(\mathbf{I}_{24\times 24} - \boldsymbol{Q}^{\mathrm{T}}_{s,k}\right)\boldsymbol{K}^{0}_{x\alpha,k}$, and $\boldsymbol{F}^{e}_{s,k}$ is the external force.

Solving the incompatible displacement $\boldsymbol{\alpha}_{s}$ from the second equation in Eq. (3.40) yields,

$$\boldsymbol{\alpha}_{s,k} = -\boldsymbol{K}^{-1}_{\alpha\alpha,k}\left(\boldsymbol{K}^{\mathrm{T}}_{x\alpha,k}\boldsymbol{X}_{s,k} - \boldsymbol{F}^{0}_{\alpha,k}\right) \tag{3.41}$$

Substituting Eq. (3.41) into the first equation in Eq. (3.40) yields,

$$\boldsymbol{K}_{s,k}\boldsymbol{X}_{s,k} = \boldsymbol{F}^{0}_{s,K} + \boldsymbol{F}^{e}_{s,k} \tag{3.42}$$

where

$$\boldsymbol{K}_{s,k} = \boldsymbol{K}_{xx,k} - \boldsymbol{K}_{x\alpha,k}\boldsymbol{K}^{-1}_{\alpha\alpha,k}\boldsymbol{K}^{\mathrm{T}}_{x\alpha,k} \tag{3.43}$$

$$\boldsymbol{F}^{0}_{s,K} = -\boldsymbol{K}_{xa,k}\boldsymbol{K}^{-1}_{aa,k}\boldsymbol{F}^{0}_{a,k} + \boldsymbol{F}^{0}_{s,k} \tag{3.44}$$

The $\boldsymbol{F}^{0}_{s,K}$ is the equivalent elastic force in the proposed NPFEM, which considers incompatible shape functions for flexural bending modes.

Furthermore, assume that the velocity and acceleration of any point inside the element can also be interpreted by the nodal coordinate velocities and accelerations by the shape function $\boldsymbol{N}_{s,k}$ as

$$\frac{d\boldsymbol{r}}{dt}=\frac{d\boldsymbol{X}_s}{dt}=\boldsymbol{N}_{s,k}\frac{d\boldsymbol{X}_{s,k}}{dt}\quad\text{and}\quad\frac{d^2\boldsymbol{r}}{dt^2}=\frac{d^2\boldsymbol{X}_s}{dt^2}=\boldsymbol{N}\frac{d^2\boldsymbol{X}_{s,k}}{dt^2}\tag{3.45}$$

Accordingly, the kinetic energy T of the element is written as

$$T_{s,k}=\int_{V_{0,k}}\frac{1}{2}\left(\frac{d\boldsymbol{r}}{dt}\right)^T\frac{d\boldsymbol{r}}{dt}\rho_{s,k}dV=\frac{1}{2}\left(\frac{d\boldsymbol{X}_{s,k}}{dt}\right)^{\mathrm{T}}\boldsymbol{M}_{s,k}\left(\frac{d\boldsymbol{X}_{s,k}}{dt}\right)\tag{3.46}$$

$$\boldsymbol{M}_{s,k}=\int_{-1}^{1}\int_{-1}^{1}\int_{-1}^{1}\rho_{s,k}\boldsymbol{N}_{s,k}^{\mathrm{T}}\boldsymbol{N}_{s,k}\left|\boldsymbol{J}_{s,k}\right|d\xi_{s,k}d\eta_{s,k}d\zeta_{s,k}\tag{3.47}$$

where $\rho_{s,k}$ is the material density and $\boldsymbol{M}_{s,k}$ is the element mass matrix, respectively. The analytical expressions of the stiffness $\boldsymbol{K}_{s,k}$ and mass $\boldsymbol{M}_{s,k}$ matrices are not generally available, and they will be evaluated numerically using the Gaussian integral [88].

The dynamic equation of each element can be derived by the principle of virtual work,

$$\delta\left(U_{s,k}-T_{s,k}\right)-\delta\boldsymbol{X}_{s,k}^{\mathrm{T}}\left(\boldsymbol{F}_{s,k}^{e}+\boldsymbol{F}_{s,K}^{0}\right)=\delta\boldsymbol{X}_{s,k}^{\mathrm{T}}\left(\boldsymbol{M}_{s,k}\frac{d^2\boldsymbol{X}_{s,k}}{dt^2}+\boldsymbol{K}_{s,k}\boldsymbol{X}_{s,k}-\boldsymbol{F}_{s,k}^{e}-\boldsymbol{F}_{s,K}^{0}\right)=0\tag{3.48}$$

For an arbitrary $\delta\bar{\boldsymbol{X}}_{s,k}^{\mathrm{T}}$, the validity of Eq. (3.48) implies

$$\boldsymbol{M}_{s,k}\ddot{\boldsymbol{X}}_{s,k}+\boldsymbol{K}_{s,k}\boldsymbol{X}_{s,k}-\boldsymbol{F}_{s,K}^{0}-\boldsymbol{F}_{s,k}^{e}=\boldsymbol{0}\tag{3.49}$$

Considering the damping effect, Eq.(3.49) can be reformulated as

$$\boldsymbol{M}_{s,k}\ddot{\boldsymbol{X}}_{s,k}+\boldsymbol{K}_{s,k}\boldsymbol{X}_{s,k}+\boldsymbol{C}_{s,k}\dot{\boldsymbol{X}}_{s,k}-\boldsymbol{F}_{s,k}^{0}-\boldsymbol{F}_{s,k}^{e}=\boldsymbol{0}\tag{3.50}$$

where $\boldsymbol{C}_{s,k}=\alpha_s\boldsymbol{M}_{s,k}+\beta_s\boldsymbol{K}_{s,k}$ is the Rayleigh damping with damping coefficients (α_s, β_s).

The global finite element equation can be assembled by the standard assembly

procedure in the traditional FEM, such that

$$\boldsymbol{M}_s\ddot{\boldsymbol{X}}_s + \boldsymbol{K}_s\boldsymbol{X}_s + \boldsymbol{C}_s\dot{\boldsymbol{X}}_s - \boldsymbol{F}_s^0 - \boldsymbol{F}_s^e = \boldsymbol{0} \tag{3.51}$$

It is noteworthy that the definition of boundary conditions in the NPFEM deviates from conventional FEMs, where boundary conditions are specified by position coordinates and velocities.

3.3.2 Numerical Verification of a Cantilevered Regular Beam

The accuracy and effectiveness of the 8-node isoparametric hexahedral element in NPFEM are verified by static and dynamic analyses of a cantilevered rectangular beam, as shown in Figure 3-4. The physical properties and geometric parameters of the beam are given in Table 3-1. The numerical results are verified with the analytical solutions in two cases.

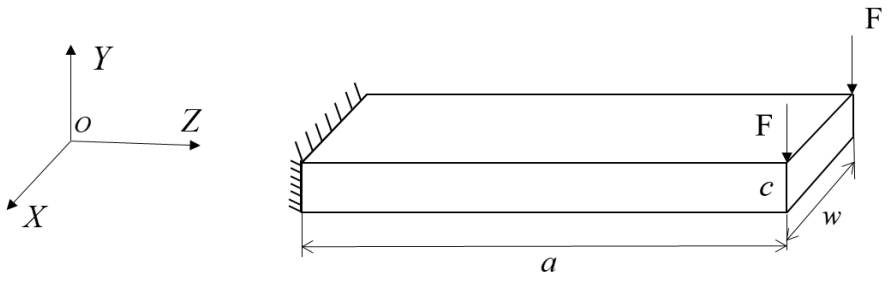

Figure 3-4. The boundary and loading conditions of a cantilevered rectangular beam.

Table 3-1 Physical properties and geometric parameters of the rectangular beam

Property	Symbol	Value	Parameter	Symbol	Value
Young's modulus	E	200 GPa	Beam length	a	20cm

Poisson ratio	υ	0.3	Beam width	w	10cm
Density	ρ	4,000 kg/m^3	Beam thickness	c	2cm

3.3.2.1 Static verification

The cantilevered beam is subjected to two static tip loads in the *Y*-axis direction $\boldsymbol{F} = [0,\ -100,\ 0]^{\mathrm{T}}\,\mathrm{kN}$ at its free end, as shown in Figure 3-4. The beam is modeled with different numbers of elements in the width, thickness, and length (W×T×L) direction to examine the convergence behavior of the newly proposed finite element.

First, simulations were conducted with varying element numbers in different directions, and the results are shown in Table 3-2 and Figure 3-5. The tip deflections calculated from the NPFEM are compared to the analytical solution for a cantilevered beam under large deflection conditions [89] in terms of relative error $e' = \left\| (x - x^*)/x^* \right\| \times 100\%$, where x and x^* are the NPFEM and analytical solutions, respectively. Compared to the solutions without incompatible modes in the element, using incompatible modes yields a rapid reduction in error as the number of elements along the length increases, underscoring the necessity of including these modes to accurately model the bending deformation of the beam with the solid element. Furthermore, the relative error converges to less than 1% once the number of elements exceeds ($2\times2\times14$), see Table 3-2. Extra elements in the thickness do not lead to a significant reduction in errors. For example, the relative error for the mesh of $2\times2\times16$ is 0.53%, while the errors of the meshes $2\times4\times16$ and $2\times6\times16$ with extra

elements in the thickness are 0.29% and 0.26%. Furthermore, the extra elements in the width direction result in only marginal improvement in the solution, e.g., the errors of the meshes $2\times4\times16$ and $4\times4\times16$ are 0.29% and 0.21%, respectively. This verifies the efficacy of the NPFEM in accurately resolving static elastic problems. Particularly, the convergence analysis shows that only two elements in the thickness direction are sufficient to accurately model the bending behavior. Consequently, the mesh of $2\times2\times16$ is used for the subsequent dynamic verification analysis.

Table 3-2 The nodal displacement at the tip of the beam.

Element Numbers (W×T×L)	NPFEM Solution (m)		Analytical Solution (m)	Relative Error of NPFEM with Incompatible Modes (%)
	Without Incompatible	With Incompatible		
2×2×4	-0.0114	-0.0349		8.96
2×2×6	-0.0183	-0.0367		4.05
2×2×8	-0.0233	-0.0374		2.34
2×2×10	-0.0266	-0.0377		1.52
2×2×12	-0.0288	-0.0379	-	1.05
2×2×14	-0.0303	-0.0380	0.0383	0.74
2×2×16	-0.0314	-0.0381		0.53
2×4×16	-0.0324	-0.0382		0.29
2×6×16	-0.0326	-0.0382		0.26
4×4×16	-0.0331	-0.0384		0.21

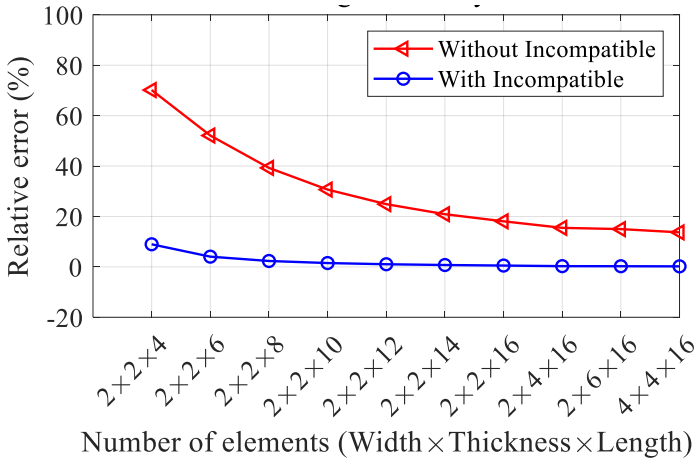

Figure 3-5 Convergence of NPFEM with and without incompatible modes.

3.3.2.2 Dynamic verification

Next, two periodic point loads $\boldsymbol{F} = [0, -5, 0]^{\mathrm{T}} \times \sin(200\pi t)$ are applied to the free end of the cantilevered beam, as shown in Figure 3-4. The beam is modeled using $(2 \times 2 \times 16)$ solid elements, with two elements in thickness, two in width, and 16 in length. The bending modal frequencies of the cantilevered beam are calculated by the NPFEM and analytical method [90], respectively, and the first three modal frequencies and shapes are shown in Table 3-3 and Figure 3-6. Compared with analytical solutions, the relative errors in modal frequency between the NPFEM and analytical solutions are less than 5%. This discrepancy is caused by the limitation of the solid element in approximating the beam bending [91,92]. Nevertheless, it is verified that the NPFEM solid element is capable of analyzing the dynamic characteristics of such structures. The frequency responses of the bending modes obtained from the nonlinear NPFEM are illustrated in Figure 3-7. The first peak

corresponds to the excitation frequency of the tip loads (100 Hz). Subsequent peaks represent the beam's first, second and third bending modes as expected.

Table 3-3 First three bending modal frequencies of the cantilevered rectangular beam

Mode Number	Frequency (Hz)		Error (%)
	NPFEM	Analytical Method	
1	589.7	571.1	3.26
2	3758.1	3579.2	5.00
3	8945.5	8838.8	1.21

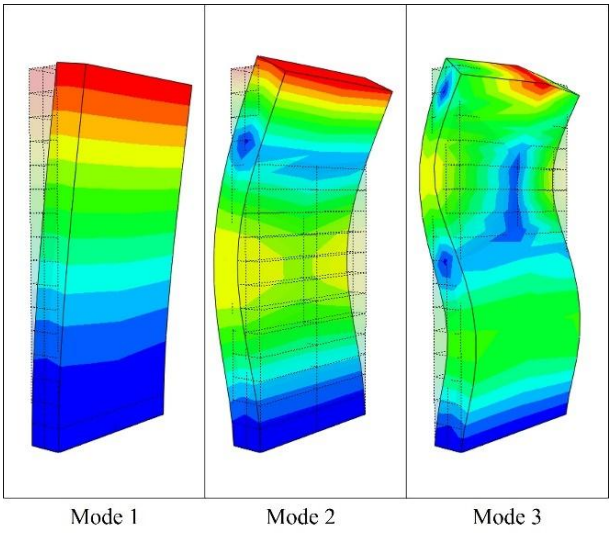

Figure 3-6 The first three bending modal shapes of the cantilevered rectangular beam.

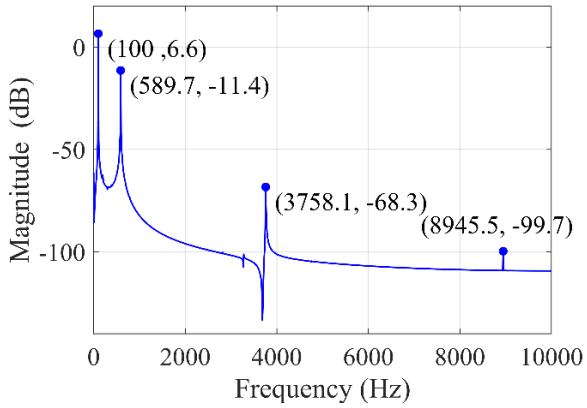

Figure 3-7 Frequency spectrum of flexural vibration of the beam.

In summary, the static and dynamic case studies verify that the proposed 8-node isoparametric hexahedral element in NPFEM is accurate for the dynamic analysis of regular-shaped structures.

3.3.3 Numerical Verification of a Twisted Blade

The static and dynamic analyses of a cantilevered twisted blade are carried out to further demonstrate the precision and effectiveness of the 8-node isoparametric hexahedral element in NPFEM. The results are validated with the commercial FE codes in two cases. Considering a cantilevered twisted blade, as shown in Figure 3-8, the physical properties and geometrical parameters of the blade are given in Table 3-4.

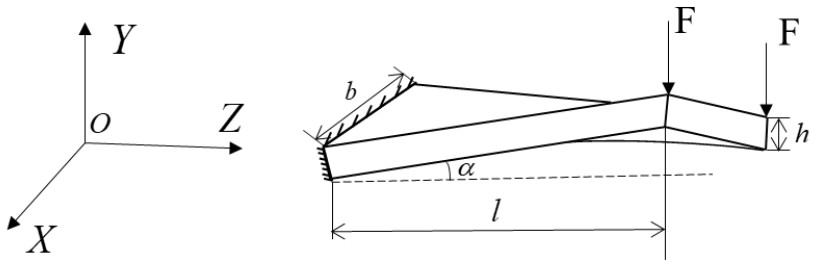

Figure 3-8 The boundary and loading conditions of a cantilevered blade.

Table 3-4 Physical properties and geometric parameters of the blade

Parameter	Symbol	Value	Parameter	Symbol	Value
Young's modulus	E	200GPa	Blade length	l	20cm
Poisson ratio	υ	0.3	Blade width	b	10cm
Density	ρ	4,000 kg/m^3	Blade thickness	h	2cm
Twist angle	α	30°	Radius @ blade root	R	5cm

3.3.3.1 Static verification

Let the cantilevered blade be fixed at one end and subjected to two static tip loads in the Y-axis direction $\boldsymbol{F} = [0,100,0]^{\mathrm{T}}\,\mathrm{kN}$ at its free end. The blade is modeled using the same number of solid elements used in Section 3.3.2, as depicted in Figure 3-9. Two elements are used in the thickness direction to facilitate the shear deformation caused by bending and two elements in the width direction to model the torsion deformation.

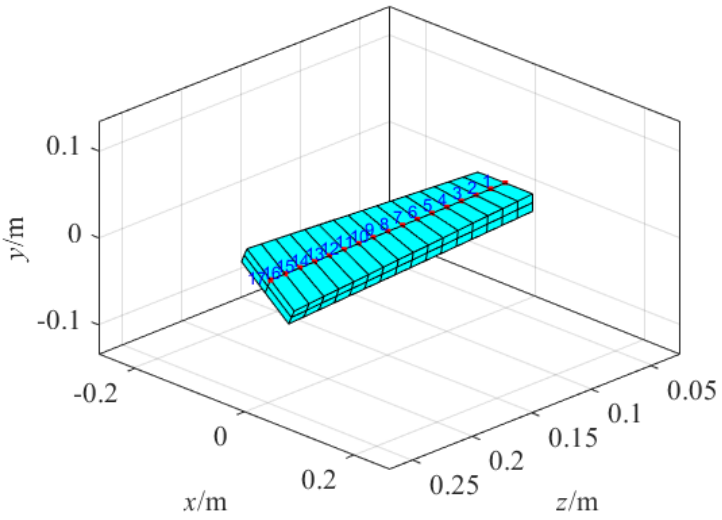

Figure 3-9 The FE mesh of the blade.

The analysis results are given in Table 3-5 and depicted in Figure 3-10. The displacement in the *Y*-axis (loading direction) along the central line (Nodes 1-17) of the blade at the top, middle and bottom layers is shown in Figure 3-10. The results of the NPFEM are almost identical to the results of the commercial FE-codes. To compare quantitatively, the displacements of the mid-free end at the top, middle, and bottom layers in the *Y*-axis are given together with the results from ANSYS in Table 3-5. It shows the relative error is less than 0.6%. Additionally, as shown in Table 3-6, a comparison of the Von Mises stress at Nodes 4-12 between NPFEM and ANSYS is performed. The results indicate that the relative error is less than 1.2%. This further validates the efficacy of the NPFEM in accurately resolving static elastic problems of complicated structures.

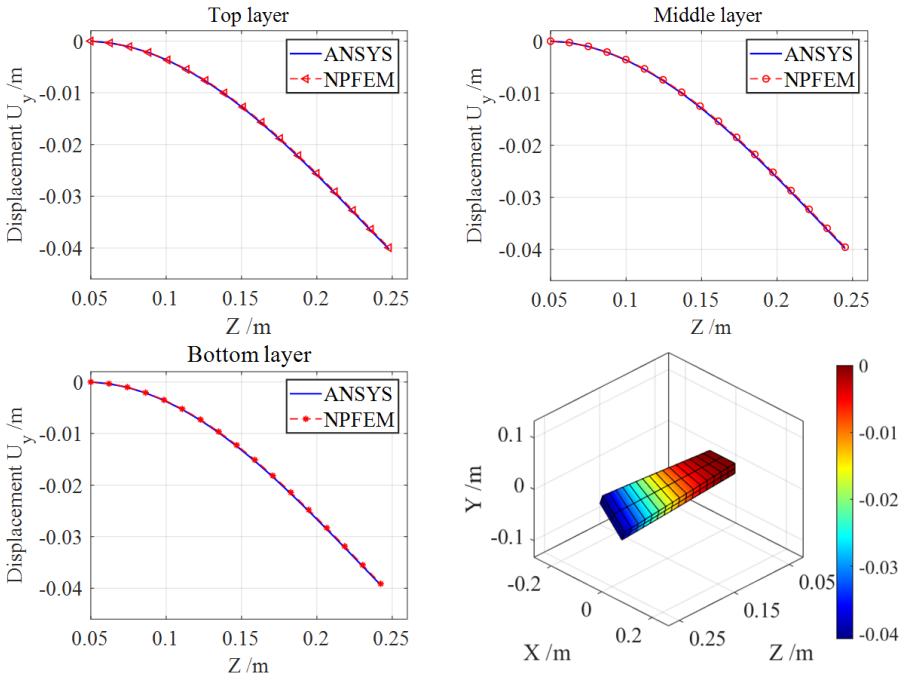

Figure 3-10 The nodal displacements U_y in the labelled section of the blade.

Table 3-5 The nodal displacement of the blade tip (Node 16).

Position	ANSYS (m)	NPFEM (m)	Relative Error (%)
Top	-0.0402	-0.0400	0.50
Middle	-0.0398	-0.0396	0.50
Bottom	-0.0394	-0.0392	0.51

Table 3-6 The Von Mises stress of 5 selected nodes.

Position	ANSYS (GPa)	NPFEM (GPa)	Relative Error (%)
Node 4	4.58	4.54	0.76
Node 6	4.06	4.02	0.91
Node 8	3.42	3.40	0.85
Node 10	2.68	2.66	0.73
Node 12	1.89	1.87	1.13

3.3.3.2 Dynamics verification

Next, let the cantilevered blade in Figure 3-8 be subjected to two periodic loads at its free tip. Assume the dynamic loads are sinusoidal, such as, $\boldsymbol{F} = [0, 5, 0]^{\mathrm{T}} \times \sin\left(200\pi t\right)$ kN. The blade is modeled with the same element mesh used in Section 3.3.3.1. The dynamic response of the cantilevered blade is analyzed by the NPFEM and ANSYS, respectively.

First, modal analysis was conducted using both NPFEM and ANSYS. The first six modal frequencies were determined and shown in Table 3-7. It shows that the frequency differences calculated by the NPFEM and ANSYS are less than 0.21%, proving that the proposed NPFEM 3D isoparametric element is accurate in frequency analysis. Moreover, the modal shapes of the first 6 modes are shown in Figure 3-11. Because of the twisted geometry, the modal shapes show the combination of bending, torsional, and in-plane shear deformation. For instance, the first and fourth modes are dominantly bending, the second and fifth modes are dominantly torsional, and the third and sixth modes are dominantly in-plane shear deformation.

Table 3-7 The first six modal frequencies of the cantilevered blade

Mode number	Frequency (Hz)		Error (%)
	NPFEM	ANSYS	
1	576.2	577.4	0.21
2	2313.0	2314.4	0.06
3	2451.0	2447.5	0.14
4	3887.8	3895.5	0.20
5	8080.1	8063.2	0.21
6	8970.7	8970.3	0.01

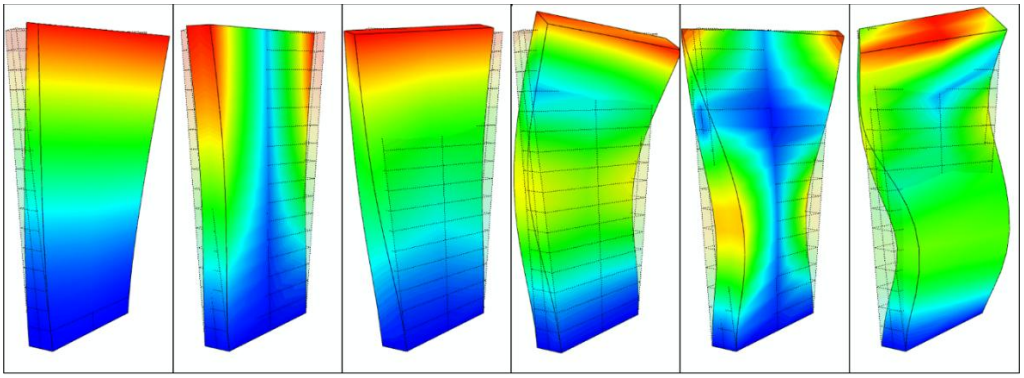

Figure 3-11 Modal shapes of the blade. The dashed lines represent the undeformed blade.

Then, the dynamic responses of the blade subjected to the periodic loads are shown in Figure 3-12 and Figure 3-13. Figure 3-12 presents the time histories of the displacements of node No. 17 in the *X* and *Y*-axis directions from both the NPFEM and the FE-code analysis. The NPFEM results align precisely with those from ANSYS, highlighting the 3D NPFEM's capability to accurately solve elastodynamic problems of solids. Obviously, it shows the blade experiences both bending (*Y*-axis) and torsional (*X*-axis) deformation under the external load in the *Y*-axis due to its twisted shape. The peak deflection on the *Y*-axis is roughly 7.5 times greater than that on the *X*-axis due to the twisted geometry of the blade.

From Figure 3-12, the associated frequency responses obtained by both the NPFEM and ANSYS are calculated and shown in Figure 3-13. The initial peaks in the *X* and *Y* axes responses correspond to the excitation frequency of the applied loads at 100Hz as expected. In the *X*-axis response, Figure 3-13(a), the second, third, and fourth peaks represent the

blade's first, second, and fourth modes, the bending induced torsional deformation plus the pure torsional deformation. In the *Y*-axis response, Figure 3-13 (b), the second peak represents the blade's first mode - bending deformation and the third peak represents the blade's fourth mode – dominant bending with slight torsional deformation. The slight discrepancies between the blade's modal frequencies shown in Figure 3-13 and those listed in Table 3-7 are attributed to the inclusion of nonlinear stiffness in the time-domain analysis because the modal frequencies in Table 3-7 are obtained by the eigenvalue analysis, which uses the blade's linear stiffness only.

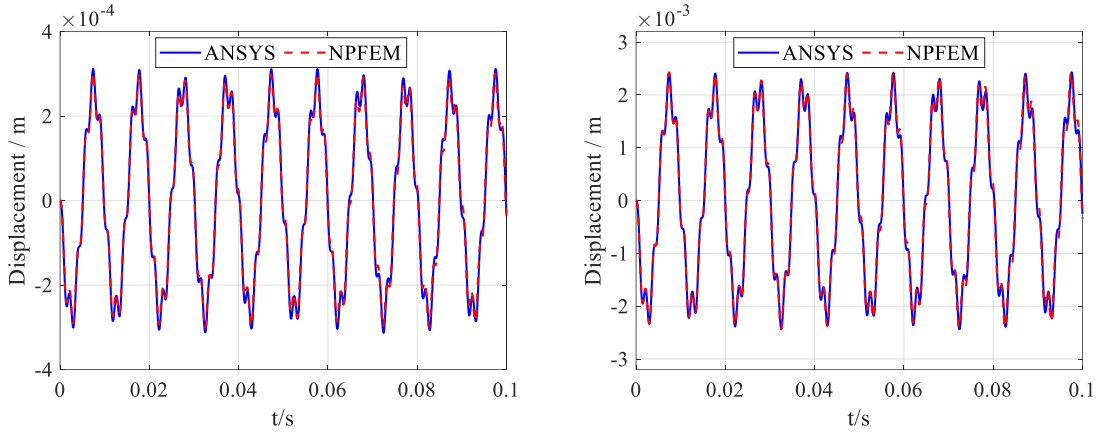

(a) x-axis (b) y-axis

Figure 3-12 The time histories of nodal positions of the blade tip (Node No.17) in the local frame.

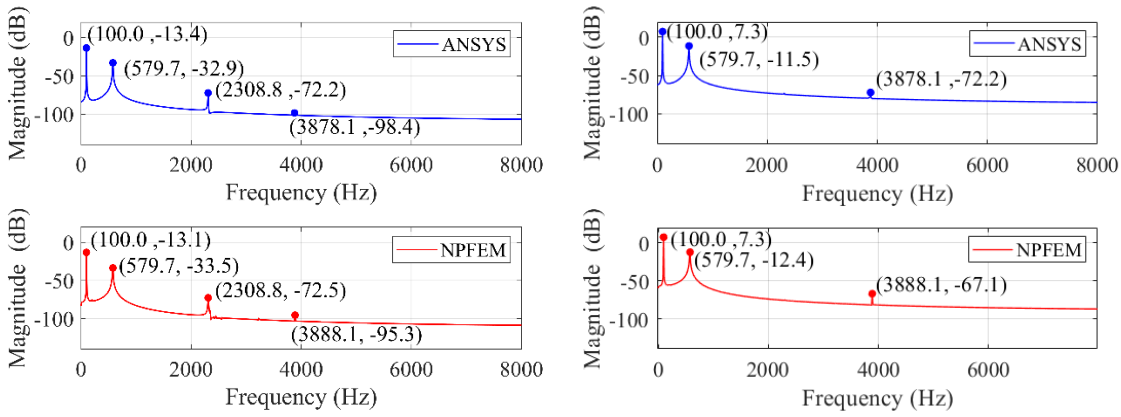

(a) x-axis (b) y-axis

Figure 3-13 The frequency spectra of the blade tip (Node No.17) subjected to the period tip loads.

3.3.4 Dynamic Analysis of a Rotating Twisted Blade

Finally, the proposed element is applied tto the analysis of a typical turbine disc-blade system, as illustrated in Figure 3-14. The blade is a twisted thin beam. Its root is attached to the turbine disc with a zero-offset angle. Two coordinate systems are used to describe the system motion as shown in Figure 3-14. The origin of the global inertial frame *OXYZ* is at the rotation center of the disc with the *X*-axis aligned with the rotation axis. The local body-fixed frame *oxyz* is fixed to the blade with its origin at the center of the blade's root surface, the *x*-axis aligned with its root edge, the *y*-axis perpendicular to the root edge, and the *z*-axis along its length. The disc is rotating about its shaft at an angular velocity ω and is not modeled by FEM. Instead, the disc is treated as a dynamic boundary condition. Unlike conventional FE analysis, where the blade is taken off the disc with its root fixed,

the elastic responses of the blade will be analyzed directly by rotating it with the disc using the NPFEM. No material damping is considered. The blade has the same physical properties and geometric parameters given in Section 3.3.3.

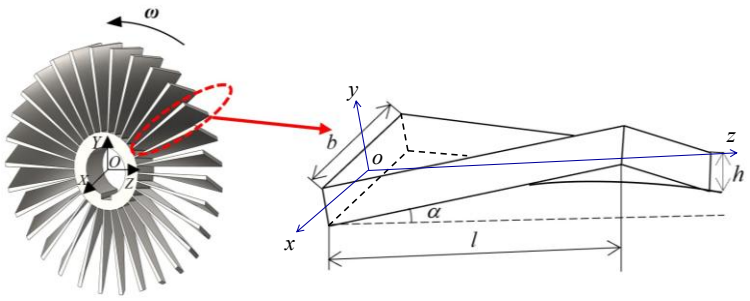

Figure 3-14 Schematic of a twisted rotating turbine blade

Next, assume the disc in Figure 3-14 is accelerated from zero to a constant angular velocity of $300\pi\,\text{rad/s}^2$ with a constant angular acceleration of $30000\pi\,\text{rad/s}^2$ in 0.01s. such that,

$$\omega = \begin{cases} 30000\pi t\ rad/s & t < 0.01s \\ 300\pi\ rad/s & t \geq 0.01s \end{cases}$$

The blade is modeled with the same FE mesh ($2\times2\times16$ elements) used in Section 3.3. The time histories of the blade tip's positions (Node No. 17) in the global Y and Z axes are shown in Figure 3-15. As expected, they reflect dominantly the rigid-body rotation of the blade, and the elastic deformation of the blade is hard to see. Subtracting the rigid-body motion of the blade tip, the elastic dynamic responses of the blade tip in the local body-fixed coordinate frame are shown in Figure 3-16. It clearly shows that the blade exhibits a typical transient response of a thin plate subjected to base acceleration. The angular

acceleration causes the blade to deflect in the *x* and *y* axes, namely torsional and bending deformation. After the initial acceleration phase, the blade continues to vibrate in the *x* and *y* axes because no material damping is considered in the analysis. Meanwhile, the blade also vibrates in its length direction (*z*-axis) due to the centrifugal acceleration. The deformation along the z-axis reflects the blade's elongation under centrifugal acceleration, leading to a stiffening effect. These results show the capability of the NPFEM to precisely extract elastic deformation from the rigid-body rotation motion.

Next, the frequency responses of the vibrating blade in the local frame are depicted in Figure 3-17. A comparison between Figure 3-17 and Figure 3-13 reveals two significant differences in the frequency responses between the rotating and stationary blades. First, the fundamental frequency increases due to the centrifugal stiffening effect of rotation, which effectively stiffens the blade as reported in Refs [93,90]. For example, the frequencies of the bending modes increase from 579.7Hz and 3888.1Hz to 589.9Hz and 3909.6Hz, respectively, and the torsional mode frequency increases from 2308.8Hz to 2314.8Hz. Second, the axial vibration of the blade exhibits a '2n' superharmonic resonance, i.e., the resonance of 1179.9Hz is 2 times the first modal frequency of 589.9Hz. This is attributed to its irregular shape and rotational motion [94–96]. These findings highlight the need for the NPFEM to provide accurate simulations, especially in scenarios involving complex nonlinear dynamic behavior in the rotating elastic solid. It also demonstrates the NPFEM's capability to solve such complex nonlinear dynamic problems.

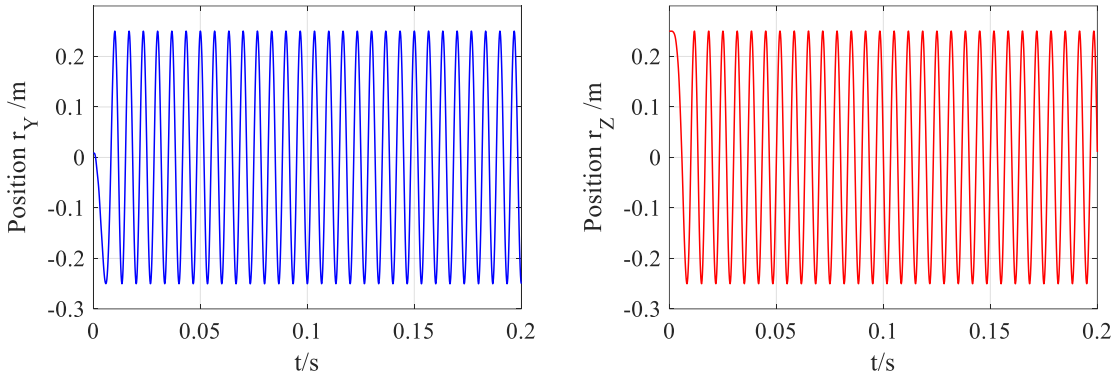

(a) Y-axis (b) Z-axis

Figure 3-15 Time histories of the blade tip's position (Node No. 17) in the global frame.

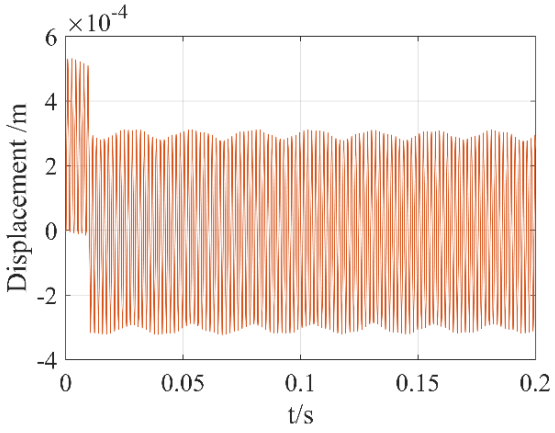

(a) x-axis

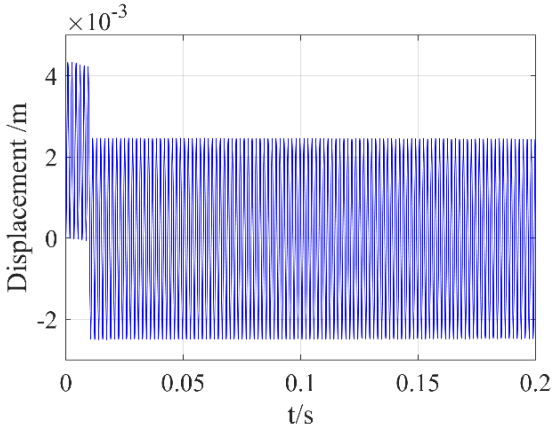

(b) *y*-axis

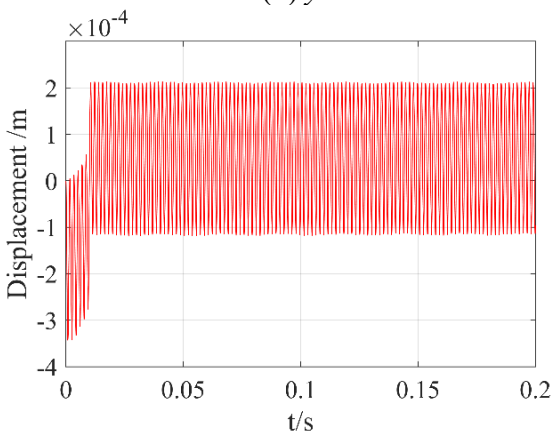

(c) *z*-axis

Figure 3-16 Time history of elastic displacement of the blade tip (Node No.17) in the local body-fixed coordinate frame.

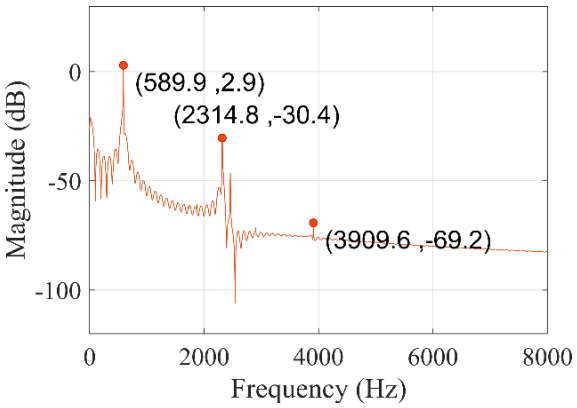

(a) *x*-axis

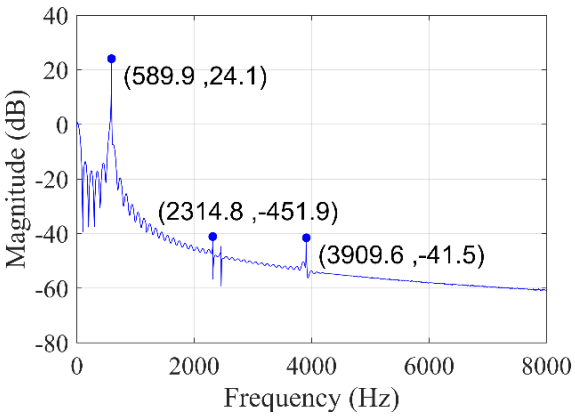

(b) *y*-axis

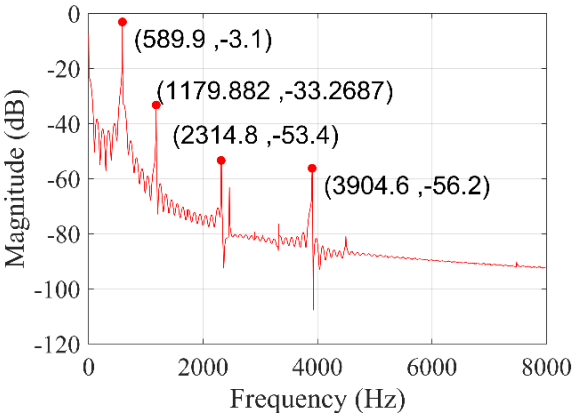

(c) *z*-axis

Figure 3-17 Frequency spectrum of the vibrating blade in the local body-fixed coordinate frame.

3.4. Full elastic Dynamic Model of the Tethered Space System

In this study, the tethered space system is represented as a combination of elastic bodies interconnected by an elastic tether. The overall system is discretized into solid elements for the spacecraft components and tensile elements for the tether. The expression of the dynamic equation of the element can be expressed in a unified matrix form as

$$\boldsymbol{M}_{h,j}\ddot{\boldsymbol{X}}_{h,j} + \boldsymbol{K}_{h,j}\boldsymbol{X}_{h,j} + \boldsymbol{C}_{h,j}\dot{\boldsymbol{X}}_{h,j} - \boldsymbol{F}^{d}_{h,j} - \boldsymbol{F}^{g}_{h,j} - \boldsymbol{F}^{0}_{h,j} = \boldsymbol{0} \tag{3.52}$$

where subscript $h = \{s,t\}$ represents the element type, s means solid element and t means tether element, and subscript j is the element number. $\boldsymbol{F}^{d}$ and $\boldsymbol{F}^{g}$ are the atmospheric drag force and the gravity force of the element, respectively. The detailed expression can be found in Ref. [97].

Since both the solid-element model of the spacecraft and the tether-element model are formulated in terms of nodal coordinates, the global dynamic equation of the entire tethered space system can be obtained by directly assembling the elemental equations of motion according to the standard finite element assembly procedure. Consequently, the governing dynamic equation of the system can be written as,

$$\boldsymbol{M}\ddot{\boldsymbol{X}} + \boldsymbol{K}\boldsymbol{X} + \boldsymbol{C}\dot{\boldsymbol{X}} - \boldsymbol{F}^{d} - \boldsymbol{F}^{g} - \boldsymbol{F}^{0} = \boldsymbol{0} \tag{3.53}$$

where $\boldsymbol{M}$, $\boldsymbol{K}$ and $\boldsymbol{C}$ are the mass matrix, stiffness matrix and damping matrix of the TSS, respectively. $\boldsymbol{F}^{d}$ and $\boldsymbol{F}^{g}$ are the atmospheric drag force and the gravity force of the entire

system, respectively. $\boldsymbol{F}^0$ is the unique equivalent elastic force term in the NPFEM approach.

3.5. Numerical Simulation

3.5.1 Steady Orbital Motion of Tethered Spacecraft System

In this case, simulations were performed using both the conventional rigid-flexible model [98] and the proposed full elastic model to compare their predicted dynamic responses. Initially, the TSS is assumed to operate in a 600km circular orbit with an undeformed tether length of 5000m. It is deployed in a straight-line configuration in the equatorial orbital plane and aligned with the local vertical. As shown in Figure 3-18, the main spacecraft and the sub-spacecraft are each discretized into four solid elements. Based on the convergence analysis conducted in previous studies [99], the tether is discretized into eight finite elements. Two body-fixed reference frames $o_m x_m y_m z_m$ and $o_s x_s y_s z_s$ are defined with their origin attached to the centers of mass of the main and the sub spacecraft, respectively. These axes are initially parallel to, and oriented in the same directions as, the ECI *O-XYZ* frame. The initial positions of the mass centers of the two spacecraft are specified as $[0, 6980637.8, 0]^{\mathrm{T}}$ (main spacecraft) and $[0, 6975636.2, 0]^{\mathrm{T}}$ (sub-spacecraft) in the ECI *O-XYZ* frame, respectively. Euler angles are adopted to describe the attitudes of each spacecraft, which are extracted from their nodal coordinates. Physical parameters of the TSS are listed in Table 3-8, and the tether's mechanical properties are listed in Table

3-9. The gravity field model used in the simulation is EGM2008 model [100] with up to degree 35 and order 35 and the atmospheric model NRLMSISE-00 [101] is used to calculate atmospheric drag. The governing equations of the TSS are solved using the generalized implicit integration scheme [102]. The time step is 0.00001s. The simulation results are shown in Figs. 3-8.

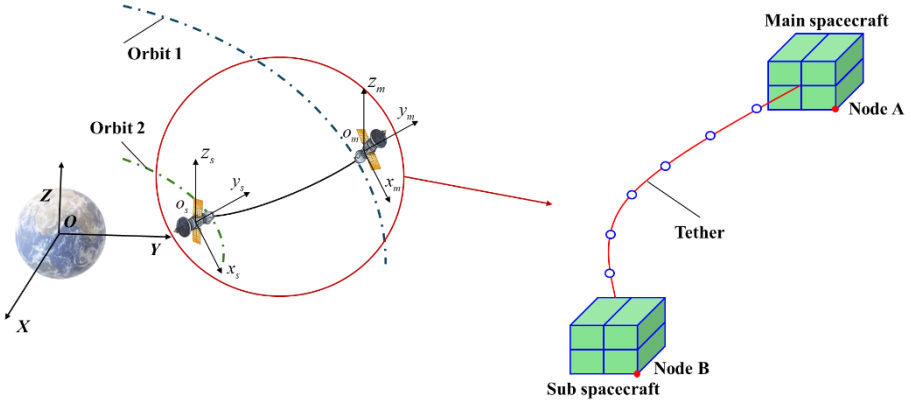

Figure 3-18 Schematic and discretized model of the TSS.

Table 3-8 Physical parameters of the TSS

Parameter	Value
Density of the spacecraft	2700 kg/m^3
The size of the main spacecraft	0.8m×0.8m×0.8m
The size of Sub-spacecraft	0.8m×0.8m×0.8m
Tether length	5000 m

Table 3-9 Tether's properties

Parameter	Value
Tether cross-sectional area	1.9635x10^{-7} m^2
Tether density (Aluminum)	2700 kg/m^3
Tether Young's Modulus	72 GPa
Tether damping coefficient (α_t, β_t)	(0,0.0015)

First, the variation of orbital altitude (ΔR) and out-of-plane motion (ΔZ) of nodes A and B of both main and sub-spacecraft (shown in Figure 3-18), as well as the mid-node of the tether, are shown in Figure 3-19. The proposed full elastic model yields results in good agreement with those of the conventional rigid-flexible model, confirming the accuracy of the proposed method in the orbital dynamic analysis of TSS. Additionally, both A and B nodes exhibit noticeable altitude and out-of-plane fluctuations. These phenomena stem from gravitational disturbances resulting from the non-ideal gravity model, specifically the gravity gradient and Earth's oblateness, which induce the out-of-plane coupling and prevent the TSS orbit from maintaining a closed circular geometry in the equatorial plane. Notably, the altitude and out-of-plane fluctuations of the mid-node of the tether are almost identical to those of nodes A and B. This suggests that the dimensions of TSS (5000 m) are too small relative to the orbital scale, resulting in approximately uniform gravitational effect across both satellites and the tether.

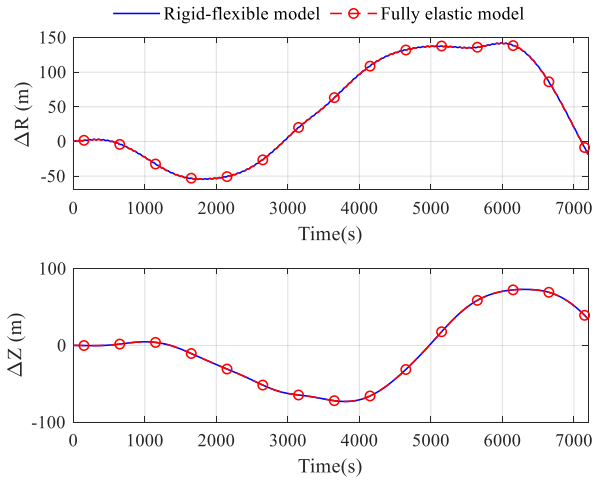

(a) Main spacecraft

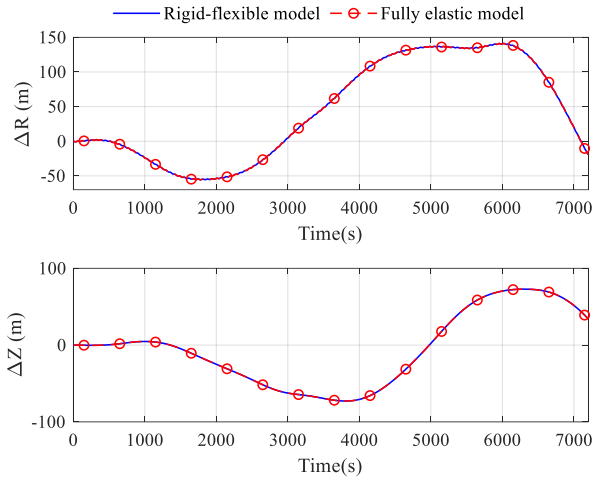

(b) Sub spacecraft

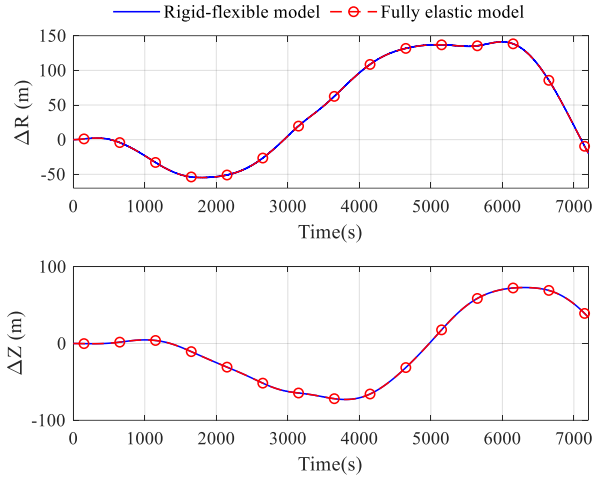

(c) Mid-node of the tether

Figure 3-19 Time histories of orbital altitude variation and out-of-plane motion of spacecraft and mid-node of the tether: (a) Main spacecraft; (b) Sub spacecraft; (c) Mid-node of the tether.

Next, the attitude motions of the two spacecraft, defined by the rotation of their body-fixed local frames relative to the ECI frame, were reconstructed from the nodal positions

and velocities via Orthogonal Procrustes Analysis [103,104]. This method is also adopted in the post-processing of the subsequent simulations in this chapter. As shown in Figure 3-20 and Figure 3-21, both models predict an approximately linear increase in the yaw angles of the two spacecraft, reflecting the orbital motion of the tethered space system, while the roll and pitch angles remain close to zero because no external torque disturbance is applied about the *x*- and *y*-axes. However, compared with the conventional rigid-flexible model, the proposed full elastic model yields more accurate rotational responses, particularly in roll, where the rigid-flexible formulation exhibits a small but noticeable accumulated deviation during long-duration simulation. This discrepancy is mainly attributed to the conventional rigid-flexible formulation, in which the rigid spacecraft and flexible tether are coupled through artificial interface constraints and approximate reduced representations, so that small numerical inconsistencies may accumulate over time and appear as spurious attitude drift [105–107], whereas the full elastic model provides a more consistent and numerically stable description of the coupled dynamics. Furthermore, these results also confirm that the NPFEM model accurately captures the orbital characteristics of the TSS, even though orbital dynamics is not explicitly included in NPFEM formulation.

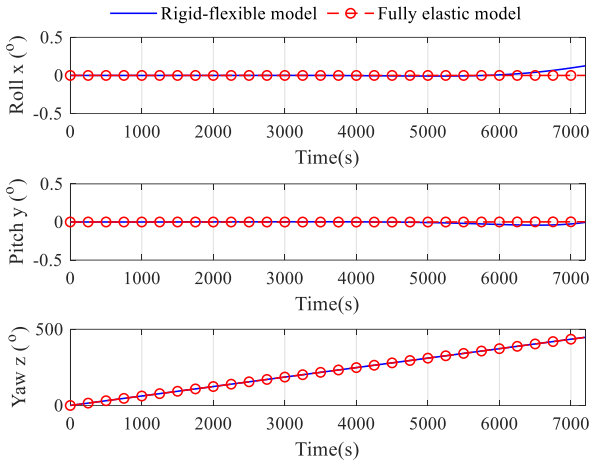

Figure 3-20 Time histories of attitudes of the main spacecraft in ECI frame.

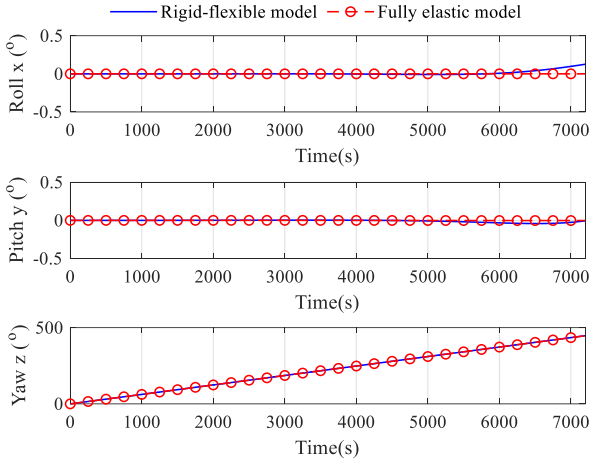

Figure 3-21 Time histories of attitudes of the sub spacecraft in the ECI frame.

In addition to the rigid-body orbital motion of the TSS, the elastic deformation of the tether is shown in Figure 3-22 and Figure 3-23. As shown in Figure 3-22, the time histories of the tether length variation predicted by the full elastic model and the rigid-flexible model are highly consistent, with both exhibiting a mean elongation of approximately 1.88 m caused by the differential gravitational force between the main satellite and the subsatellite.

The subsequent variation, ranging from 5001 to 5002.75 m, is mainly attributed to gravity-gradient perturbations along the orbit. Figure 3-23 further presents the tension variations in all tether elements predicted by the full elastic model. The tether remains taut throughout the orbital motion, with the tension and length exhibiting the same periodic fluctuations consistent with its elastic longitudinal vibration modes. These oscillations result from the interaction between the tether's elastic response and the periodic variation of the gravity gradient.

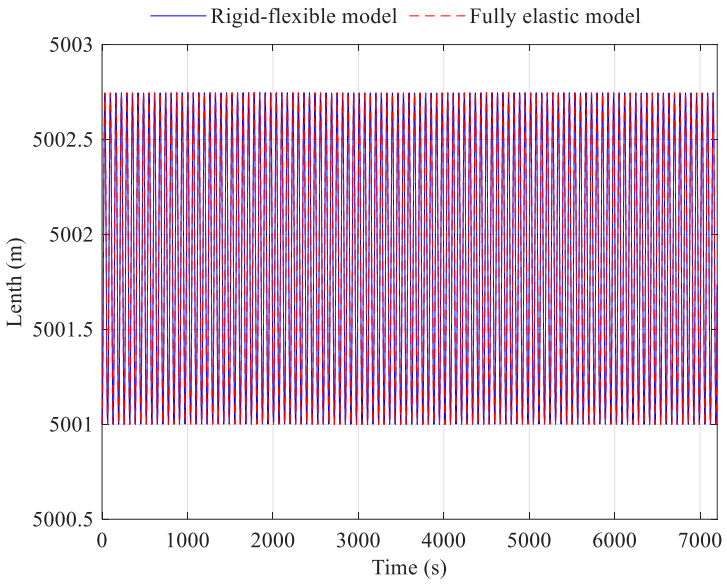

Figure 3-22 Time histories of the tether length.

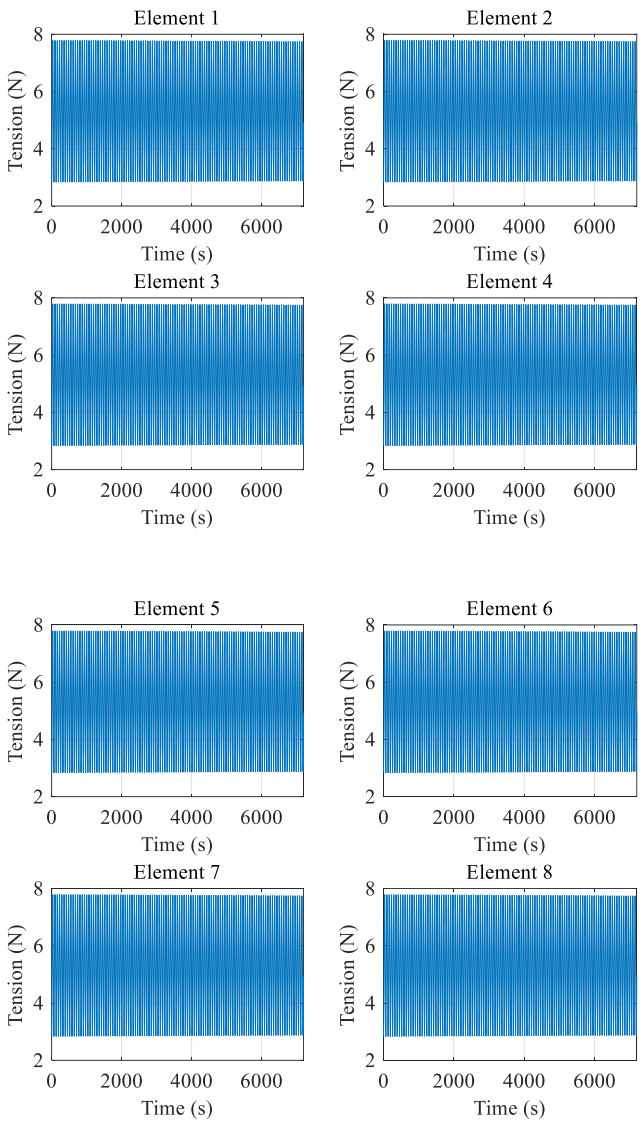

Figure 3-23 Tether tension of each tether element.

Finally, Figure 3-24 presents the time histories of the von Mises stress at the connection nodes between the tether and the two spacecraft. Since the natural frequency of the spacecraft structure is significantly higher than the characteristic frequency of the tether tension variation, the stress response is dominantly excited mainly by the tether vibration,

and its dominant frequency is therefore similar to that of the tether dynamics. The results show that the maximum von Mises stress reaches 3.7 MPa during on-orbit motion. Consequently, these results confirm that the NPFEM-based elastic TSS model effectively and accurately captures the coupled translational, rotational, and elastic dynamics of the TSS, providing a robust approach for orbital-structural coupled dynamic analysis of TSS.

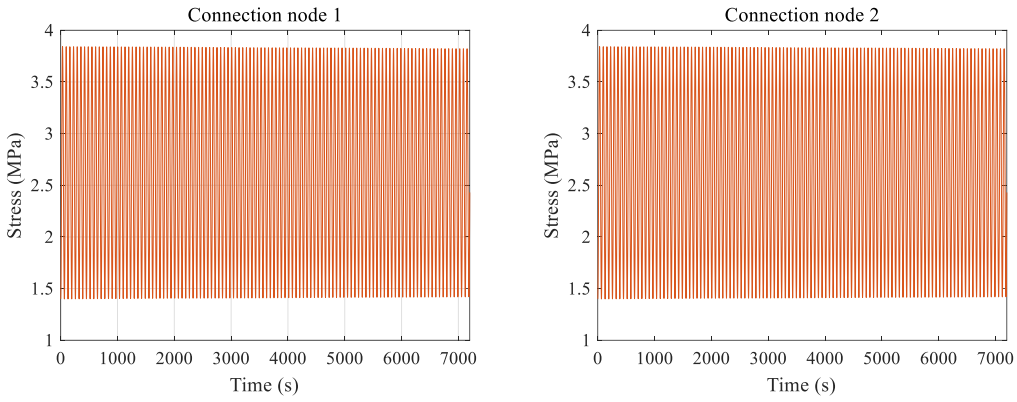

(a) (b)

Figure 3-24 Time histories of the von Mises stress at the connection nodes between the tether and spacecraft: (a) Connection node between the tether and main spacecraft; (b) Connection node between the tether and sub spacecraft.

3.5.2 Dynamic Analysis of Momentum Exchange Tether for Cross-Orbit Payload Delivery

Momentum-exchange tethers are a specialized type of TSS, proposed for cross-orbit payload delivery as shown in Figure 3-25. This maneuver is accomplished by exploiting

the rotational motion of the TSS. A rotating tethered system captures a payload in a lower orbit and subsequently releases it after the payload has reached a higher orbit. During this process, part of TSS angular momentum is transferred to the payload, causing the TSS to lose angular momentum and consequently experience a reduction in orbital velocity and altitude.

Similar to Section 3.5.1, the main spacecraft is discretized into four solid elements, while the tether is represented by eight tether elements, as shown in Figure 3-25. However, the payload and sub spacecraft are modeled as a single lumped point mass, justified by their significantly smaller mass and size relative to the main spacecraft. Payload release is modeled in the simulation by reducing the mass amount of this point mass during the maneuver.

As shown in Figure 3-25, the center of mass of the main spacecraft is assumed to be in a circular Earth orbit within the equatorial orbital plane at an altitude of 600 km. The tether is initially aligned along the *Y*-axis in the ECI frame, with the payload in the lower orbit. A body-fixed reference frame $oxyz$ is defined with its origin attached to the center of mass of the main spacecraft, and its axes aligned with the spacecraft's principal axes of inertia. Initially, these axes are parallel to and oriented in the same directions as the ECI *O-XYZ* frame.

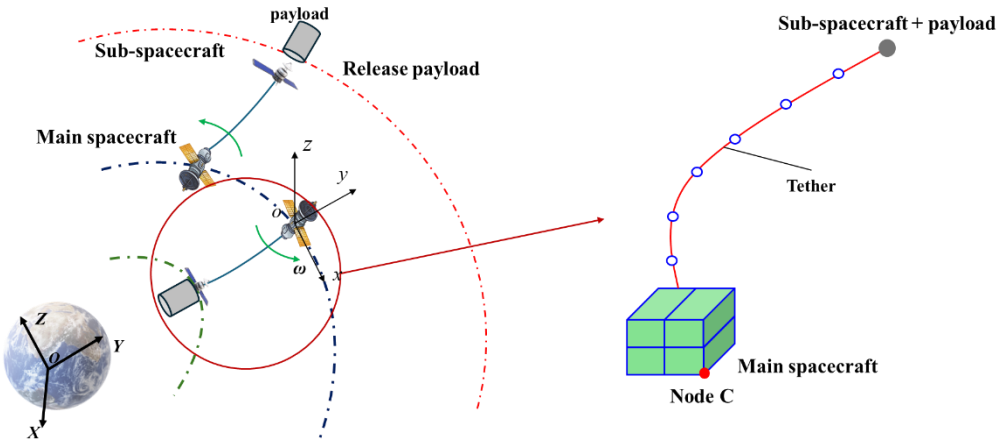

Figure 3-25 The schematic and the discretized model of momentum-exchange tethers

Table 3-10 Physical parameters of the momentum exchanged TSS

Parameter	Value
Density of the main spacecraft	2700 kg/m^3
The size of the main spacecraft	0.8m×0.8m×0.8m
The mass of the sub spacecraft	11.6kg
The releasing payload	10kg
Tether length	5000 m

The initial position of the center of mass of the main spacecraft is specified as $[0, 6978137, 0]^{\mathrm{T}}$ in the ECI *O-XYZ* frame. Its attitude is described using the Euler angles of the body-fixed reference frame ^{oxyz} relative to the ECI frame, which are derived from the nodal positions of the spacecraft. The corresponding angular velocities are calculated from the nodal coordinates and velocities of the spacecraft. The physical parameters of the momentum-exchange TSS are listed in Table 3-10, and the tether properties are identical to those defined in Table 3-9. The gravity and atmospheric models are the same as those used in Section 3.5.1. The governing equations of the system are also solved by the

generalized implicit integration scheme [102]. The simulations are performed with a time step of 0.00001s.

With the payload already captured by the sub spacecraft at the beginning of the simulation, the TSS is assumed to spin with a constant spin rate $\omega = 0.016\ rad/s$ initially. The tether is initially straight and aligned with the local vertical, placing the payload in a lower orbit than the main satellite. The payload is released upon reaching its high orbital point at the time instant of 400s, and the simulation continues for another eight spinning cycles of the TSS after payload release.

As shown in Figure 3-26, the time histories of the orbital altitude variation and out-of-plane motion of Node C on the main spacecraft (as labeled in Figure 3-25), the tether mid-node, and the mass point of the sub spacecraft exhibit a pronounced relative shift after payload release, thereby illustrating their relative dynamics before and after the payload-release event. Compared to the case in Section 3.5.1, the orbital altitude exhibits a pronounced change following the payload release, due to the change in mass distribution in TSS. In contrast, the out-of-plane motion remains effectively unchanged, reaffirming that this component of the motion arises primarily from gravitational perturbations rather than from the payload release itself.

Based on the nodal positions and velocities, the attitude angles and angular velocities of the main spacecraft relative to the ECI frame are subsequently derived and shown in Figure 3-27 and Figure 3-28. The attitude change is not significant, see Figure 3-27, for two reasons: (i) the disturbance caused by payload release lies within the orbital plane, so

the out-of-plane rotation (roll and pitch) is unaffected; and (ii) the induced yaw disturbance is negligible relative to the system's orbital angle because the payload mass is too small compared with that of the main spacecraft. However, the results demonstrate that payload release produces a distinct disturbance in the main spacecraft angular velocity, see Figure 3-28. This is attributable to the change of mass distribution and corresponding change in TSS angular-momentum of inertia, again reflecting the constraints imposed by angular-momentum conservation.

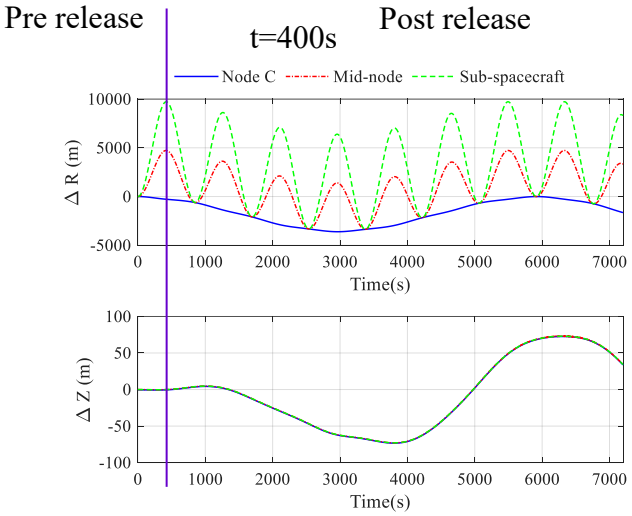

Figure 3-26 Time histories of orbital altitude variation and out-of-plane motion of Node C on the main spacecraft, Mid-node of the tether and the mass point of the sub spacecraft.

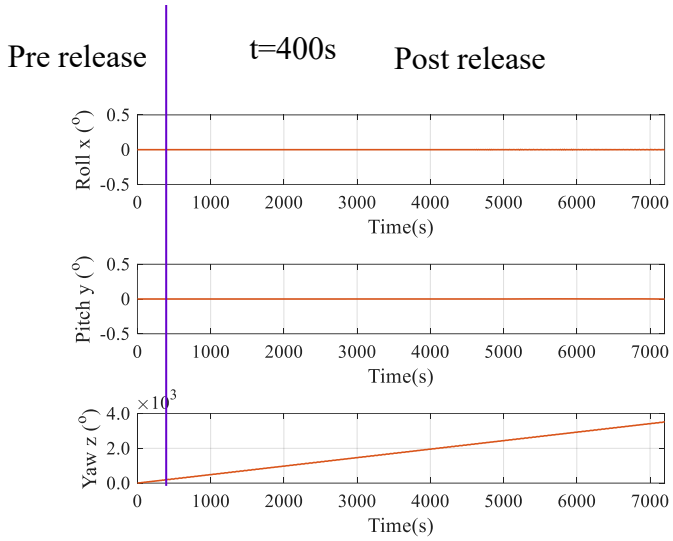

Figure 3-27 Time histories of the attitudes of the main spacecraft in ECI frame.

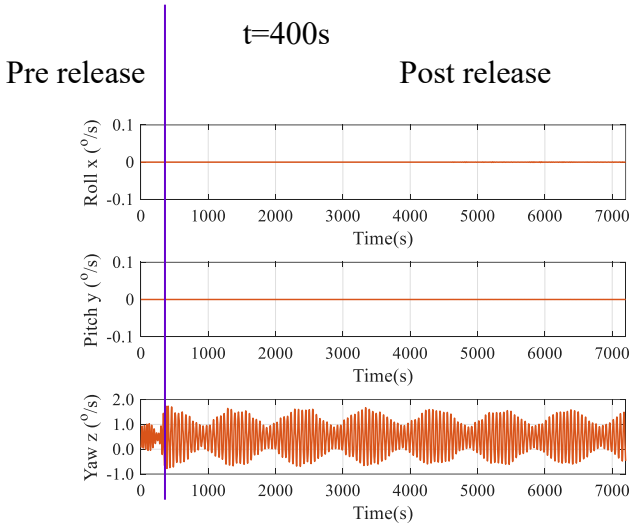

Figure 3-28 Time histories of the angular velocities of the main spacecraft in ECI frame.

Figure 3-29 illustrates the time histories of the tether length, and Figure 3-30 further presents the corresponding tension response. Following payload release at 400 s, the tether elongation shows a significant decrease due to the reduction in centrifugal force resulting

from the loss of payload mass (see Figure 3-29). Correspondingly, the tension exhibits a noticeable reduction too. Nevertheless, the tension remains strictly positive over the entire spin time, indicating that the tether sustains a continuously taut state and effectively precludes any onset of slackening or structural disengagement. The time histories of the von Mises stress at the tether–spacecraft connection nodes are further presented in Figure 3-31. The results show that the maximum von Mises stress reaches 7.4 MPa, and that the stress at the connection nodes decreases significantly after payload release. In addition, as depicted in Figure 3-32, the tether geometric configuration reveals that the tether undergoes only moderate elastic libration while maintaining a coherent, stable, and uninterrupted spatial profile throughout the maneuver, thereby confirming the structural integrity and robustness of the TSS under the time-varying mass and dynamic conditions.

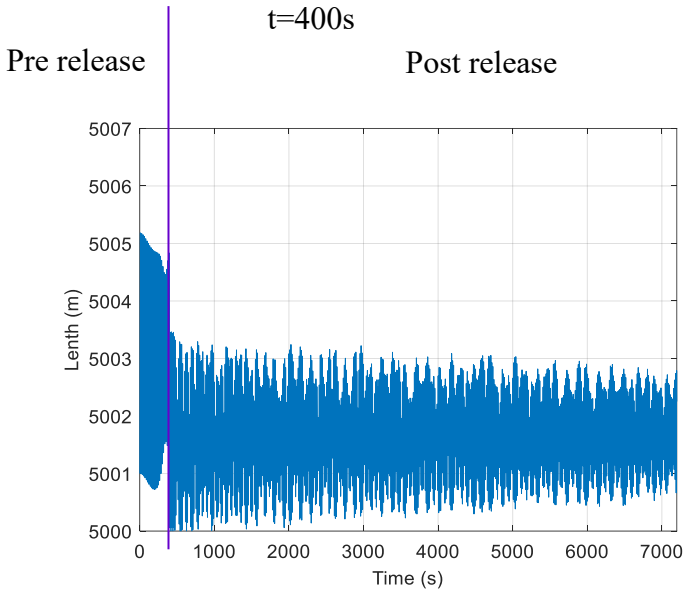

Figure 3-29 Time histories of the tether length.

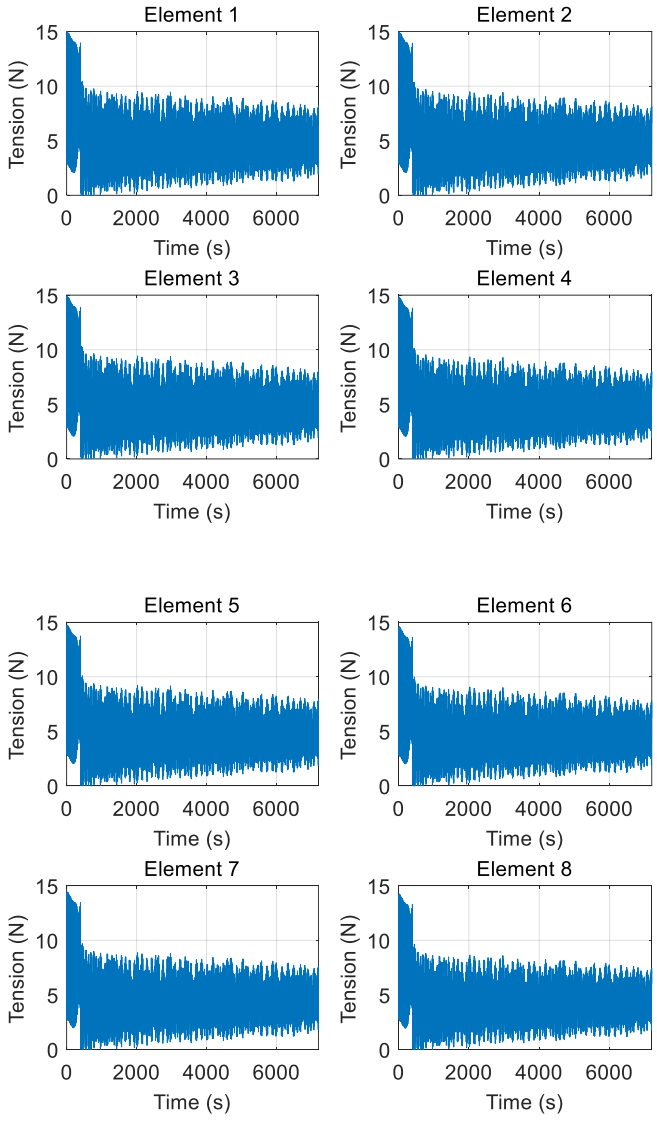

Figure 3-30 Tether tension of each tether element.

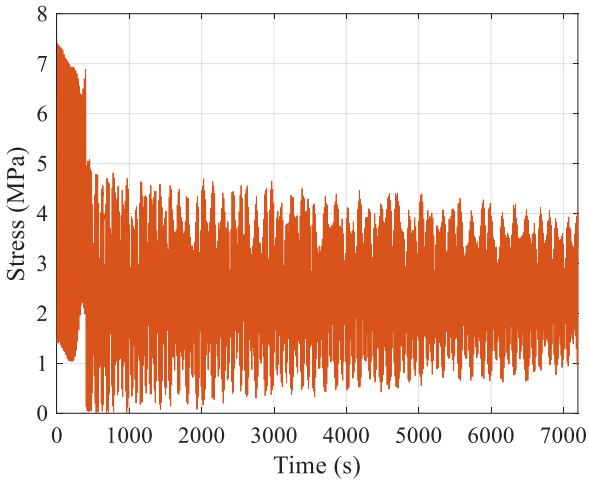

Figure 3-31 Time histories of the von Mises stress at the connection nodes between the tether and spacecraft.

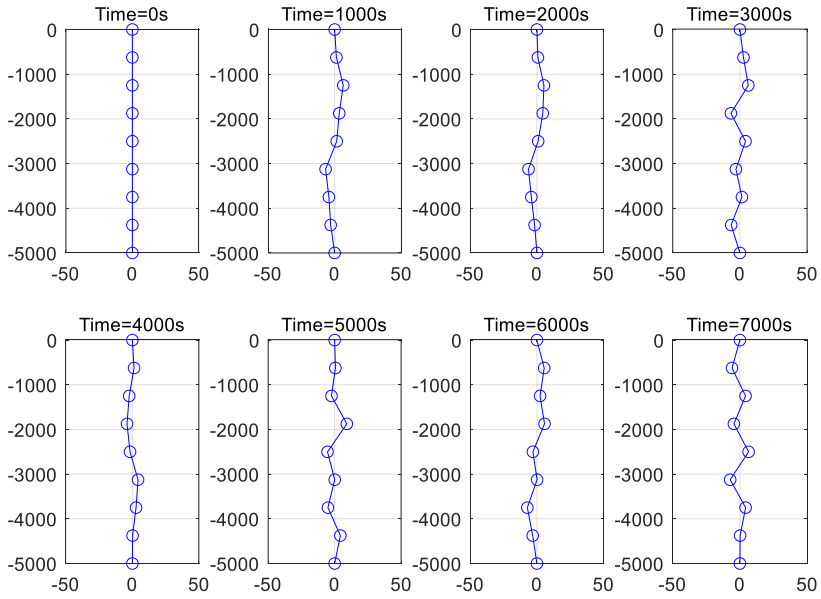

Figure 3-32 Tether configurations at different time instants after payload release.

Overall, these results demonstrate the proposed NPFEM-based elastic dynamic model

and the feasibility of using a momentum-exchange tethered spacecraft system for orbital energy transfer. The maintained tension and stable configuration after payload release highlight the system's potential for propellant-free payload transfer from low to higher orbits.

3.5.3 Dynamic Analysis of Hub-Spoke Tethered Spacecraft Formation

The final case is the hub-spoke tethered spacecraft formation (HS-TSF). This configuration shows considerable promise for advanced missions, including electric sail propulsion and synthetic aperture radar [108]. As illustrated in Figure 3-33, the formation consists of a central hub connected to multiple peripheral sub spacecraft via radial tethers. The tether deployment strategy leverages rotation of the central hub to generate centrifugal forces on the sub spacecraft, providing the tension required to deploy them while maintaining a taut tether configuration throughout the formation.

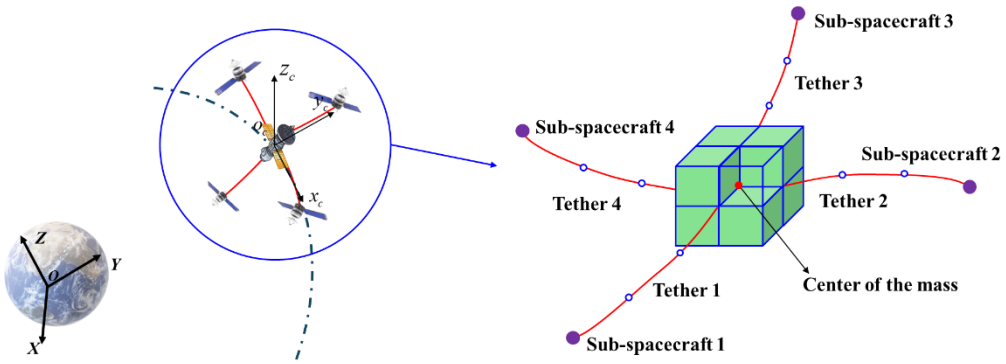

Figure 3-33 The schematic and the discretized model of HS-TSF.

In this model, the central hub was discretized into 8 solid elements, while each of the 4 tethers was modeled with 3 tether elements per tether, as depicted in Figure 3-33. Due to their significantly smaller mass and size relative to the central hub, the sub spacecraft were simplified as lumped point masses. The physical parameters of the HS-TSF are given in Table 3-11. The tether's properties are identical to those defined in Table 3-11.

Table 3-11 Physical parameters of the HS-TSF

Parameter	Value
Density of the main spacecraft	2700 kg/m^3
The size of the main spacecraft	$0.8\text{m}\times 0.8\text{m}\times 0.8\text{m}$
The mass of the sub spacecraft	21.6kg

The HS-TSF was initialized in the simulation in the equatorial plane, comprising a central hub connected to four sub spacecraft by 10m tethers initially. As shown in Figure 3-33, the initial formation is in a cross-configuration: Tethers 1 and 3 are aligned in the local vertical, while Tethers 2 and 4 are oriented in the along-track direction. It is assumed that the center of mass of the entire system operates in Earth orbit at an altitude of 600km initially. Similar to the definition in Section 3.5.1 and Section 3.5.2, a body-fixed reference frame $o_c x_c y_c z_c$ is defined with its origin at the center of mass of the central hub, which is initially located at $[0, 6978137, 0]^{\mathrm{T}}$ in the ECI *O-XYZ* frame. Euler angles are used to describe the attitude motion of the central hub relative to the ECI frame. The entire system is initially assumed to spin at a constant angular velocity $\omega = 0.38 rad/s$. After 30 s, the tethers are released at an initial speed of 0.05 m/s without any active control input, such that the sub spacecraft are passively deployed by the centrifugal force resulting from the

spin of the central hub. Again, the gravity and atmospheric models are the same as those used in Section 3.5.1. The simulations in this case were conducted using the same numerical solver as that described in Section 3.5.1, with a time step of 0.00001s.

The simulation results depicted in Figure 3-34-Figure 3-38 present the time histories of critical parameters during the uncontrolled tether deployment, including orbital motion, the rotational dynamics (spin angles and rates) of the central hub, the deployed length of each tether, and the tension in each tether element. As discussed in the first simulation case (Section 3.5.1), the center of mass of the central hub also exhibits noticeable altitude and out-of-plane oscillations. These oscillations are induced by gravitational perturbations inherent in the non-ideal gravity model, particularly gravity-gradient effects and Earth's oblateness, which prevent the orbit from remaining a perfectly closed circular trajectory in the equatorial plane. Figure 3-35-Figure 3-36 show a significant deceleration of the central hub's spin during tether deployment, consistent with conservation of angular momentum. As the sub spacecraft are deployed, the angular momentum arm increases, thereby the angular moment of inertia of the TSS. The resulting increase in the angular moment of inertia leads to a corresponding decrease in the spin rate of the central hub. Consistent with this trend, Figure 3-37-Figure 3-40 indicate that the tension in each tether element and the von Mises stress at each connection node between the tether and the spacecraft decrease as deployment proceeds, i.e., as tether length increases. This decrease in tension occurs because the decrease in spin rate ω^2, which overpowers the linear increase in tether length (L) in the centrifugal force $\omega^2 L$, dominates the linear increase in tether length, leading to a

net reduction in the centrifugal load and thus in tether tension, thereby reducing the internal stress of the spacecraft. Physically, this indicates that the TSS redistributes rotational energy during the tether deployment, which may help mitigate peak tether tensions and reduce the risk of structural failure. These results also highlight the need to account for both tether elasticity and rotational dynamics when predicting the mechanical response of TSS, and they provide useful guidance for designing deployment strategies that enable safe operation while minimizing tether stress.

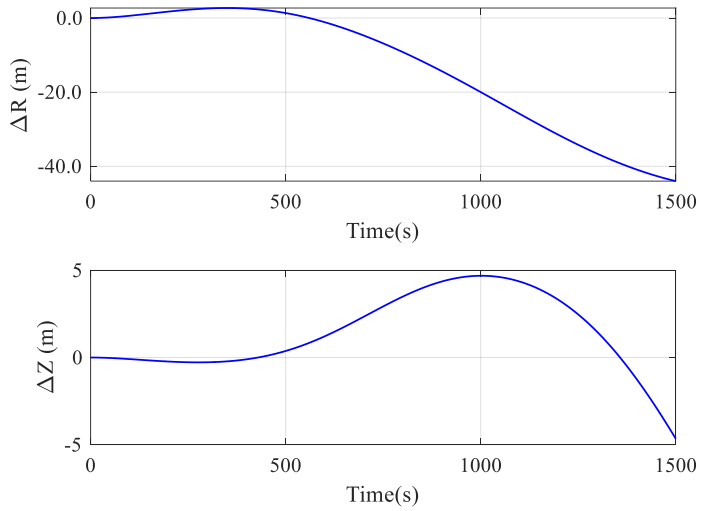

Figure 3-34 Time histories of the orbital altitude variation and out-of-plane motion of the center of mass on the central spacecraft.

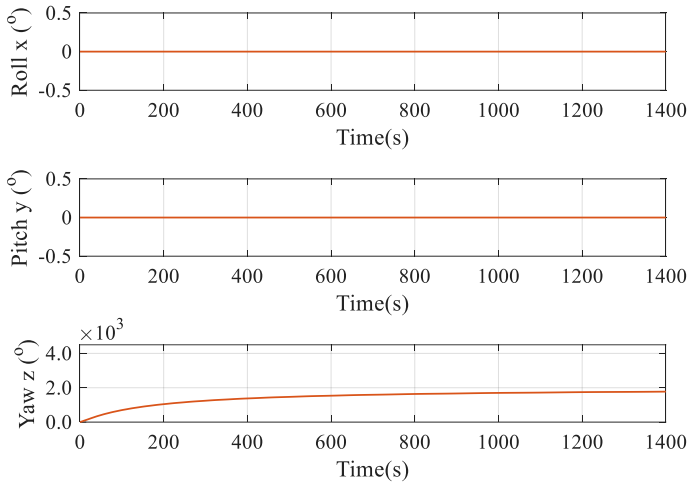

Figure 3-35 Time histories of the spin angles of the central hub.

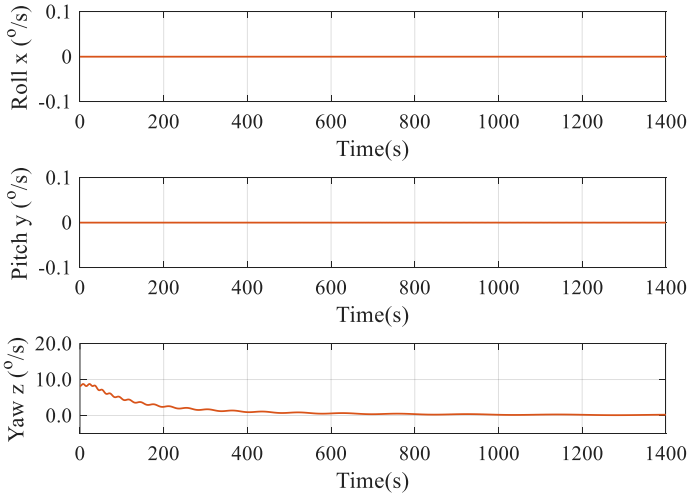

Figure 3-36 Time histories of the spin rates of the central hub.

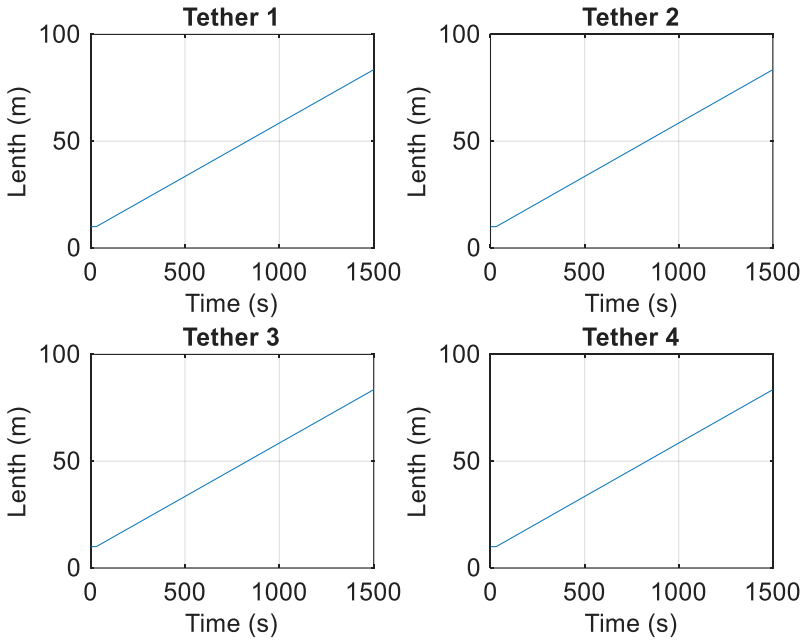

Figure 3-37 Time histories of the length of each tether.

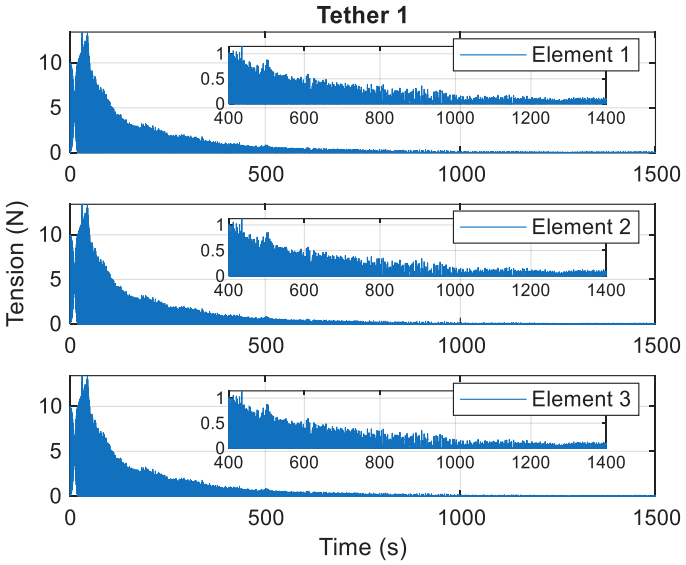
Tether 1
Element 1
Element 2
Element 3
Tension (N)
Time (s)

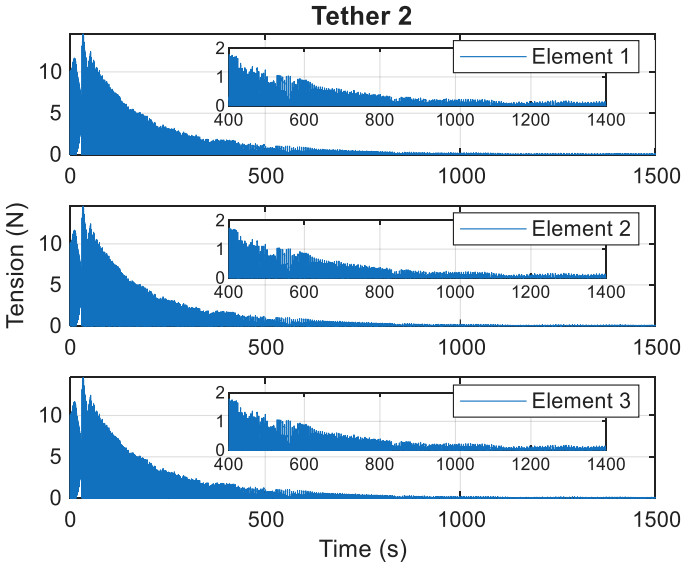
Tether 2
Element 1
Element 2
Element 3
Tension (N)
Time (s)

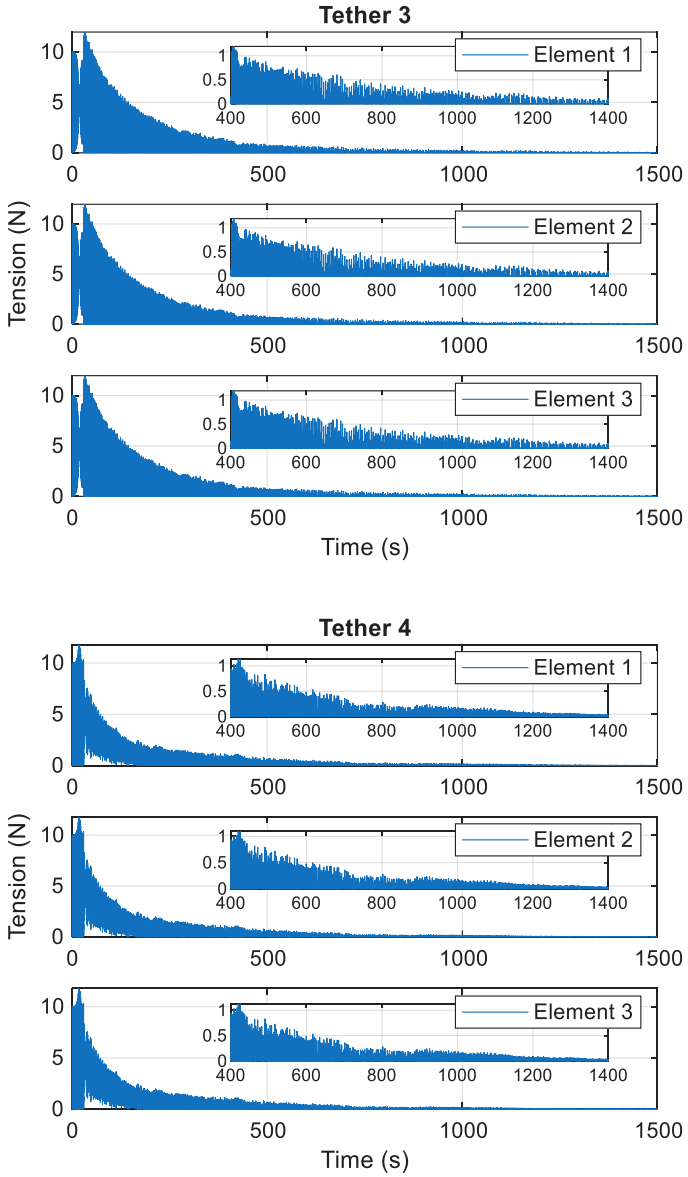

Figure 3-38 Tether tension of each tether element.

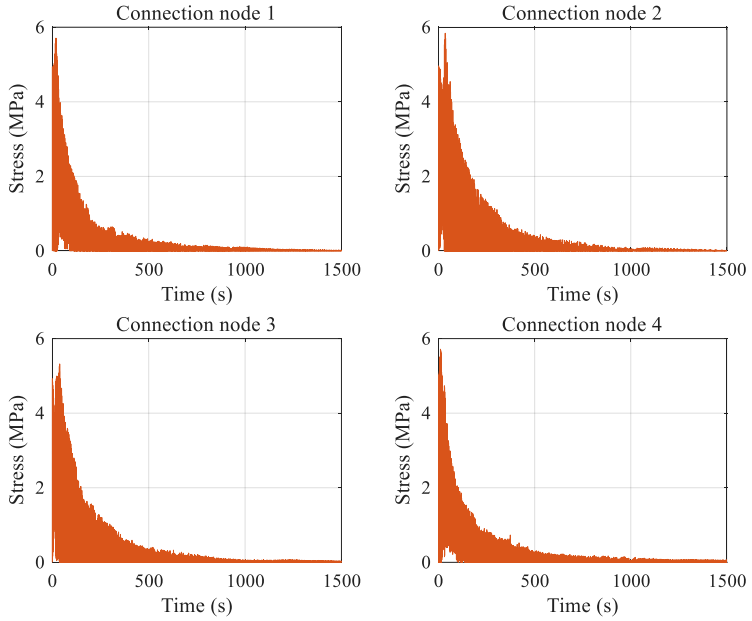

Figure 3-39 Time histories of the von Mises stress at the connection nodes between the tethers and the central hub.

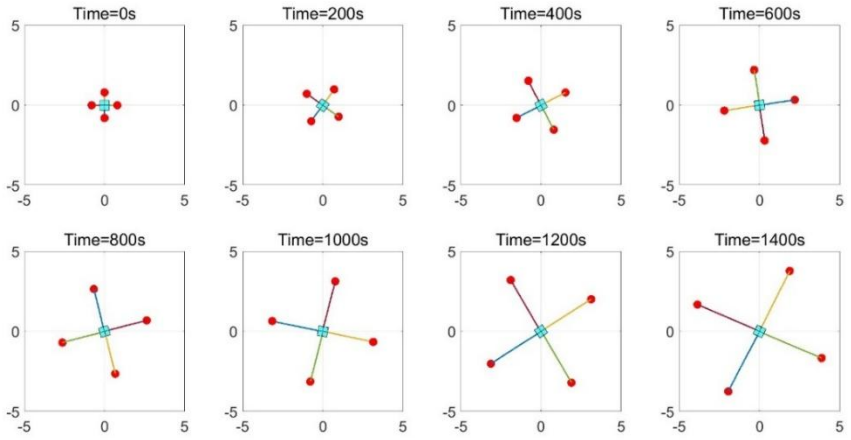

Figure 3-40 The configuration of HS-TSF at different time instants.

Chapter 4 FINITE ELEMENT KALMAN STATE ESTIMATOR OF SPACE TETHERS

Summary: This chapter develops a robust finite element Kalman filter for the state estimation of flexible tethered space systems, which are of significant importance in space exploration and satellite missions. The proposed method fuses position and velocity measurements at the tether ends, distributed fiber-optic strain measurements along the tether, and position and velocity estimates obtained from a finite element-based Kalman filter to estimate the state of the tether system. The related research has been published in **Reference (1)**, as listed in Section 1.6.

4.1. Preliminaries

While these discrete tether models are more accurate, they render existing control methodologies based on a single straight tether no longer applicable, because the tether discretization yields a set of libration angles for each element. Controlling a bent tether to its desired shape requires feedback on the full state of all elements or their libration angles, which is practically infeasible due to the extremely thin nature of the tether and the difficulty of placing sensors at individual elements along its length. Therefore, we proposed a novel and robust FE-Kalman state estimator to estimate the complete state of a flexible elastic tether using only measured state variables. It is assumed that both ends of the tether

are equipped with position and velocity sensors, and the flexible tether also features an embedded Fiber Optic Sensing System (FOSS). Furthermore, it is assumed, based on previous works [33,49,109], that (i) the system is in the orbit around the Earth; (ii) the spacecraft are modeled as lumped masses; (iii) the tether is made from an isotropic elastic material; and (iv) the optical fiber is considered massless with negligible stiffness.

The objective of the FE-Kalman state estimator is to estimate the three-dimensional motion of the tether. For the space tethers shown in Figure 4-1, the proposed FE-Kalman state estimator requires measurements of the positions and velocities of all nodes. As previously noted, it is assumed that the positions and velocities of the end nodes (Nodes #1 and #n) of the tether can be measured with high accuracy through GPS, INS, or other external means. Additionally, the longitudinal strain along the tether is assumed to be continuously and accurately measured by a fiber optic sensing system (FOSS). However, the positions and velocities of the internal nodes (Nodes #2, #3, ..., #n-1) are unobserved and must be estimated.

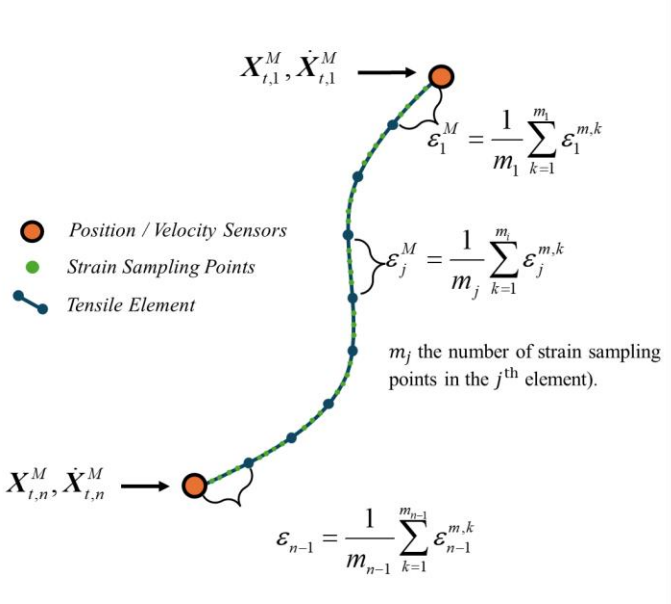

Figure 4-1 Schematic of the discretized FE model and states.

4.2. Dynamic Model of Space Tethers

Recalling Eq. (3.12), the dynamic equation of space tethers with control input can be formulated as

$$\boldsymbol{M}_t\ddot{\boldsymbol{X}}_t + \boldsymbol{K}_t\boldsymbol{X}_t + \boldsymbol{C}_t\dot{\boldsymbol{X}}_t - \boldsymbol{F}_t^0 - \boldsymbol{F}_t^e - \boldsymbol{B}_t^d\boldsymbol{u}_t = \boldsymbol{0} \tag{4.1}$$

where $\boldsymbol{B}_t^d$ is the control mapping matrix, and $\boldsymbol{u}_t$ is the control input.

Reformulating Eq. (3.12) into state space form yields,

$$\dot{\tilde{\boldsymbol{X}}} = \boldsymbol{A}_d\tilde{\boldsymbol{X}} + \boldsymbol{B}_d\boldsymbol{u}_d + \boldsymbol{F}^{ext} \tag{4.2}$$

$$\boldsymbol{A}_d = \begin{bmatrix} \boldsymbol{0} & \mathbf{I}_{3n\times 3n} \\ -\boldsymbol{M}_t^{-1}\boldsymbol{K}_t & -\boldsymbol{M}_t^{-1}\boldsymbol{C}_t \end{bmatrix},\ \boldsymbol{B}_d = \begin{bmatrix} \boldsymbol{0} \\ \boldsymbol{M}_t^{-1}\boldsymbol{B}_t^d \end{bmatrix},\ \boldsymbol{u}_d = \boldsymbol{u}_t \text{ and } \boldsymbol{F}^{ext} = \begin{bmatrix} \boldsymbol{0} \\ \boldsymbol{F}_t^d + \boldsymbol{F}_t^g \end{bmatrix} \tag{4.3}$$

where $\tilde{\boldsymbol{X}} = \left(\boldsymbol{X}_t, \dot{\boldsymbol{X}}_t\right)^{\mathrm{T}} \in \mathbb{R}^{6n\times 1}$ is the state vector, $\boldsymbol{A}_d \in \mathbb{R}^{6n\times 6n}$ is the state transition matrix, $\boldsymbol{B}_d \in \mathbb{R}^{6n\times 1}$ is the mapping matrix, $\boldsymbol{F}^{ext} \in \mathbb{R}^{6n\times 1}$ is the external force vector, and $\mathbf{I}_{3n\times 3n} \in \mathbb{R}^{3n\times 3n}$ is an identity matrix.

Theoretically, the discrete system model in the framework of a Kalman filter can be obtained by discretizing the dynamic model of the flexible tethers in Eq. (4.2) by the zero-order-hold method and adding measurement noise. However, previous studies have shown that a simple kinematic system model results in similar accuracy to a computationally intensive FE-based system model [49]. Therefore, in this work, the system model for the FE-Kalman state estimator is defined in discrete-time form as a first-order approximation of the time derivative of the state $\tilde{\boldsymbol{X}} \in \mathbb{R}^{6n\times 1}$, plus measurement noise, as follows,

$$\tilde{\boldsymbol{X}}_{i+1} = \tilde{\boldsymbol{A}}_i \tilde{\boldsymbol{X}}_i + \tilde{\boldsymbol{W}}_i \tag{4.4}$$

$$\tilde{\boldsymbol{A}}_i = \begin{bmatrix} \mathbf{I}_{3n\times 3n} & \Delta t \mathbf{I}_{3n\times 3n} \\ \mathbf{0} & \mathbf{I}_{3n\times 3n} \end{bmatrix} \in \mathbb{R}^{6n\times 6n} \tag{4.5}$$

where the subscript i represents the ith time step in Chapter 4, Δt is the time step, $\mathbf{I}_{3n\times 3n} \in \mathbb{R}^{3n\times 3n}$ is the identity matrix, and $\tilde{\boldsymbol{W}}_i \sim \left(0, \boldsymbol{Q}^{W}\right)$ is the white noise with a zero mean and a covariance matrix $\boldsymbol{Q}^{W}$.

4.3. Measurement Model

The proposed measurement model includes three integral components: (i) the sensor

model on the tether ends, (ii) the FOSS model, and (iii) the virtual sensor model. They are discussed as follows.

4.3.1 Position and Velocity Sensor Model

As shown in Figure 4-1, the position and velocity sensors onboard two tethered spacecraft are capable of precisely measuring the positions and velocities, denoted by $\boldsymbol{Y}_i^1 \in \mathbb{R}^{12}$, at the ends of the flexible tether at the ith time interval. The position and velocity sensor model can be formulated as follows:

$$\boldsymbol{Y}_i^1 = \boldsymbol{H}^1 \tilde{\boldsymbol{X}}_i + \tilde{\boldsymbol{V}}_i^1 \tag{4.6}$$

$$\boldsymbol{H}^1 = \begin{bmatrix} \mathbf{I}_{3\times3} & \mathbf{0}_{3\times3(n-2)} & \mathbf{0}_{3\times3} & \mathbf{0}_{3\times3} & \mathbf{0}_{3\times3(n-2)} & \mathbf{0}_{3\times3} \\ \mathbf{0}_{3\times3} & \mathbf{0}_{3\times3(n-2)} & \mathbf{I}_{3\times3} & \mathbf{0}_{3\times3} & \mathbf{0}_{3\times3(n-2)} & \mathbf{0}_{3\times3} \\ \mathbf{0}_{3\times3} & \mathbf{0}_{3\times3(n-2)} & \mathbf{0}_{3\times3} & \mathbf{I}_{3\times3} & \mathbf{0}_{3\times3(n-2)} & \mathbf{0}_{3\times3} \\ \mathbf{0}_{3\times3} & \mathbf{0}_{3\times3(n-2)} & \mathbf{0}_{3\times3} & \mathbf{0}_{3\times3} & \mathbf{0}_{3\times3(n-2)} & \mathbf{I}_{3\times3} \end{bmatrix} \tag{4.7}$$

where $\boldsymbol{Y}_i^1 = \left(\boldsymbol{X}_{t,1}^M, \dot{\boldsymbol{X}}_{t,1}^M, \boldsymbol{X}_{t,n}^M, \dot{\boldsymbol{X}}_{t,n}^M \right)^T \in \mathbb{R}^{12}$ represents the measured positions and velocities of tether ends at the ith time interval, $\boldsymbol{H}^1 \in \mathbb{R}^{12\times6n}$ is the observation matrix and equal to an identity matrix, and $\tilde{\boldsymbol{V}}_i^1 \in \mathbb{R}^{12}$ is the Gaussian white noise with a zero mean.

4.3.2 FOSS Model

The FOSS measures the longitudinal strain of the tether continuously, as shown in Figure 4-1. Denote the average strain in the jth element as $\varepsilon_{t,j}^M, j \in [1, n-1]$, such that

$$\varepsilon_{t,j}^{M} = \frac{1}{m_j}\sum_{k=1}^{m_i}\varepsilon_{t,j}^{m,k} \tag{4.8}$$

where m_j is the number of stain sampling points in the element. In this work, it is assumed $m_j = 10$.

Thus, the measurement model of the FOSS at the ith time interval is given as,

$$\boldsymbol{Y}_i^2 = \boldsymbol{f}_i^{\varepsilon}(\tilde{\boldsymbol{X}}_i) + \tilde{\boldsymbol{V}}_i^{\varepsilon} \tag{4.9}$$

where $\boldsymbol{Y}_i^2 = \left(\varepsilon_{t,1}^{M}, \varepsilon_{t,2}^{M}, \cdots, \varepsilon_{t,n-1}^{M}\right)^{\mathrm{T}} \in \mathbb{R}^{n-1}$ is the measured strain vector, $\boldsymbol{f}_i^{\varepsilon}(\tilde{\boldsymbol{X}}_i)$ is the observation function that maps the true state space into the observed space, and $\tilde{\boldsymbol{V}}_i^2 \in \mathbb{R}^{n-1}$ is the Gaussian white noise with a zero mean.

The observation function $\boldsymbol{f}_i^{\varepsilon}(\tilde{\boldsymbol{X}}_i)$ is unknown and is constructed by the newly developed inverse nodal position finite element method (iNPFEM). Recalling Eq. (3.3), the Green-Lagrange strain of the jth element is expressed as

$$\varepsilon_{t,j} = \boldsymbol{B}_{t,j}\boldsymbol{X}_{t,j}^{M} - 1 \tag{4.10}$$

where $\boldsymbol{X}_{t,j}^{M}$ is the same as $\boldsymbol{X}_{t,j}$ in Eq. (3.3).

Define the squared error between the measured and FE-estimated strain as per [110]

$$\Phi_j = \left(\varepsilon_{t,j} - \varepsilon_{t,j}^{M}\right)^2 \tag{4.11}$$

Substituting Eq. (4.10) into Eq. (4.11) yields

$$\Phi_j = (\boldsymbol{X}_{t,j}^{\mathrm{M}})^{\mathrm{T}}\boldsymbol{B}_{t,j}^{\mathrm{T}}\boldsymbol{B}_{t,j}\boldsymbol{X}_{t,j}^{M} - 2(1+\varepsilon_{t,j}^{M})(\boldsymbol{X}_{t,j}^{\mathrm{M}})^{\mathrm{T}}\boldsymbol{B}_{t,j}^{\mathrm{T}} + (\varepsilon_{t,j}^{M})^2 + 2\varepsilon_{t,j}^{M} + 1 \tag{4.12}$$

The sum of the squared strain error of the whole tether system can be formulated as

$$\Phi = \sum_{j=1}^{n-1} \Phi_j = \sum_{k=1}^{n} \left[(\boldsymbol{X}_{t,k}^{M})^{\mathrm{T}} \boldsymbol{B}_{t,k}^{\mathrm{T}} \boldsymbol{B}_{t,k} \boldsymbol{X}_{t,k}^{M} - 2(1+\varepsilon_{t,k}^{M})(\boldsymbol{X}_{t,k}^{M})^{\mathrm{T}} \boldsymbol{B}_{t,k}^{\mathrm{T}} + \left(\varepsilon_{t,k}^{M}\right)^2 + 2\varepsilon_{t,k}^{M} + 1 \right] \quad (4.13)$$

Minimizing the sum of squared strain error by $\partial\Phi \left/ \partial\left(\boldsymbol{X}_{t,j}^{M}\right)^{\mathrm{T}} = \boldsymbol{0}\right.$ yields,

$$\boldsymbol{K}_{t,j}^{inv} \boldsymbol{X}_{t,j}^{M\mathrm{T}} = \boldsymbol{\xi}_{t,j} \quad (4.14)$$

$$\boldsymbol{K}_{t,j}^{inv} = \boldsymbol{Q}_{t,j}^{\mathrm{T}} \left(\boldsymbol{B}_{t,j}^{0}\right)^{\mathrm{T}} \boldsymbol{B}_{t,j}^{0} \boldsymbol{Q}_{t,j} \quad (4.15)$$

$$\boldsymbol{Y}_{2,j} = \left(\boldsymbol{B}_{t,j}^{0}\right)^{\mathrm{T}} \boldsymbol{Q}_{t,j}^{\mathrm{T}} (\varepsilon_{t,j}^{M} + 1) \quad (4.16)$$

where $\boldsymbol{K}_{t,j}^{inv} \in \mathbb{R}^{6\times6}$ and $\boldsymbol{Y}_{2,j} \in \mathbb{R}^{6\times1}$ are defined as the element's inverse stiffness matrix and augmented strain vector, respectively.

The inverse finite element equation of the flexible tether is obtained by assembling all element equations based on the standard assembly procedure in FEM, such that

$$\boldsymbol{Y}^2 = \boldsymbol{K}_t^{inv} \boldsymbol{X}_t^{M} \quad (4.17)$$

where $\boldsymbol{K}_t^{inv} \in \mathbb{R}^{3(n-1)\times3n}$ is the observation matrix that maps the nodal displacement into the observed strain $\boldsymbol{\xi}_{t,j} \in \mathbb{R}^{3(n-1)\times1}$ in the total augmented measured strain vector.

Substituting the boundary conditions Eq. (4.6) into Eq. (4.17) yields,

$$\boldsymbol{Y}^2 = \boldsymbol{h}^2 \boldsymbol{X}_t^{M} \quad (4.18)$$

where $\boldsymbol{h}^2 \in \mathbb{R}^{3(n-2)\times3(n-2)}$ is the observation matrix that is invertible and $\boldsymbol{X}_t^{M} \in \mathbb{R}^{3(n-2)}$

represents the position vector of internal nodes.

Equation (4.18) can be further transformed into the state space expression by replacing the position vector $\boldsymbol{X}_t^M$ with the state vector $\tilde{\boldsymbol{X}}$, such that,

$$\boldsymbol{X}_t^M = \mathbf{T}^2 \tilde{\boldsymbol{X}} \quad \text{and} \quad \mathbf{T}^2 = \begin{bmatrix} \mathbf{0}_{3(n-2)\times 3} & \mathbf{I}_{3(n-2)\times 3(n-2)} & \mathbf{0}_{3(n-2)\times 3} & \mathbf{0}_{3(n-2)\times 3n} \end{bmatrix} \tag{4.19}$$

Substituting Eq. (4.18) into (4.9) yields the measurement model for FOSS at the ith time interval

$$\boldsymbol{Y}_i^2 = \boldsymbol{H}_i^2 \tilde{\boldsymbol{X}}_i + \tilde{\boldsymbol{V}}_i^2 \tag{4.20}$$

where $\boldsymbol{H}_i^2 = \boldsymbol{h}_i^2 \mathbf{T}^2 \in \mathbb{R}^{(n-1)\times 6n}$.

4.3.3 Virtual Sensor Model

Using the measurements obtained from the FOSS, the positions at each node along the tether can be determined via iNPFEM. However, the internal nodal velocities remain unmeasured and require estimation. To address this, a virtual sensor is introduced to estimate the internal nodal velocities using the dynamic FE model of the space tether, as described in Section 3.2, in a recursive manner.

Assume the measurement model of the virtual sensor can be expressed as

$$\boldsymbol{Y}_i^3 = \boldsymbol{f}_i^v \left(\tilde{\boldsymbol{X}}_i \right) + \tilde{\boldsymbol{V}}_i^3 \tag{4.21}$$

where $\boldsymbol{Y}_i^3 = \dot{\boldsymbol{X}}_i \in \mathbb{R}^{3(n-2)}$ is the velocity of internal nodes at the ith time to be estimated, $\boldsymbol{H}_i^3 \in \mathbb{R}^{3(n-2)\times 6n}$ is the nonlinear virtual observation function, and $\tilde{\boldsymbol{V}}_i^3 \in \mathbb{R}^{3(n-2)}$ is the

measurement noise of the virtual sensor due to model uncertainties and unmodeled dynamics.

Based on Refs. [49,72], the nonlinear virtual observation function is obtained by repeatedly solving the following constrained equation recursively using the Lagrange multiplier method,

$$\boldsymbol{h}_i^3\left(\dot{\boldsymbol{X}}_{t,i}\right)=\begin{cases}\boldsymbol{M}_{t,i}\ddot{\boldsymbol{X}}_{t,i}-\boldsymbol{C}_{t,i}\dot{\boldsymbol{X}}_{t,i}-\boldsymbol{K}_{t,i}\boldsymbol{X}_{t,i}+\boldsymbol{\phi}_{1\boldsymbol{X}}^{\mathrm{T}}\lambda_1+\boldsymbol{\phi}_{2\boldsymbol{X}}^{\mathrm{T}}\lambda_2=\boldsymbol{F}_{t,i}^{d}+\boldsymbol{F}_{t,i}^{g}+\boldsymbol{B}_t^{d}\boldsymbol{u}_i \\ \boldsymbol{\phi}_1\left(\tilde{\boldsymbol{X}}_{t,i}^{e},\boldsymbol{Y}_i^1\right)=\tilde{\boldsymbol{X}}_{t,i}^{e}-\boldsymbol{Y}_i^1=\boldsymbol{0} \\ \boldsymbol{\phi}_2\left(\boldsymbol{X}_{t,i}^{in},\boldsymbol{Y}_i^2\right)=\boldsymbol{X}_{t,i}^{in}-\boldsymbol{Y}_i^2=\boldsymbol{0}\end{cases} \tag{4.22}$$

$$\boldsymbol{\phi}_{1\boldsymbol{X}}^{\mathrm{T}}=\frac{\partial\boldsymbol{\phi}_1}{\partial\boldsymbol{X}},\ \text{and}\ \boldsymbol{\phi}_{2\boldsymbol{X}}^{\mathrm{T}}=\frac{\partial\boldsymbol{\phi}_2}{\partial\boldsymbol{X}} \tag{4.23}$$

where $\lambda_1\in\mathbb{R}^{12}$ and $\lambda_2\in\mathbb{R}^{3(n-2)}$ are the Lagrange multiplier vectors in Chapter 4.

Then, the measurement model of the virtual sensor can also be expressed as

$$\boldsymbol{Y}_i^3=\boldsymbol{h}_i^3\left(\dot{\boldsymbol{X}}_{t,i}\right)+\tilde{\boldsymbol{V}}_i^3=\bar{\boldsymbol{h}}_i^3\dot{\boldsymbol{X}}_{t,i}+\tilde{\boldsymbol{V}}_i^3 \tag{4.24}$$

where $\bar{\boldsymbol{h}}_i^3=\partial\boldsymbol{h}_i^3\big/\partial\dot{\boldsymbol{X}}_{t,i}$ is the virtual measurement Jacobian matrix. Since Eq. (4.22) has only one solution, $\bar{\boldsymbol{h}}_i^3$ is invertible.

Similar to the FOSS model, Eq. (4.24) can be rewritten in the state space format by replacing the velocity vector of internal nodes $\dot{\boldsymbol{X}}_t^{in}$ with the state vector $\tilde{\boldsymbol{X}}$, such that,

$$\dot{\boldsymbol{X}}_t^{in}=\mathbf{T}^3\tilde{\boldsymbol{X}}\quad\text{and}\quad\mathbf{T}^3=\begin{bmatrix}\mathbf{0}_{3(n-2)\times3n} & \mathbf{0}_{3(n-2)\times3} & \mathbf{I}_{3(n-2)\times3(n-2)} & \mathbf{0}_{3(n-2)\times3}\end{bmatrix} \tag{4.25}$$

Substituting Eq. (4.24) into (4.25) yields the measurement model at the ith time interval

$$\boldsymbol{Y}_i^3 = \boldsymbol{H}_i^3 \tilde{\boldsymbol{X}}_i + \tilde{\boldsymbol{V}}_i^3 \tag{4.26}$$

where $\boldsymbol{H}_i^3 = \bar{\boldsymbol{h}}_i^3 \mathbf{T}^3 \in \mathbb{R}^{(n-1)\times 6n}$.

4.3.4 Augmented Measurement Model of System

Finally, the measurement model is augmented by combining all three measurement models as

$$\boldsymbol{Y}_i = \boldsymbol{h}_i(\tilde{\boldsymbol{X}}_i) = \boldsymbol{H}_i \tilde{\boldsymbol{X}}_i + \tilde{\boldsymbol{V}}_i \tag{4.27}$$

$$\boldsymbol{Y}_i = \begin{bmatrix} \boldsymbol{Y}_i^1 \\ \boldsymbol{Y}_i^2 \\ \boldsymbol{Y}_i^3 \end{bmatrix}, \quad \boldsymbol{H}_i = \begin{bmatrix} \boldsymbol{H}_i^1 \\ \boldsymbol{H}_i^2 \\ \boldsymbol{H}_i^3 \end{bmatrix}, \quad \tilde{\boldsymbol{V}}_i = \begin{bmatrix} \tilde{\boldsymbol{V}}_i^1 \\ \tilde{\boldsymbol{V}}_i^2 \\ \tilde{\boldsymbol{V}}_i^3 \end{bmatrix} \tag{4.28}$$

where $\boldsymbol{H}_i \in \mathbb{R}^{6n\times 6n}$ is the total observation matrix, $\tilde{\boldsymbol{V}}_i \sim \left(0, \boldsymbol{R}^V\right)$ is the zero-mean white noise with a covariance $\boldsymbol{R}^V$.

The discrete system model Eq. (4.4) and measurement model Eq. (4.28) are reconstructed as

$$\begin{cases} \tilde{\boldsymbol{X}}_{i+1} = \tilde{\boldsymbol{A}}_i \tilde{\boldsymbol{X}}_i \\ \boldsymbol{Y}_i = \boldsymbol{H}_i \tilde{\boldsymbol{X}}_i \end{cases} \tag{4.29}$$

4.4. Implementation of State Estimator Algorithm

The FE-Kalman state estimator recursively runs in two major steps following a standard Kalman filter procedure,

Prediction:

Prediction model: $\hat{\tilde{\boldsymbol{X}}}_i = \tilde{\boldsymbol{A}}_{i-1}\hat{\tilde{\boldsymbol{X}}}_{i-1}$

Prediction covariance matrix: $\boldsymbol{P}_i^- = \tilde{\boldsymbol{A}}_{i-1}\boldsymbol{P}_{i-1}\tilde{\boldsymbol{A}}_{i-1}^{\mathrm{T}} + \boldsymbol{R}_{i-1}^{W}$

Correction:

Kalman gain: $\boldsymbol{G}_i^e = \boldsymbol{P}_i^- \boldsymbol{H}_i^{\mathrm{T}} (\boldsymbol{H}_i^{\mathrm{T}} \boldsymbol{P}_i^- \boldsymbol{H}_i^{\mathrm{T}} + \boldsymbol{R}^V)^{-1}$

Correct the state: $\hat{\tilde{\boldsymbol{X}}}_i = \hat{\tilde{\boldsymbol{X}}}_i^- + \boldsymbol{G}_i^e \left[\boldsymbol{Y}_i - \boldsymbol{H}_i \hat{\tilde{\boldsymbol{X}}}_i \right]$

Update the prediction covariance matrix: $\boldsymbol{P}_i = \left(\mathbf{I}_{3n\times 3n} - \boldsymbol{G}_i^e \boldsymbol{H}_i \right) \boldsymbol{P}_i^-$

where $\hat{\tilde{\boldsymbol{X}}}_i^-$ and $\hat{\tilde{\boldsymbol{X}}}_i$ are the prior and posterior estimations of $\tilde{\boldsymbol{X}}_i$ at the ith time.

The above iteration process of the state estimation algorithm is shown in Figure 4-2.

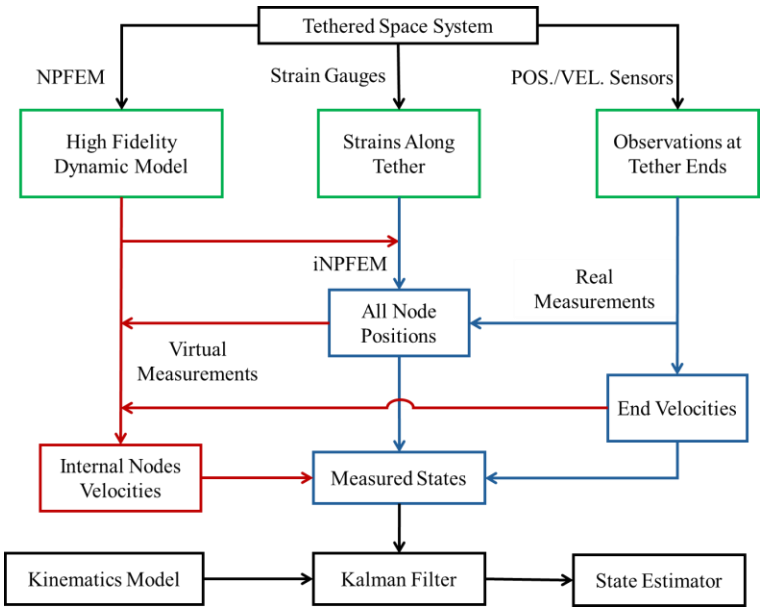

Figure 4-2 Flowchart of the state estimation algorithm.

4.5. Stability, Observability and Robustness of FE-Kalman State

Estimator

4.5.1 Stability and Observability

The state estimation algorithm is designed based on the Kalman filter. Hence, the stability of the FE-Kalman state estimator can be strictly proved using Lyapunov's second method as per Ref. [111].

To prove the observability of the flexible tether, the dynamic model, as represented by Eq. (4.2), and the measurement model are reformulated as,

$$\begin{cases} \dot{\tilde{\boldsymbol{X}}} = \boldsymbol{f}_d\left(\tilde{\boldsymbol{X}}, \boldsymbol{u}_d\right) \\ \boldsymbol{Y} = \boldsymbol{h}\left(\tilde{\boldsymbol{X}}\right) \end{cases} \tag{4.30}$$

where $\boldsymbol{f}_d\left(\tilde{\boldsymbol{X}}, \boldsymbol{u}_d\right) = \tilde{\boldsymbol{A}}_d\tilde{\boldsymbol{X}} + \tilde{\boldsymbol{B}}_d\boldsymbol{u}_d + \boldsymbol{F}^{ext}$, and $\boldsymbol{h}\left(\tilde{\mathbf{X}}\right) = \boldsymbol{H}\tilde{\boldsymbol{X}} + \tilde{\boldsymbol{V}}$ is the continuous expression of Eq. (4.27).

As the system is nonlinear, its observability shall be proved by Lie derivatives [112].

***Remark* 1** The Lie derivative of the function $\boldsymbol{h}$ with respect to the function $\boldsymbol{f}_d$ is defined as

$$\begin{cases} \mathcal{L}_{f_d}^0\boldsymbol{h}\left(\tilde{\boldsymbol{X}}\right) = \boldsymbol{h}\left(\tilde{\boldsymbol{X}}\right) \\ \mathcal{L}_{f_d}^1\boldsymbol{h}\left(\tilde{\boldsymbol{X}}\right) = \dfrac{\partial\mathcal{L}_{f_d}^0\boldsymbol{h}\left(\tilde{\boldsymbol{X}}\right)}{\partial\tilde{\boldsymbol{X}}}\boldsymbol{f}_d \\ \vdots \\ \mathcal{L}_{f_d}^k\boldsymbol{h}\left(\tilde{\boldsymbol{X}}\right) = \dfrac{\partial\mathcal{L}_{f_d}^{k-1}\boldsymbol{h}\left(\tilde{\boldsymbol{X}}\right)}{\partial\tilde{\boldsymbol{X}}}\boldsymbol{f}_d \end{cases}, \left(k = 0,1,2,\cdots\right) \tag{4.31}$$

where k is the order of Lie derivatives.

***Remark* 2** The nonlinear system's observability matrix is denoted as $\mathcal{O} \in \mathbb{R}^{6n\times 6n}$.

$$\mathcal{O} = \begin{bmatrix} \nabla \mathcal{L}_{f_d}^{0} \boldsymbol{h}\left(\tilde{\boldsymbol{X}}\right) \\ \nabla \mathcal{L}_{f_d}^{1} \boldsymbol{h}\left(\tilde{\boldsymbol{X}}\right) \\ \vdots \\ \nabla \mathcal{L}_{f_d}^{6n-1} \boldsymbol{h}\left(\tilde{\boldsymbol{X}}\right) \end{bmatrix} \tag{4.32}$$

***Remark* 3** If the column rank of the observability matrix is full, the nonlinear system is observable.

According to the first two remarks, the observability matrix of the flexible tether can be written as

$$\mathcal{O} = \begin{bmatrix} \nabla \mathcal{L}_{f_d}^{0} \boldsymbol{h}\left(\tilde{\mathbf{X}}\right) \\ \nabla \mathcal{L}_{f_d}^{1} \boldsymbol{h}\left(\tilde{\mathbf{X}}\right) \\ \vdots \\ \nabla \mathcal{L}_{f_d}^{6n-1} \boldsymbol{h}\left(\tilde{\mathbf{X}}\right) \end{bmatrix} == \begin{bmatrix} H \\ \boldsymbol{H}\left(\dfrac{\partial \boldsymbol{f}_d}{\partial \tilde{\boldsymbol{X}}}\right) \\ \vdots \\ \boldsymbol{H}\left(\dfrac{\partial_{6n-1}}{\partial \tilde{\boldsymbol{X}}}\left(\cdots \dfrac{\partial_3}{\partial \tilde{\boldsymbol{X}}}\left(\dfrac{\partial_2}{\partial \tilde{\boldsymbol{X}}}\left(\left(\dfrac{\partial_1}{\partial \tilde{\boldsymbol{X}}} \boldsymbol{f}_d\right)\boldsymbol{f}_d\right)\boldsymbol{f}_d\right)\boldsymbol{f}_d\right)\right) \end{bmatrix} \tag{4.33}$$

The matrix $\boldsymbol{H}$ can be explicitly expressed as

$$\boldsymbol{H} = \begin{bmatrix} \mathbf{I}_{3\times 3} & \mathbf{0}_{3\times 3(n-2)} & \mathbf{0}_{3\times 3} & \mathbf{0}_{3\times 3} & \mathbf{0}_{3\times 3(n-2)} & \mathbf{0}_{3\times 3} \\ \mathbf{0}_{3\times 3} & \mathbf{0}_{3\times 3(n-2)} & \mathbf{I}_{3\times 3} & \mathbf{0}_{3\times 3} & \mathbf{0}_{3\times 3(n-2)} & \mathbf{0}_{3\times 3} \\ \mathbf{0}_{3\times 3} & \mathbf{0}_{3\times 3(n-2)} & \mathbf{0}_{3\times 3} & \mathbf{I}_{3\times 3} & \mathbf{0}_{3\times 3(n-2)} & \mathbf{0}_{3\times 3} \\ \mathbf{0}_{3\times 3} & \mathbf{0}_{3\times 3(n-2)} & \mathbf{0}_{3\times 3} & \mathbf{0}_{3\times 3} & \mathbf{0}_{3\times 3(n-2)} & \mathbf{I}_{3\times 3} \\ \mathbf{0}_{3(n-2)\times 3} & \boldsymbol{h}^2 & \mathbf{0}_{3(n-2)\times 3} & \mathbf{0}_{3(n-2)\times 3} & \mathbf{0}_{3\times 3(n-2)} & \mathbf{0}_{3\times 3} \\ \mathbf{0}_{3(n-2)\times 3} & \mathbf{0}_{3\times 3(n-2)} & \mathbf{0}_{3\times 3} & \mathbf{0}_{3\times 3} & \overline{\boldsymbol{h}}^3 & \mathbf{0}_{3\times 3} \end{bmatrix} \tag{4.34}$$

where $\boldsymbol{h}^2$ and $\boldsymbol{h}^3$ are invertible as explained in the previous sections, and $\mathbf{I}_{3n\times 3n}$ is an

identity matrix.

Therefore, the matrix $\boldsymbol{H}$ must possess a full column rank of 6n, ensuring that the observability matrix $\mathcal{O}$ always retains its full column rank of 6n, regardless of the value of any other parameters. According to ***Remark* 3**, the system can be proved to be observable.

4.5.2 Robustness

The real measurement can be updated at each time step, and the errors in the real measurement are solely a result of the sensors and must be bounded. Therefore, if the errors in the virtual measurement are proven to be bounded, the robustness of the overall measurement model can be ensured.

The discrete form of the system model in Eq. (4.2) is derived using the zero-order-hold method. Linearizing the model, we have

$$\bar{\boldsymbol{X}}_{i+1} = \bar{\boldsymbol{A}}_i^d \bar{\boldsymbol{X}}_i + \bar{\boldsymbol{B}}_i^d \boldsymbol{u}_i \tag{4.35}$$

$$\bar{\boldsymbol{A}}^d = \mathbf{I}_{3n\times 3n} + \bar{\boldsymbol{A}}\Delta t = \begin{bmatrix} \mathbf{I}_{3n\times 3n} & \mathbf{I}_{3n\times 3n}\Delta t \\ -\boldsymbol{M}_{t,i}^{-1}\boldsymbol{K}_{t,i}\Delta t & -\boldsymbol{M}_{t,i}^{-1}\boldsymbol{C}_{t,i}\Delta t + \mathbf{I}_{3n\times 3n} \end{bmatrix}, \text{ and } \bar{\boldsymbol{B}}_i^d = \boldsymbol{0} \tag{4.36}$$

Since the positions of all nodes can be obtained by real measurements from the FOSS at each time step, the errors of positions can be updated in each iteration loop. Then, assuming the errors in the velocities at the ith and i+1th time are denoted as $\boldsymbol{\Delta}_v^i$ and $\boldsymbol{\Delta}_v^{i+1}$ respectively, substituting them into Eq. (4.35) yields

$$\left|\boldsymbol{\Delta}_v^{i+1}\right| \le \boldsymbol{M}_{t,i}^{-1}\boldsymbol{C}_{t,i}\Delta t\boldsymbol{\Delta}_v^i + \mathbf{I}_{3n\times 3n}\left|\boldsymbol{\Delta}_v^i\right| \tag{4.37}$$

where $\boldsymbol{M}_{t,i}^{-1}\boldsymbol{C}_{t,i}\Delta t\boldsymbol{\Delta}_v^i$ is much smaller than $\mathbf{I}_{3n\times 3n}\boldsymbol{\Delta}_v^i$. Hence it is proved that the errors in the virtual measurement are bounded, and the newly proposed FE-Kalman state estimator is robust.

4.6. Simulation and Discussion

To demonstrate the effectiveness of the newly proposed state estimation algorithm, numerical simulations of a space tether are carried out. The space tether is assumed to orbit the Earth with an initial orbital altitude of 600km in the equatorial orbit, which is in the *X*-*Y* plane as shown in Figure 4-3. The two spacecraft at the ends are modeled as two 5kg lumped masses. Based on NPFEM, the flexible tether is discretized into eight elements with nine nodes. The physical properties of the flexible tether are listed in Table 4-1. The states of the two spacecraft at each end of the tether and the strains along the tether are directly measured and used as feedback for the state estimator. The state of the tether is then estimated by the proposed algorithm. A high-fidelity nodal position finite element model is used to imitate the dynamics of the real space tethers in space, serving as a reference for comparison.

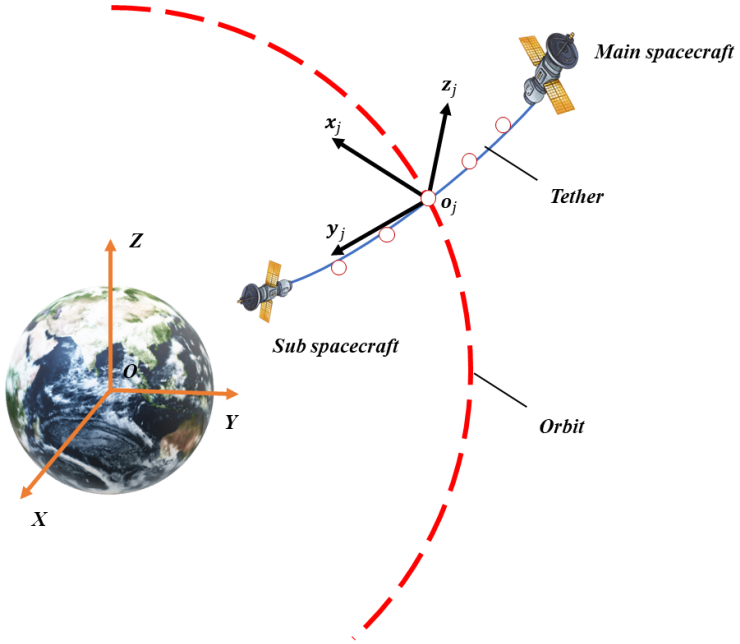

Figure 4-3 The schematic diagram of TSS model.

Table 4-1 Physical properties of the flexible tether [49]

Parameter	Value
Length of tether (m)	500
Density (kg/m3)	2700
Cross-sectional Area (m2)	$1.978\text{x}10^{-7}$
Young's Modulus (GPa)	72

In the simulation, the covariance matrix $\boldsymbol{Q}^{W}$ of the process noise $\tilde{\boldsymbol{W}}_j$ and the covariance matrix $\boldsymbol{R}^{V}$ of the measurement noise $\boldsymbol{V}_h$ are defined to be the same, with a standard deviation is 0.01(m or m/s). The damping coefficients (α_t and β_t) are set to 0 and 0.0015 as per Ref. [49], respectively. The simulation period is 5 hours. The gravitational and atmospheric drag forces are calculated using the Earth Gravity Model (2008) [100] and the Atmosphere Density Model (NRLMSIS-00) [101]. Finally, for direct comparison purposes, the same case in Ref. [49] was analyzed by the proposed state

estimator. The results of the simulation are presented and discussed in the following.

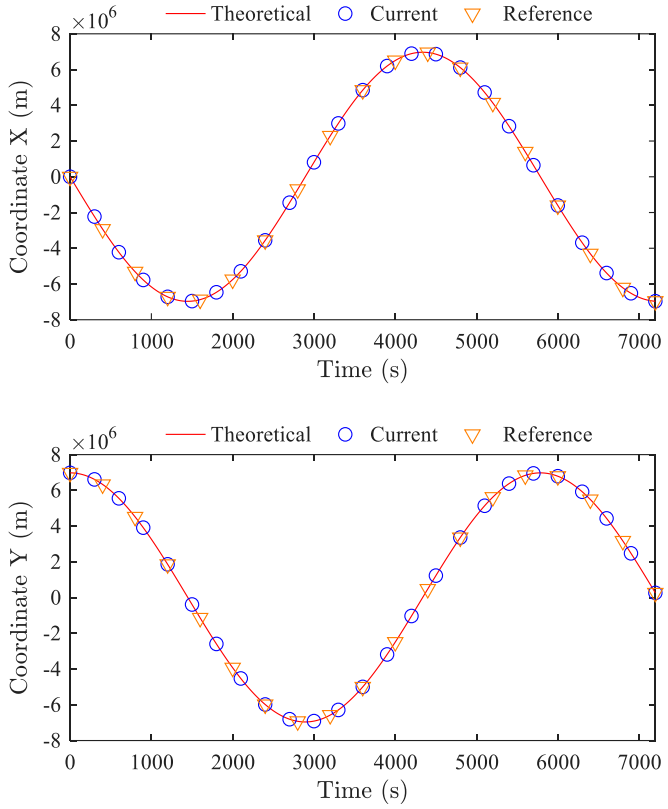

Figure 4-4 Comparison of position estimation at the 3rd node: (a) *X*-Axis (b) *Y*-Axis.

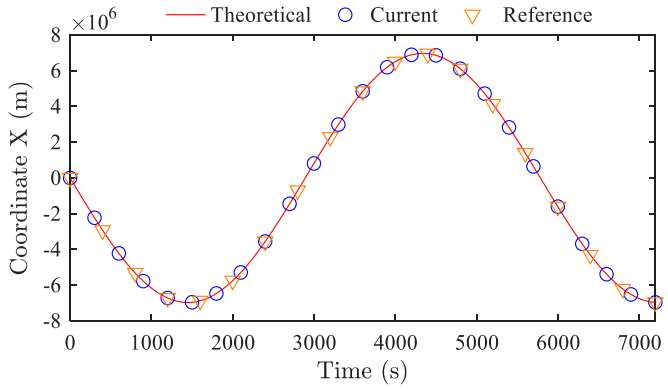

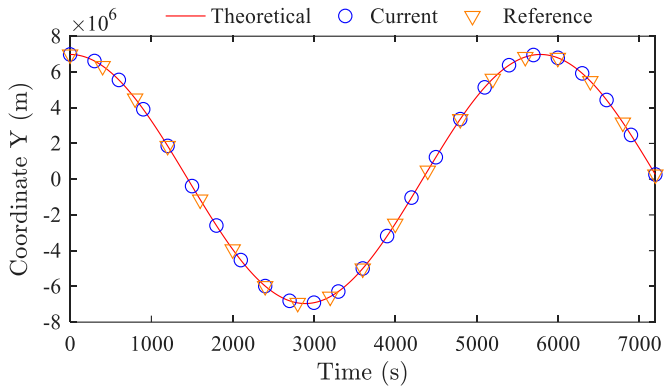

Figure 4-5 Comparison of position estimation at the 5th node: (a) *X*-Axis (b) *Y*-Axis.

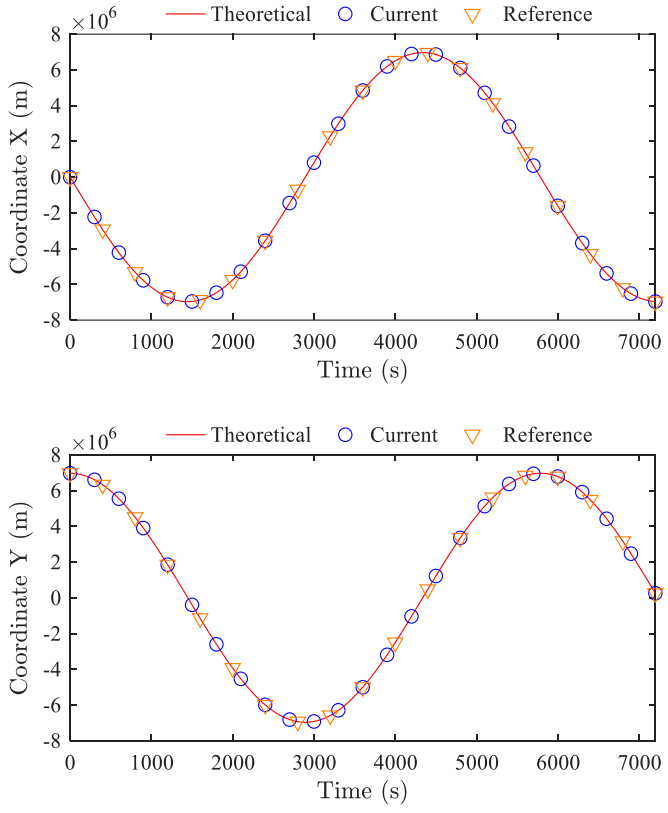

Figure 4-6 Comparison of position estimation at the 7th node: (a) *X*-Axis (b) *Y*-Axis.

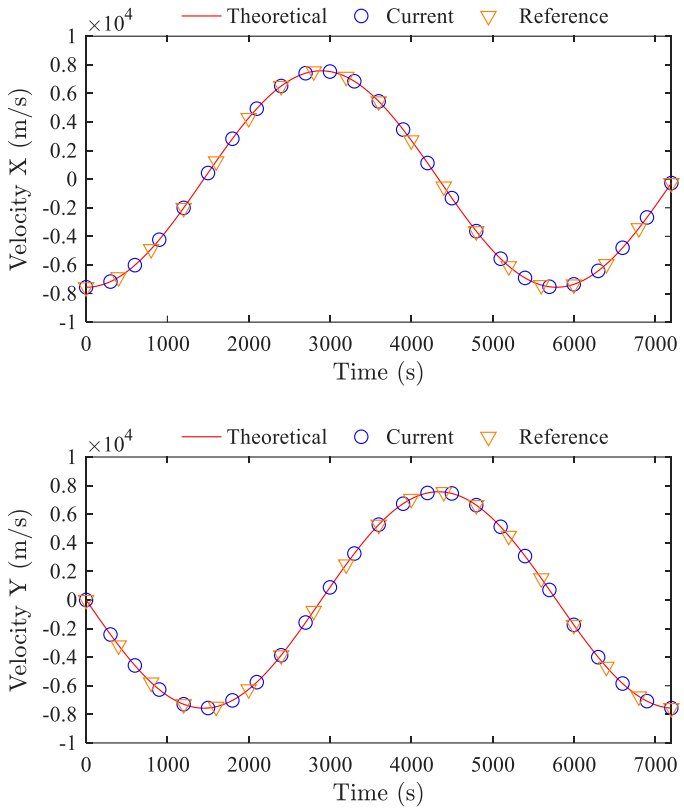

Figure 4-7 Comparison of velocity estimation at the 3rd node: (a) *X*-Axis (b) *Y*-Axis.

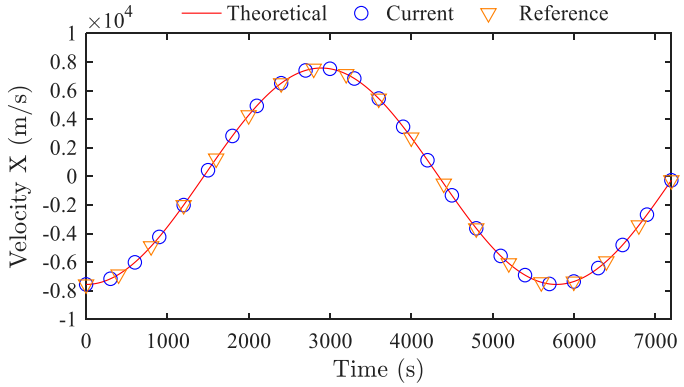

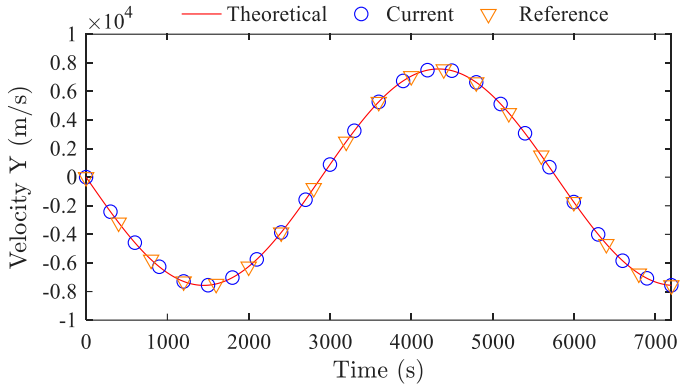

Figure 4-8 Comparison of velocity estimation at the 5th node: (a) *X*-Axis (b) *Y*-Axis.

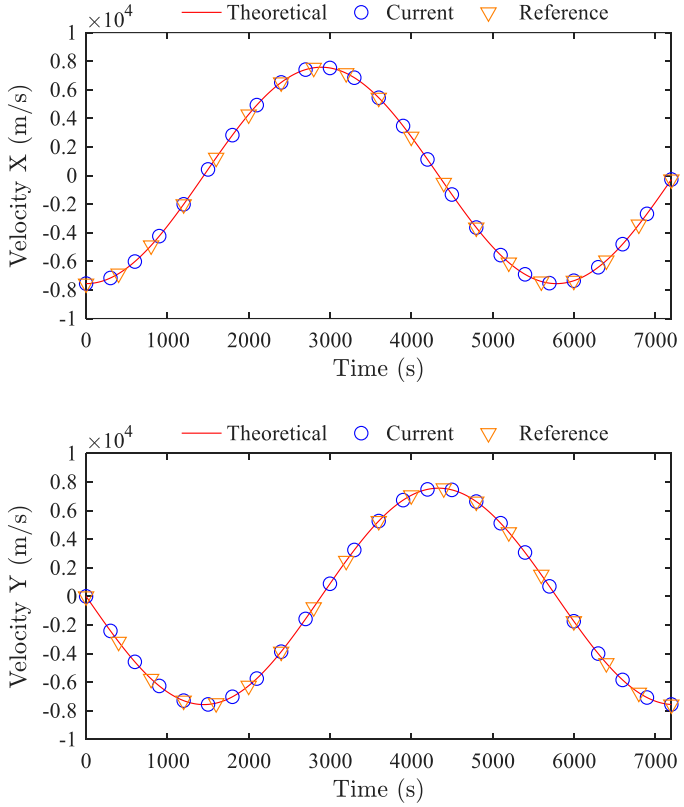

Figure 4-9 Comparison of velocity estimation at the 7th node: (a) *X*-Axis (b) *Y*-Axis.

Since the space tether orbits in the equatorial orbit or the *X*-*Y* plane, Figure 4-4-Figure 4-9 only present the positions and velocities in the *X* and *Y* axes at the 3rd, 5th, and 7th

internal nodes. It is evident that the estimations by the current and reference methods are highly consistent with the real state. To evaluate the performance, we examine the position estimation errors along the tether over time and plot them in Figure 4-10. It is observed that the maximum errors in state estimation always occur in the middle section of the tether in both methods. The magnitude of the maximum errors is reduced by a factor of 3 plus using the current method compared to the reference method [49].

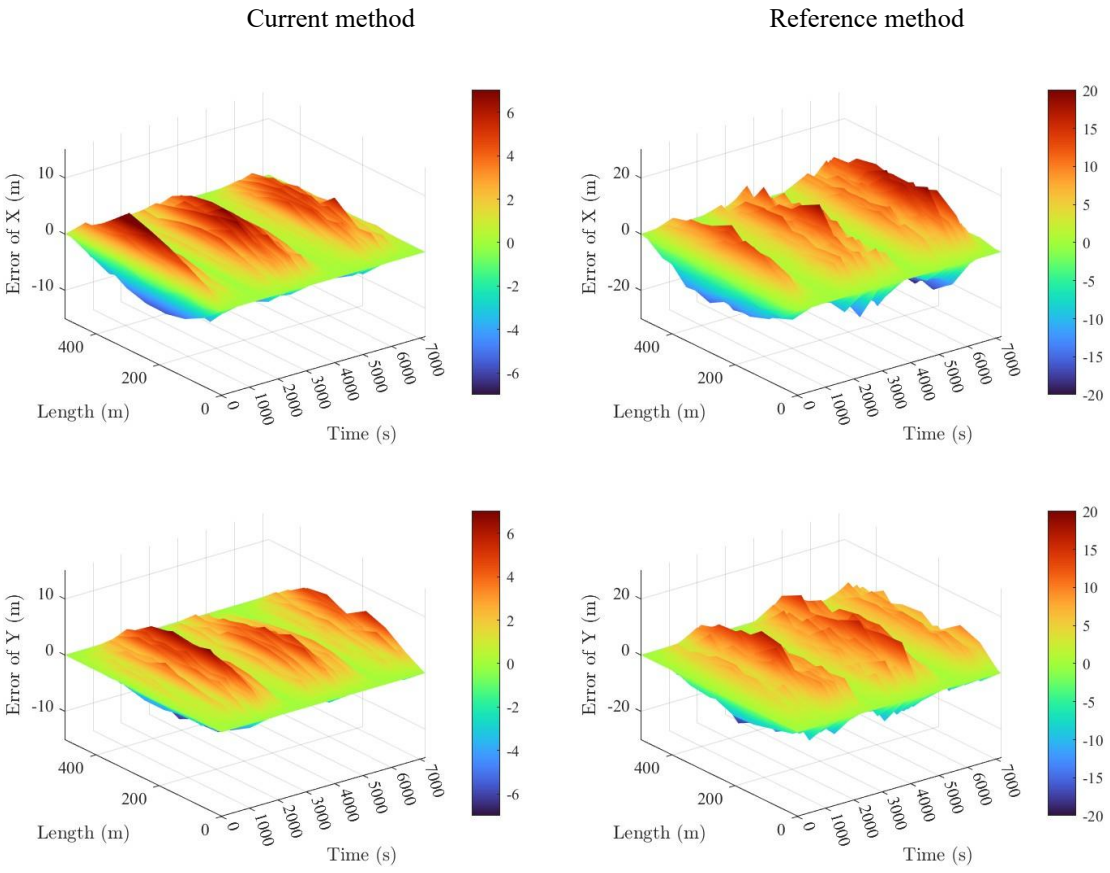

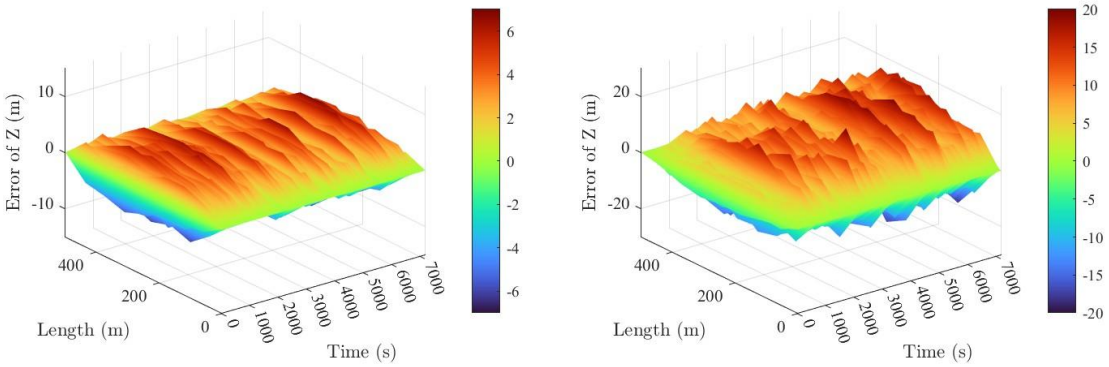

Figure 4-10 Errors of the current and reference method in different directions.

To further investigate the effectiveness of the current method, the position and velocity estimation errors at the 3rd, 5th, and 7th nodes are illustrated in Figure 4-11-Figure 4-16. The results demonstrate that, compared to the previous approach in [49], the proposed state estimation algorithm can achieve better estimation performance by reducing estimation errors. The strain observations from the FOSS provide nontrivial information, which keeps the estimation errors bounded. The errors vary periodically, with a maximum of about 8m per cycle. In contrast, these cyclic maximum estimation errors in [49] may increase over time. Therefore, the newly proposed state estimation algorithm is capable not only of enhancing estimation accuracy but also of achieving long-term stable estimation.

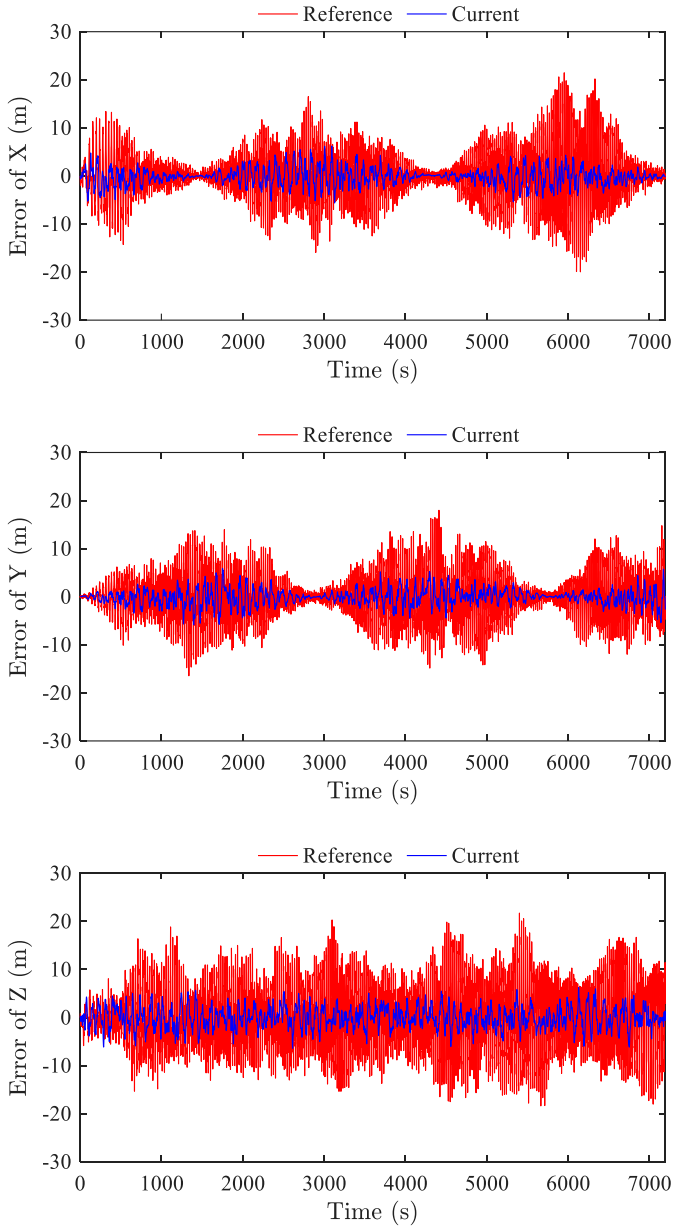

Figure 4-11 Comparison of position estimation errors of the 3rd node by the previous method and the proposed method in different directions.

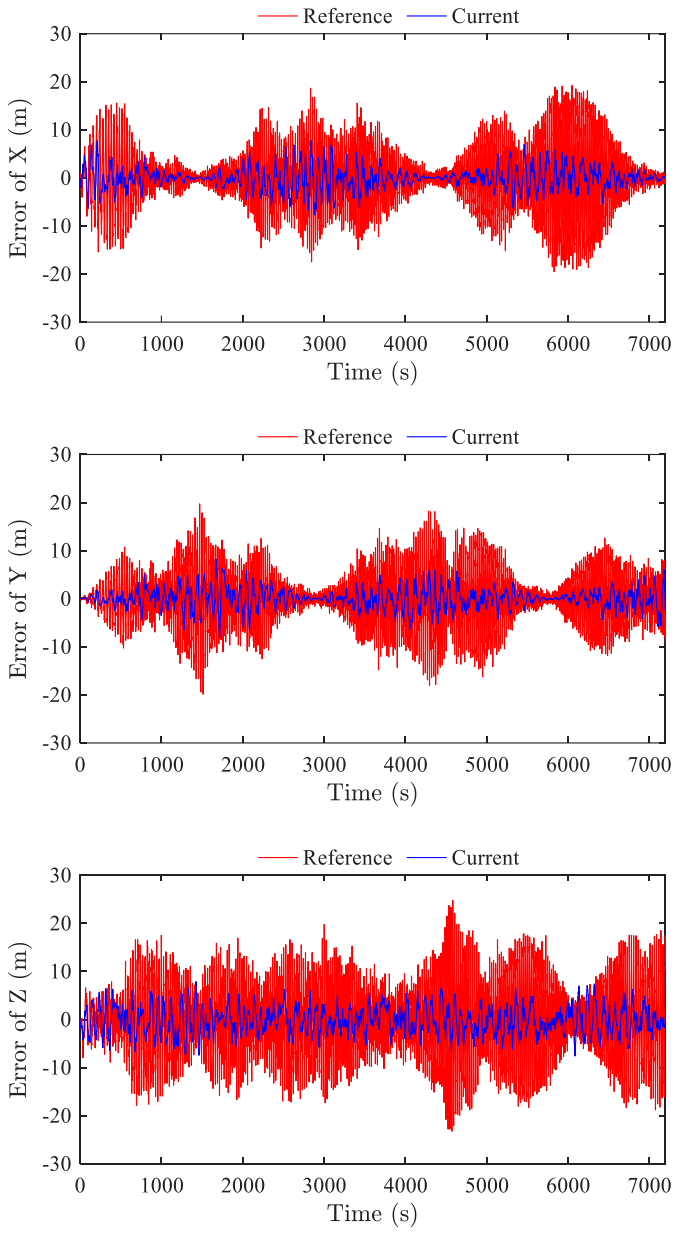

Figure 4-12 Comparison of position estimation errors of the 5th node by the previous method and the proposed method in different directions.

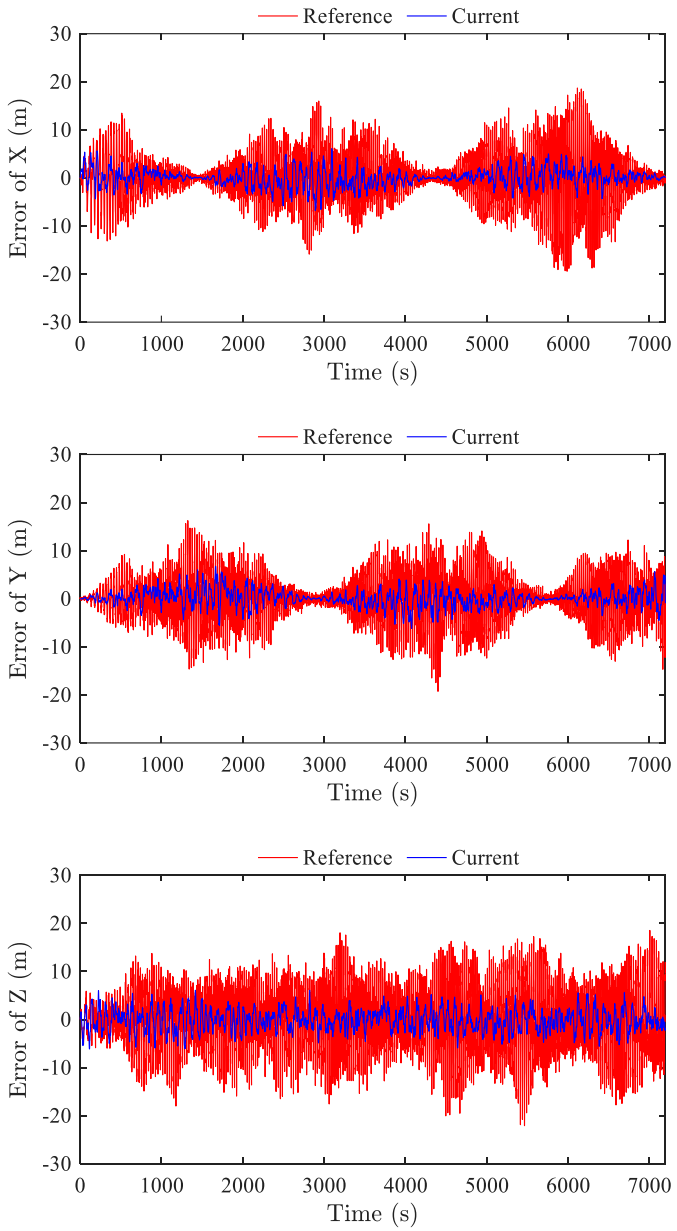

Figure 4-13 Comparison of position estimation errors of the 7th node by the previous method and the proposed method in different directions.

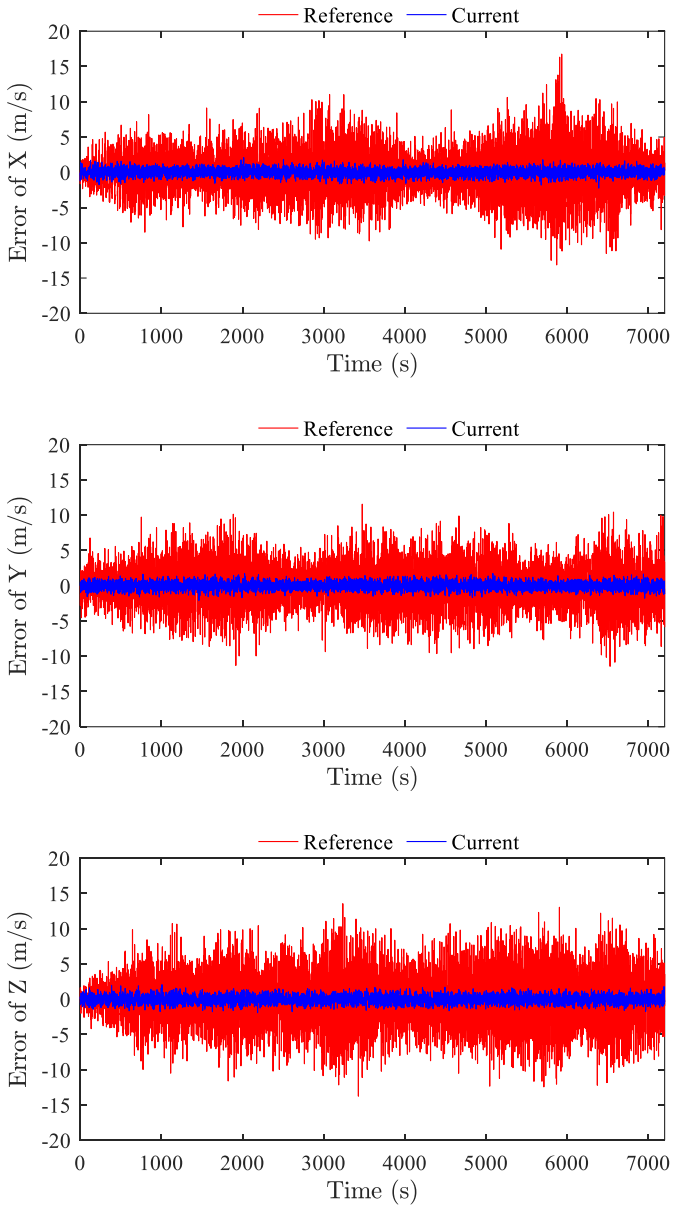

Figure 4-14 Comparison of velocity estimation errors of the 3rd node by the previous method and the proposed method in different directions.

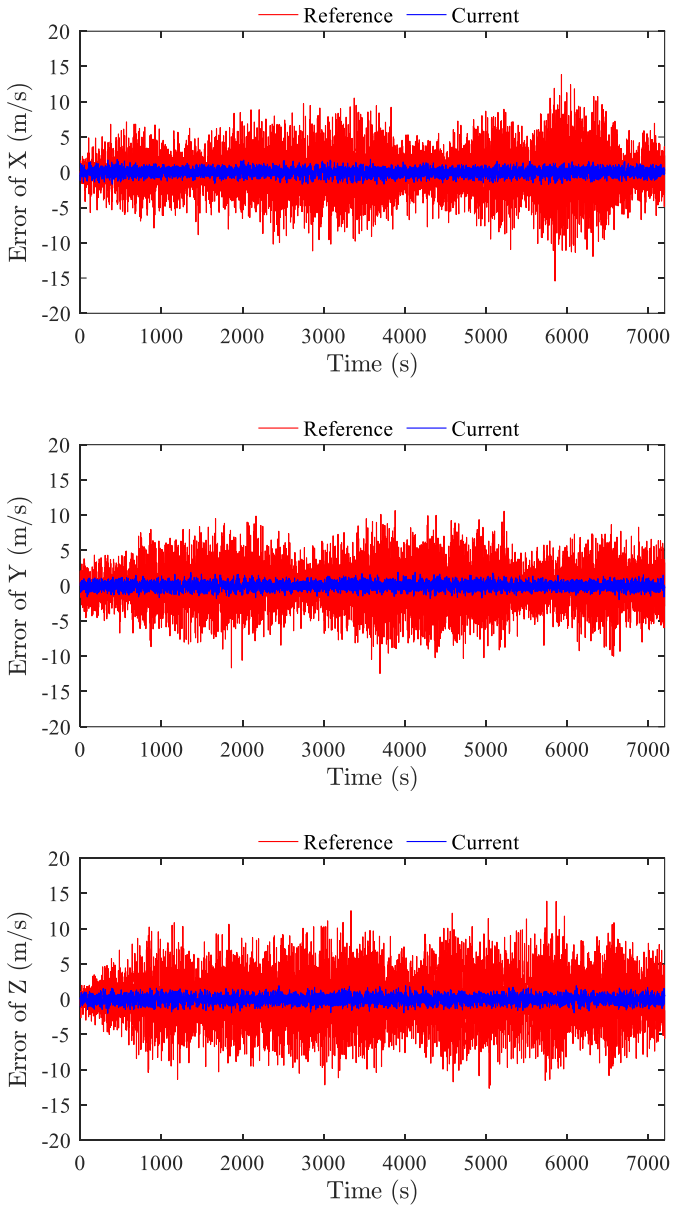

Figure 4-15 Comparison of velocity estimation errors of the 5th node by the previous method and the proposed method in different directions.

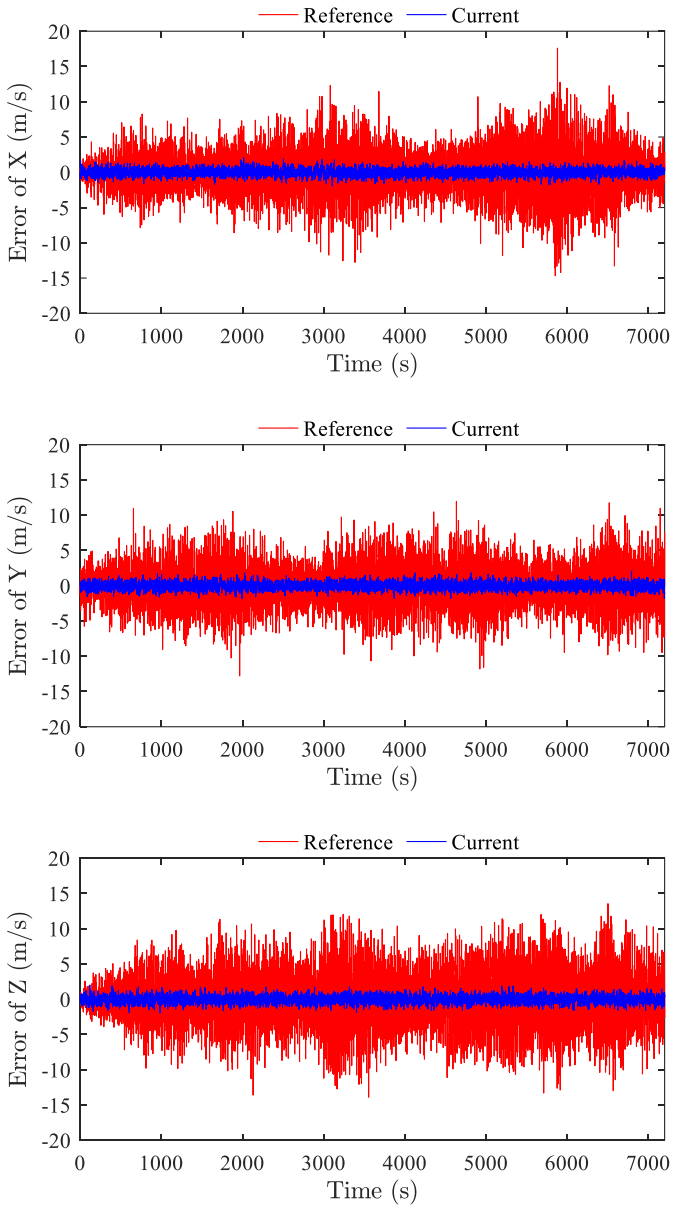

Figure 4-16 Comparison of velocity estimation errors of the 7th node by the previous method and the proposed method in different directions.

Chapter 5 GLOBAL COMPUTATIONAL CONTROL FRAMEWORK OF SPACE TETHERS

Summary: This chapter presents a computational control framework for flexible space tethers, integrated with computational mechanics. Building on the high-fidelity finite element dynamic model and FE-Kalman state estimator developed in the previous chapters, it formulates a moving horizon optimal control approach to regulate tether geometry. The control problem is recast through Hamilton's variational principle as a two-point boundary value problem with a moving terminal boundary condition, and the control inputs are generated numerically for closed-loop feedback control. The related research has been published in **Reference (3)**, as listed in Section 1.6.

5.1. Preliminaries

As shown in Figure 5-1, the conventional control design process begins with a high-fidelity finite-element representation of the flexible tether, from which the dominant dynamic characteristics are extracted to construct a simplified model for subsequent analytical controller development. Extending beyond this conventional framework, the proposed computational control approach eliminates the intermediate model-simplification step and enables feedback controller synthesis directly from the high-fidelity model. By preserving the fidelity of the original model and constructing the control law numerically,

this formulation avoids the difficulty of deriving closed-form analytical controllers for high-dimensional tether systems.

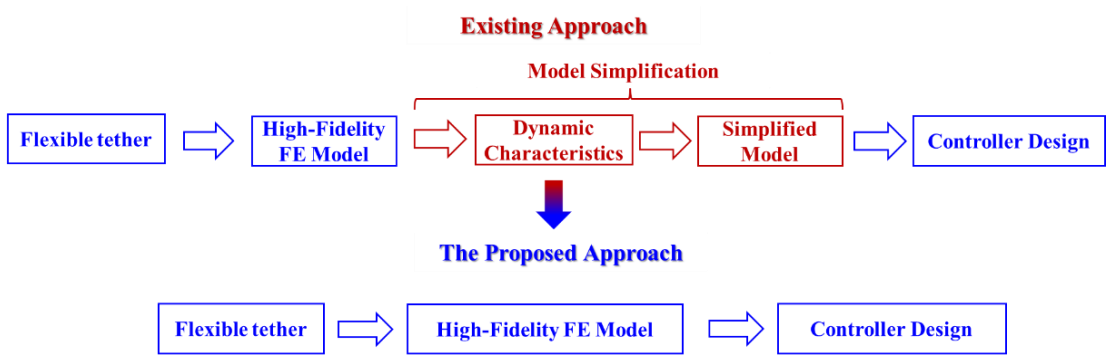

Figure 5-1. Evolution diagram of global computational control.

Suppose a TSS orbiting the Earth comprises a main spacecraft and a sub spacecraft connected by a flexible elastic tether. The system actuation is exclusively located on these two spacecraft. Two coordinate frames, the global inertial frame $O-XYZ$ and the local frame $o_j-x_jy_jz_j$ fixed to the jth element, are introduced to describe the tether dynamics as illustrated in Figure 5-2. The origin of the global frame is located at the center of the Earth with its *Z*-axis aligned with Earth's rotation axis, *X*-axis pointing to the equinox, and *Y*-axis completing a right-hand frame. The origin of the local frame is located at one end of the jth element with y_j -axis along the element length.

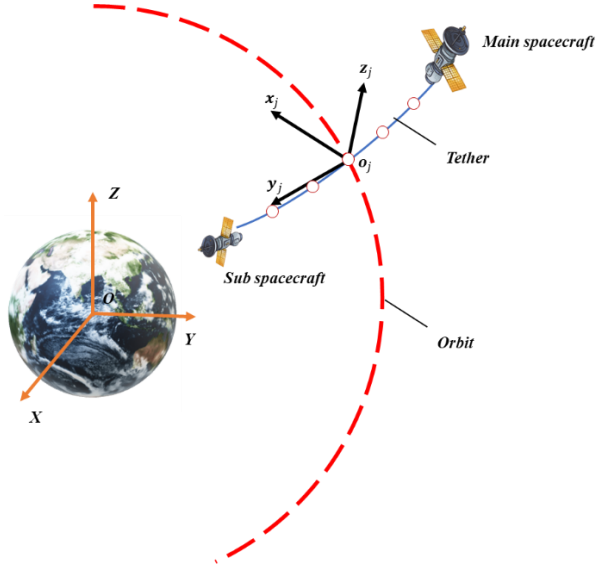

Figure 5-2. Schematic diagram of the TSS model.

Based on Ref. [72], the following assumptions are employed in establishing the tether dynamics: (i) the system is in an ideal circular orbit. (ii) the spacecraft are represented as lumped masses due to the enormous ratio of tether length over spacecraft size; (iii) actuators are located only on the spacecraft; and (iv) the tether is considered isotropic elastic, discretized into (n−1) tensile elements (without compressive stiffness) and n nodes, as depicted in Figure 5-2.

5.2. Computational Feedback Optimal Control

The dynamic model of the flexible tethers is described as Eq. (4.2), such that

$$\dot{\tilde{\boldsymbol{X}}} = \boldsymbol{A}_d \tilde{\boldsymbol{X}} + \boldsymbol{B}_d \boldsymbol{u}_d + \boldsymbol{F}^{ext} \tag{5.1}$$

To design a computational optimal controller for the regulation of the flexible tether, a quadratic function is selected as the step cost function, such that

$$L\left(\tilde{\boldsymbol{X}},\boldsymbol{u}_d\right)=\frac{1}{2}\left(\tilde{\boldsymbol{X}}_d-\tilde{\boldsymbol{X}}\right)^{\mathrm{T}}\boldsymbol{R}^O\left(\tilde{\boldsymbol{X}}_d-\tilde{\boldsymbol{X}}\right)+\frac{1}{2}\boldsymbol{u}_d{}^{\mathrm{T}}\boldsymbol{Q}^O\boldsymbol{u}_d \tag{5.2}$$

where $\boldsymbol{Q}^O$ and $\boldsymbol{R}^O$ are both positive definite matrices.

The terminal cost function is defined as

$$\varphi\left(\tilde{\boldsymbol{X}}\left(T\right),T\right)=0 \tag{5.3}$$

The boundary conditions of the optimal control are written as

$$\tilde{\boldsymbol{X}}\left(t_0\right)=\tilde{\boldsymbol{X}}_0;\ \tilde{\boldsymbol{X}}^e\left(T\right)=\tilde{\boldsymbol{X}}_d^e \tag{5.4}$$

Hence, the optimal control problem can be defined as

$$\begin{aligned}\underset{\tilde{\boldsymbol{X}},\boldsymbol{u}_d}{\operatorname{argmin}}\ J&=\int_{t_0}^{T}\frac{1}{2}\left(\tilde{\boldsymbol{X}}_d-\tilde{\boldsymbol{X}}\right)^{\mathrm{T}}\boldsymbol{R}^O\left(\tilde{\boldsymbol{X}}_d-\tilde{\boldsymbol{X}}\right)+\frac{1}{2}\boldsymbol{u}_d^{\mathrm{T}}\boldsymbol{Q}^O\boldsymbol{u}_d dt\\ &\dot{\tilde{\boldsymbol{X}}}=\boldsymbol{A}_d\tilde{\boldsymbol{X}}+\boldsymbol{B}_d\boldsymbol{u}_d+\boldsymbol{F}^{ext};\\ \text{subject to}\quad&\tilde{\boldsymbol{X}}\left(t_0\right)=\tilde{\boldsymbol{X}}_0;\\ &\tilde{\boldsymbol{X}}^e\left(T\right)=\tilde{\boldsymbol{X}}_d^e\end{aligned} \tag{5.5}$$

The optimal control problem is to find the input $\boldsymbol{u}^*\left(t\right)$ on the time interval $\left[t_0,T\right]$ that derives the plant along a trajectory $\boldsymbol{x}^*\left(t\right)$ such that the cost function is minimized. Then the augmented objective function is formulated as

$$J'=\int_{t_0}^{T}\left[\frac{1}{2}\left(\tilde{\boldsymbol{X}}_d-\tilde{\boldsymbol{X}}\right)^{\mathrm{T}}\boldsymbol{R}^O\left(\tilde{\boldsymbol{X}}_d-\tilde{\mathbf{X}}\right)+\frac{1}{2}\boldsymbol{u}_d^{\mathrm{T}}\boldsymbol{Q}^O\boldsymbol{u}_d+\boldsymbol{\lambda}\left(t\right)^{\mathrm{T}}\left(\boldsymbol{A}_d\tilde{\boldsymbol{X}}+\boldsymbol{B}_d\boldsymbol{u}_d+\boldsymbol{F}^{ext}-\dot{\tilde{\boldsymbol{X}}}\right)\right]dt \tag{5.6}$$

If we define the Hamiltonian function as

$$H\left(\boldsymbol{x},\boldsymbol{u},t\right)=\frac{1}{2}\left(\tilde{\boldsymbol{X}}_d-\tilde{\boldsymbol{X}}\right)^{\mathrm{T}}\boldsymbol{R}^O\left(\tilde{\boldsymbol{X}}_d-\tilde{\boldsymbol{X}}\right)+\frac{1}{2}\boldsymbol{u}_d^{\mathrm{T}}\boldsymbol{Q}^O\boldsymbol{u}_d+\boldsymbol{\lambda}\left(t\right)^{\mathrm{T}}\left(\boldsymbol{A}_d\tilde{\boldsymbol{X}}+\boldsymbol{B}_d\boldsymbol{u}_d+\boldsymbol{F}^{ext}\right)$$

(5.7)

Then we can rewrite the augmented objective function as

$$J' = \int_{t_0}^{T} \left[H\left(\tilde{\boldsymbol{X}}, \boldsymbol{u}_d, t\right) - \boldsymbol{\lambda}(t)^{\mathrm{T}} \dot{\tilde{\boldsymbol{X}}} \right] dt \tag{5.8}$$

Considering the first-order variation of the above equation, we have

$$\begin{aligned}
\delta J' &== \int_{t_0}^{T} \left[\delta \boldsymbol{u}_d H_{\boldsymbol{u}} + \delta \tilde{\boldsymbol{X}}^{\mathrm{T}} H_x - \delta \dot{\tilde{\boldsymbol{X}}}^{\mathrm{T}} \boldsymbol{\lambda} + \delta \boldsymbol{\lambda}^{\mathrm{T}} \left(H_{\lambda} - \dot{\tilde{\boldsymbol{X}}} \right) \right] dt \\
&= \int_{t_0}^{T} \left[\delta \boldsymbol{u}_d H_{\mathbf{u}} + \delta \tilde{\boldsymbol{X}}^{\mathrm{T}} H_x - \delta \tilde{\boldsymbol{X}}^{\mathrm{T}} \boldsymbol{\lambda} + \delta \tilde{\boldsymbol{X}}^{\mathrm{T}} \dot{\boldsymbol{\lambda}} + \delta \boldsymbol{\lambda}^{\mathrm{T}} \left(H_{\lambda} - \dot{\tilde{\boldsymbol{X}}} \right) \right] dt \\
&== \int_{t_0}^{T} \left[\delta \boldsymbol{u}_d H_{\boldsymbol{u}} + \delta \tilde{\boldsymbol{X}}^{\mathrm{T}} H_x + \delta \tilde{\boldsymbol{X}}^{\mathrm{T}} \dot{\boldsymbol{\lambda}} + \delta \boldsymbol{\lambda}^{\mathrm{T}} \left(H_{\lambda} - \dot{\tilde{\boldsymbol{X}}} \right) \right] dt - \delta \tilde{\boldsymbol{X}}^{\mathrm{T}} \boldsymbol{\lambda} \Big|_{t_0}^{T} \\
&= \int_{t_0}^{T} \left[\delta \boldsymbol{u}_d H_{\mathbf{u}} + \delta \tilde{\boldsymbol{X}}^{\mathrm{T}} \left(H_x + \dot{\boldsymbol{\lambda}} \right) + \delta \boldsymbol{\lambda}^{\mathrm{T}} \left(H_{\lambda} - \dot{\tilde{\boldsymbol{X}}} \right) \right] dt = 0
\end{aligned} \tag{5.9}$$

where,

$$H_{\boldsymbol{u}} = \frac{\partial H}{\partial \boldsymbol{u}_d}, \; H_x = \frac{\partial H}{\partial \tilde{\boldsymbol{X}}}, \text{ and } \; H_{\lambda} = \frac{\partial H}{\partial \boldsymbol{\lambda}} \tag{5.10}$$

Thus, the first-order necessary conditions for the problem, including state equations, costate equations and stationarity conditions, are obtained as follows:

$$\frac{\partial H}{\partial \boldsymbol{\lambda}} = \dot{\tilde{\boldsymbol{X}}} \tag{5.11}$$

$$\frac{\partial H}{\partial \tilde{\boldsymbol{X}}} = -\dot{\boldsymbol{\lambda}} \tag{5.12}$$

$$\frac{\partial H}{\partial \boldsymbol{u}_d} = \mathbf{0} \tag{5.13}$$

The control variable can be expressed as a function of state and costate variables by solving Eq. (5.13), and then the Hamiltonian can be reformulated as a functional of state

and costate variables as $H\left(\tilde{\boldsymbol{X}},\boldsymbol{\lambda},t\right)$. Finally, the necessary conditions in Eqs. (5.11)- (5.12) can be written as the following Hamiltonian TPBVP.

$$\dot{\tilde{\boldsymbol{X}}}=\frac{\partial H\left(\tilde{\boldsymbol{X}},\boldsymbol{\lambda},t\right)}{\partial\boldsymbol{\lambda}} \tag{5.14}$$

$$-\dot{\boldsymbol{\lambda}}=\frac{\partial H\left(\tilde{\boldsymbol{X}},\boldsymbol{\lambda},t\right)}{\partial\tilde{\boldsymbol{X}}} \tag{5.15}$$

Substituting the Hamiltonian as Eq. (5.7) into the stationarity condition, we have

$$\frac{\partial H}{\partial\boldsymbol{u}_d}=\boldsymbol{Q}^O\boldsymbol{u}_d+\boldsymbol{B}_d^{\mathrm{T}}\boldsymbol{\lambda}=\boldsymbol{0} \tag{5.16}$$

Solving the above equation, we obtained,

$$\boldsymbol{u}_d=-\left(\boldsymbol{Q}^O\right)^{-1}\boldsymbol{B}_d^{\mathrm{T}}\boldsymbol{\lambda} \tag{5.17}$$

Then the Hamiltonian can be expressed as a functional of state and costate variables, such that

$$H\left(\tilde{\boldsymbol{X}}_d,\boldsymbol{\lambda},t\right)=\frac{1}{2}\left(\tilde{\boldsymbol{X}}_d-\tilde{\boldsymbol{X}}\right)^{\mathrm{T}}\boldsymbol{R}^O\left(\tilde{\boldsymbol{X}}_d-\tilde{\boldsymbol{X}}\right)+\frac{1}{2}\boldsymbol{\lambda}^{\mathrm{T}}\boldsymbol{B}_d\boldsymbol{Q}^{O-1}\boldsymbol{B}_d^{\mathrm{T}}\boldsymbol{\lambda}+\boldsymbol{\lambda}^{\mathrm{T}}\left(\boldsymbol{A}_d\tilde{\boldsymbol{X}}-\boldsymbol{B}_d\boldsymbol{Q}^{O-1}\boldsymbol{B}_d^{\mathrm{T}}\boldsymbol{\lambda}+\boldsymbol{F}^{ext}\right) \tag{5.18}$$

Substituting Eq. (5.18) into the state equation and the costate equation yields,

$$\begin{aligned}\dot{\tilde{\boldsymbol{X}}}&=\frac{\partial H}{\partial\boldsymbol{\lambda}}=\boldsymbol{A}_d\tilde{\boldsymbol{X}}-\boldsymbol{B}_d\boldsymbol{Q}^{-1}\boldsymbol{B}_d^{\mathrm{T}}\boldsymbol{\lambda}+\boldsymbol{F}^{ext}\\ \dot{\boldsymbol{\lambda}}&=-\frac{\partial H}{\partial\tilde{\boldsymbol{X}}}=-\boldsymbol{R}^O\left(\tilde{\boldsymbol{X}}_d-\tilde{\boldsymbol{X}}\right)-\left(\boldsymbol{A}_d^{\mathrm{T}}\boldsymbol{\lambda}+\tilde{\boldsymbol{X}}^{\mathrm{T}}\left(\frac{\partial\boldsymbol{A}_d}{\partial\tilde{\boldsymbol{X}}}\right)^{\mathrm{T}}\boldsymbol{\lambda}\right)\end{aligned} \tag{5.19}$$

where,

$$\frac{\partial \boldsymbol{A}_d}{\partial \tilde{\boldsymbol{X}}}\tilde{\boldsymbol{X}}=\left[\frac{\partial \boldsymbol{A}_d}{\partial X_{t,1}}\tilde{\boldsymbol{X}},\frac{\partial \boldsymbol{A}_d}{\partial Y_{t,1}}\tilde{\boldsymbol{X}},\frac{\partial \boldsymbol{A}_d}{\partial Z_{t,1}}\tilde{\boldsymbol{X}}\quad,\cdots,\quad\frac{\partial \boldsymbol{A}_d}{\partial X_{t,n}}\tilde{\boldsymbol{X}},\frac{\partial \boldsymbol{A}_d}{\partial Y_{t,n}}\tilde{\boldsymbol{X}},\frac{\partial \boldsymbol{A}_d}{\partial Z_{t,n}}\tilde{\boldsymbol{X}},\frac{\partial \boldsymbol{A}_d}{\partial \dot{X}_{t,1}}\tilde{\boldsymbol{X}},\frac{\partial \boldsymbol{A}_d}{\partial \dot{Y}_{t,1}}\tilde{\boldsymbol{X}},\frac{\partial \boldsymbol{A}_d}{\partial \dot{Z}_{t,1}}\tilde{\boldsymbol{X}}\quad,\cdots,\quad\frac{\partial \boldsymbol{A}_d}{\partial \dot{X}_{t,n}}\tilde{\boldsymbol{X}},\frac{\partial \boldsymbol{A}_d}{\partial \dot{Y}_{t,n}}\tilde{\boldsymbol{X}},\frac{\partial \boldsymbol{A}_d}{\partial \dot{Z}_{t,n}}\tilde{\boldsymbol{X}}\right]$$

(5.20)

Substituting Eq. (4.3) into $\frac{\partial \boldsymbol{A}_d}{\partial X_{t,k}}$, $\frac{\partial \boldsymbol{A}_d}{\partial Y_{t,k}}$, and $\frac{\partial \boldsymbol{A}_d}{\partial Z_{t,k}}$ (k=1, 2, 3,… ,n) one has

$$\frac{\partial \boldsymbol{A}_d}{\partial X_{t,k}}=\begin{bmatrix}\mathbf{0} & \mathbf{I}_{3n\times 3n}\\ -\boldsymbol{M}_t^{-1}\dfrac{\partial \boldsymbol{K}_t}{\partial X_{t,k}} & -\boldsymbol{M}_t^{-1}\dfrac{\partial \boldsymbol{C}_t}{\partial X_{t,k}}\end{bmatrix},\qquad \frac{\partial \boldsymbol{A}_d}{\partial \dot{X}_{t,k}}=\mathbf{0} \tag{5.21}$$

$$\frac{\partial \boldsymbol{A}_d}{\partial Y_{t,k}}=\begin{bmatrix}\mathbf{0} & \mathbf{I}_{3n\times 3n}\\ -\boldsymbol{M}_t^{-1}\dfrac{\partial \boldsymbol{K}_t}{\partial Y_{t,k}} & -\boldsymbol{M}_t^{-1}\dfrac{\partial \boldsymbol{C}_t}{\partial Y_{t,k}}\end{bmatrix},\qquad \frac{\partial \boldsymbol{A}_d}{\partial \dot{Y}_{t,k}}=\mathbf{0} \tag{5.22}$$

$$\frac{\partial \boldsymbol{A}_d}{\partial Z_{t,k}}=\begin{bmatrix}\mathbf{0} & \mathbf{I}_{3n\times 3n}\\ -\boldsymbol{M}_t^{-1}\dfrac{\partial \boldsymbol{K}_t}{\partial Z_{t,k}} & -\boldsymbol{M}_{t,k}^{-1}\dfrac{\partial \boldsymbol{C}_t}{\partial Z_{t,k}}\end{bmatrix},\qquad \frac{\partial \boldsymbol{A}_d}{\partial \dot{Z}_{t,k}}=\mathbf{0} \tag{5.23}$$

where $\boldsymbol{C}_t=\left[\alpha_t\boldsymbol{M}_t+\beta_t\boldsymbol{K}_t\right]\in\mathbb{R}^{3n\times 3n}$ is the Rayleigh damping with α_t and β_t being damping coefficients, such that,

$$\frac{\partial \boldsymbol{C}_t}{\partial X_{t,k}}=\alpha_t\frac{\partial \boldsymbol{M}_t}{\partial X_{t,k}}+\beta_t\frac{\partial \boldsymbol{K}_t}{\partial X_{t,k}}=\beta_t\frac{\partial \boldsymbol{K}_t}{\partial X_{t,k}} \tag{5.24}$$

$$\frac{\partial \boldsymbol{C}_t}{\partial Y_{t,k}}=\alpha_t\frac{\partial \boldsymbol{M}_t}{\partial Y_{t,k}}+\beta_t\frac{\partial \boldsymbol{K}_t}{\partial Y_{t,k}}=\beta_t\frac{\partial \boldsymbol{K}_t}{\partial Y_{t,k}} \tag{5.25}$$

$$\frac{\partial \boldsymbol{C}_t}{\partial Z_{t,k}}=\alpha_t\frac{\partial \boldsymbol{M}_t}{\partial Z_{t,k}}+\beta_t\frac{\partial \boldsymbol{K}_t}{\partial Z_{t,k}}=\beta_t\frac{\partial \boldsymbol{K}_t}{\partial Z_{t,k}} \tag{5.26}$$

Hence, to obtain the detailed expression of Eqs. (5.24) - (5.26), $\frac{\partial \boldsymbol{K}_t}{\partial X_{t,k}}$, $\frac{\partial \boldsymbol{K}_t}{\partial Y_{t,k}}$ and $\frac{\partial \boldsymbol{K}_t}{\partial Z_{t,k}}$ are derived. Similar to the procedure to calculate the stiffness matrix $\boldsymbol{K}_t$ in the FEM, $\frac{\partial \boldsymbol{K}_t}{\partial X_{t,k}}$, $\frac{\partial \boldsymbol{K}_t}{\partial Y_{t,k}}$ and $\frac{\partial \boldsymbol{K}_t}{\partial Z_{t,k}}$ need to be formulated first. According to Section 3.2, the stiffness matrix of the jth element can be expressed as

$$\boldsymbol{K}_{t,j} = E_t A_{t,j} L_{t,j} \boldsymbol{B}_{t,j}{}^{\mathrm{T}} \boldsymbol{B}_{t,j} \tag{5.27}$$

$$\boldsymbol{B}_{t,j} = \begin{bmatrix} -\frac{X_{t,j+1}-X_{t,j}}{L_{t0,j}L_{t,j}} & -\frac{Y_{t,j+1}-Y_{t,j}}{L_{t0,j}L_{t,j}} & -\frac{Z_{t,j+1}-Z_{t,j}}{L_{t0,j}L_{t,j}} & \frac{X_{t,j+1}-X_{t,j}}{L_{t0,j}L_{t,j}} & \frac{Y_{t,j+1}-Y_{t,j}}{L_{t0,j}L_{j}} & \frac{Z_{t,j+1}-Z_{t,j}}{L_{t0,j}L_{t,j}} \end{bmatrix} \tag{5.28}$$

where $\boldsymbol{B}_{t,j}$ is the strain matrix at the global frame.

Substituting Eq. (5.27) into $\frac{\partial \boldsymbol{K}_{t,j}}{\partial X_{t,j}}$ leads,

$$\boldsymbol{K}^{x'}_{t,jk} = \frac{\partial \boldsymbol{K}_{t,j}}{\partial X_{t,k}} = 2E_t A_{t,j} L_{t,j} \frac{\partial \boldsymbol{B}_{t,j}{}^{\mathrm{T}}}{\partial X_{t,k}} \boldsymbol{B}_{t,j} \tag{5.29}$$

where,

$$\begin{cases} \dfrac{\partial \boldsymbol{B}_{t,j}{}^{\mathrm{T}}}{\partial X_{t,k}} = \dfrac{1}{L_{t0,j}L_{t,j}} \begin{bmatrix} 1 & 0 & 0 & -1 & 0 & 0 \end{bmatrix}, \ (k=j) \\ \dfrac{\partial \boldsymbol{B}_{t,j}{}^{\mathrm{T}}}{\partial X_{t,k}} = \dfrac{1}{L_{t0,j}L_{t,j}} \begin{bmatrix} -1 & 0 & 0 & 1 & 0 & 0 \end{bmatrix}, \ (k=j+1) \\ \dfrac{\partial \boldsymbol{B}_{t,j}{}^{\mathrm{T}}}{\partial X_{t,k}} = \dfrac{1}{L_{t0,j}L_{t,j}} \begin{bmatrix} 0 & 0 & 0 & 0 & 0 & 0 \end{bmatrix}, \ \text{else} \end{cases} \tag{5.30}$$

Further, the derivative of the jth element stiffness matrix with respect to $X_{t,k}$ can be represented as

$$\boldsymbol{K}_{t,jk}^{x'} = -\frac{2E_t A_{t,j}}{L_{t,j} L_{t0,j}} \begin{bmatrix} \cos\theta_{jx} & \cos\theta_{jy} & \cos\theta_{jz} & -\cos\theta_{jx} & -\cos\theta_{jy} & -\cos\theta_{jz} \\ 0 & 0 & 0 & 0 & 0 & 0 \\ 0 & 0 & 0 & 0 & 0 & 0 \\ -\cos\theta_{jx} & -\cos\theta_{jy} & -\cos\theta_{jz} & \cos\theta_{jx} & \cos\theta_{jy} & \cos\theta_{jz} \\ 0 & 0 & 0 & 0 & 0 & 0 \\ 0 & 0 & 0 & 0 & 0 & 0 \end{bmatrix}, \ (k = j) \tag{5.31}$$

$$\boldsymbol{K}_{t,jk}^{x'} = \frac{2E_t A_{t,j}}{L_{t,j} L_{t0,j}} \begin{bmatrix} \cos\theta_{jx} & \cos\theta_{jy} & \cos\theta_{jz} & -\cos\theta_{jx} & -\cos\theta_{jy} & -\cos\theta_{jz} \\ 0 & 0 & 0 & 0 & 0 & 0 \\ 0 & 0 & 0 & 0 & 0 & 0 \\ -\cos\theta_{jx} & -\cos\theta_{jy} & -\cos\theta_{jz} & \cos\theta_{jx} & \cos\theta_{jy} & \cos\theta_{jz} \\ 0 & 0 & 0 & 0 & 0 & 0 \\ 0 & 0 & 0 & 0 & 0 & 0 \end{bmatrix}, (k = j+1) \tag{5.32}$$

$$\boldsymbol{K}_{t,jk}^{x'} = \boldsymbol{0}, \text{ else}$$

Similarly, the derivative of the jth element stiffness matrix with respect to $Y_{t,k}$ can be expressed as

$$\boldsymbol{K}_{t,jk}^{y'} = -\frac{2E_t A_{t,j}}{L_{t,j} L_{t0,j}} \begin{bmatrix} 0 & 0 & 0 & 0 & 0 & 0 \\ \cos\theta_{jx} & \cos\theta_{jy} & \cos\theta_{jz} & -\cos\theta_{jx} & -\cos\theta_{jy} & -\cos\theta_{jz} \\ 0 & 0 & 0 & 0 & 0 & 0 \\ 0 & 0 & 0 & 0 & 0 & 0 \\ -\cos\theta_{jx} & -\cos\theta_{jy} & -\cos\theta_{jz} & \cos\theta_{jx} & \cos\theta_{jy} & \cos\theta_{jz} \\ 0 & 0 & 0 & 0 & 0 & 0 \end{bmatrix}, \ (k = j)$$

(5.33)

$$\boldsymbol{K}_{t,jk}^{y'} = -\frac{2E_t A_{t,j}}{L_{t,j} L_{t0,j}} \begin{bmatrix} 0 & 0 & 0 & 0 & 0 & 0 \\ \cos\theta_{jx} & \cos\theta_{jy} & \cos\theta_{jz} & -\cos\theta_{jx} & -\cos\theta_{jy} & -\cos\theta_{jz} \\ 0 & 0 & 0 & 0 & 0 & 0 \\ 0 & 0 & 0 & 0 & 0 & 0 \\ -\cos\theta_{jx} & -\cos\theta_{jy} & -\cos\theta_{jz} & \cos\theta_{jx} & \cos\theta_{jy} & \cos\theta_{jz} \\ 0 & 0 & 0 & 0 & 0 & 0 \end{bmatrix}, (k = j+1)$$

(5.34)

$$\boldsymbol{K}_{t,jk}^{y'} = \mathbf{0}, \text{ else} \tag{5.35}$$

Besides, the derivative of the jth element stiffness matrix with respect to $Z_{t,k}$ can be represented as

$$\boldsymbol{K}_{t,jk}^{z'} = -\frac{2E_t A_{t,j}}{L_{t,j} L_{t0,j}} \begin{bmatrix} 0 & 0 & 0 & 0 & 0 & 0 \\ 0 & 0 & 0 & 0 & 0 & 0 \\ \cos\theta_{jx} & \cos\theta_{jy} & \cos\theta_{jz} & -\cos\theta_{jx} & -\cos\theta_{jy} & -\cos\theta_{jz} \\ 0 & 0 & 0 & 0 & 0 & 0 \\ 0 & 0 & 0 & 0 & 0 & 0 \\ -\cos\theta_{jx} & -\cos\theta_{jy} & -\cos\theta_{jz} & \cos\theta_{jx} & \cos\theta_{jy} & \cos\theta_{jz} \end{bmatrix}, (k = j)$$

(5.36)

$$\boldsymbol{K}_{t,jk}^{z'} = \frac{2E_t A_{t,j}}{L_{t,j} L_{t0,j}} \begin{bmatrix} 0 & 0 & 0 & 0 & 0 & 0 \\ 0 & 0 & 0 & 0 & 0 & 0 \\ \cos\theta_{jx} & \cos\theta_{jy} & \cos\theta_{jz} & -\cos\theta_{jx} & -\cos\theta_{jy} & -\cos\theta_{jz} \\ 0 & 0 & 0 & 0 & 0 & 0 \\ 0 & 0 & 0 & 0 & 0 & 0 \\ -\cos\theta_{jx} & -\cos\theta_{jy} & -\cos\theta_{jz} & \cos\theta_{jx} & \cos\theta_{jy} & \cos\theta_{jz} \end{bmatrix}, (k = j+1)$$

(5.37)

$$\boldsymbol{K}_{t,jk}^{z'} = \mathbf{0}\text{, else} \tag{5.38}$$

The derivative of the stiffness matrix of the system with respect to $X_{t,j}, Y_{t,j}, Z_{t,j}$ is respectively obtained by assembling the derivative of all element stiffness matrices based on the standard assembly procedure in FEM. Then the detailed expression of Eq. (5.20) can be given. Consequently, the explicit expression of Eq. (5.19) is reformulated. The trajectory of the state can be derived by solving this equation. By substituting $\tilde{\boldsymbol{X}}$ and $\boldsymbol{\lambda}$ into Eq. (5.17), we obtain an open-loop numerical controller that guides the system from the initial position to the desired trajectory.

However, errors in open-loop control are unavoidable due to modeling uncertainties, inaccurate initial conditions, environmental disturbances, and state estimation errors. To compensate for these effects, a feedback control framework based on model predictive control theory is introduced, in which the proposed open-loop computational control input is updated based on the latest state information as follows. After the (i-1)th time $i = (0,1,2,\cdots,m)$ the boundary conditions at the time t_i are updated with a shortened horizon,

$$\tilde{\boldsymbol{X}}(t_i) = \tilde{\boldsymbol{X}}_i \,;\, \tilde{\boldsymbol{X}}^e(T) = \tilde{\boldsymbol{X}}_d^e \tag{5.39}$$

where $\tilde{\boldsymbol{X}}_i$ is the feedback from the designed state estimator.

Then the control input $\boldsymbol{u}_d^i$ can be recalculated by solving the Eq. (5.19) with the new boundary condition and is applied to the system by interpolating the control input $\boldsymbol{u}_d^{i-1}$

from the previous optimization. Finally, the control input $\boldsymbol{u}_d^i$ can be obtained in terms of $i = 1, 2, \cdots, m$ following the same process, recursively. The implementation process is shown in Figure 5-3. The proposed computational control method provides a more general and adaptive framework for elastic system control by enabling automated, algorithm-driven controller design within a standardized FEM-based framework. By operating directly on high-fidelity dynamic models, it preserves the physical accuracy and distributed characteristics of the original system without relying on reduced-order approximations for analytical controller derivation. In addition, by replacing fixed closed-form control laws with numerical algorithms, the framework offers greater flexibility in handling complex dynamic behavior and evolving system configurations.

Controllability: The controllability of the tethered space system has been rigorously established in prior literature [113–115,72].

Stability: In this study, the stability of the closed-loop system is examined within a nonlinear receding horizon control framework. The asymptotic stability of nonlinear receding horizon control is analyzed through the monotonicity of the optimal cost function. This monotonicity property is guaranteed when a terminal equality constraint $\tilde{\boldsymbol{X}}^e\left(T\right) = \tilde{\boldsymbol{X}}_d^e$ is applied [72,116–118]. Although the high-fidelity representation of tether elasticity based on NPFEM/ANCF substantially increases the dimension of the state space, the theoretical stability properties of the nonlinear receding horizon control scheme remain unchanged. By explicitly penalizing elastic potential energy and strain-rate-related terms in the state-

dependent stage cost, the controller suppresses both rigid-body librational motion and high-frequency elastic vibrations. In practical implementation, small residual oscillations may arise because of spatiotemporal discretization and numerical solver tolerances. Nevertheless, the closed-loop system remains practically stable within an invariant neighborhood of the equilibrium.

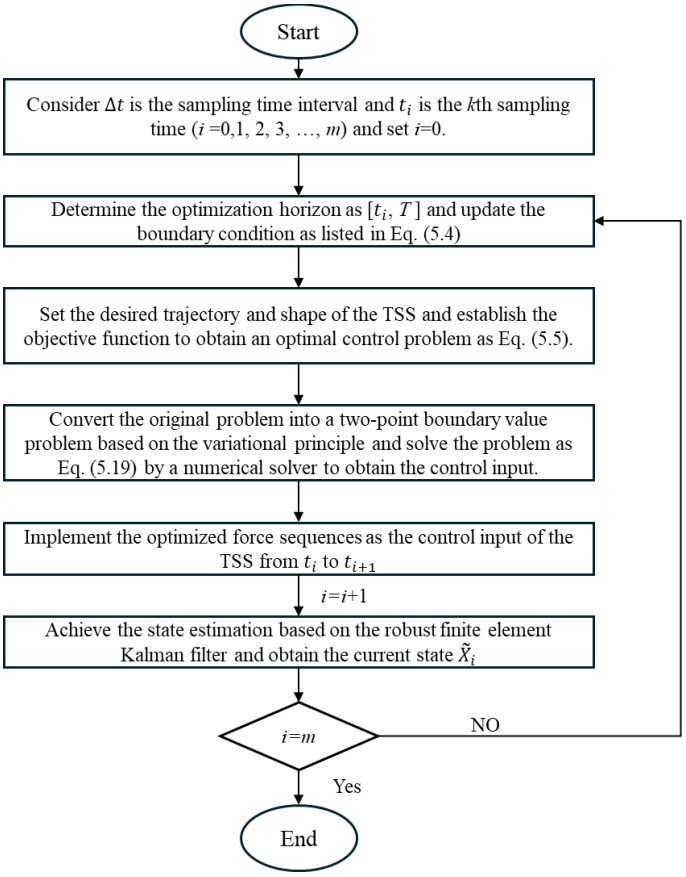

Figure 5-3 Flowchart of the implementation of computational optimal control with state estimator.

5.3. Simulation and Discussion

The effectiveness of the proposed computational control framework is verified through numerical simulations by controlling an initially bent flexible tether with two spacecraft at the ends to its balanced state, i.e., the tether is straight vertically in orbit. As a benchmark, the dynamic behavior of the system without control input is also analyzed and presented. The tethered spacecraft are assumed to be two lumped masses. It is assumed that the center of mass of the system orbits the Earth with an orbital altitude of 600 km in the equatorial orbit within the *X*-*Y* plane, as depicted in Figure 4-3. The physical properties of the space tether are listed in Table 5-1.

In the current work, the flexible space tether is discretized into four tether elements with five nodes based on the convergence analysis in the previous studies [72]. Initially, the tether is bent into a half-circle with both ends located in the local vertical direction, as shown in Figure 5-4. Here, a local *o*-*xy* coordinate system in the orbit plane is used to present simulation results. The FE-Kalman estimator is employed to estimate the state of the internal nodes (No. 2,3,4 nodes) along the tether for the geometric profile feedback control. The simulation runs for 5 hours with and without the proposed computational optimal control. The time step is set as 0.001s, and the weight matrices in the optimal control are assumed as $\boldsymbol{Q}^O = \mathbf{I}_{6\times6} \in \mathbb{R}^{6\times6}$ and $\boldsymbol{R}^O = 10\times\mathbf{I}_{15\times15} \in \mathbb{R}^{15\times15}$, respectively.

Table 5-1 Physical properties of the TSS

Parameter	Value
Mass of main spacecraft (kg)	500

Mass of sub spacecraft (kg)	5
Tether length (m)	500
Density (kg/m^3)	2700
Cross-sectional Area (m^2)	2x10^{-7}
Young's Modulus (GPa)	72

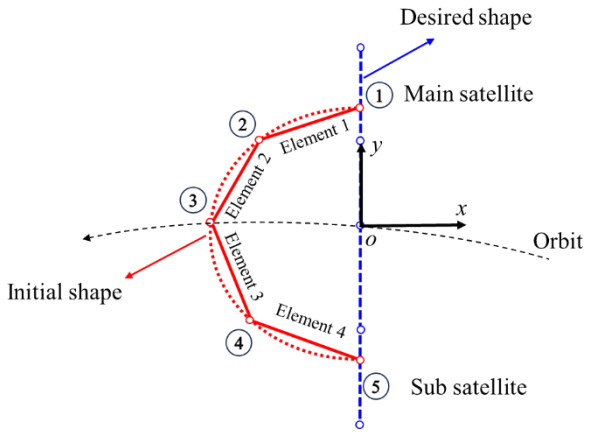

Figure 5-4 The initial and desired geometrical profiles of the flexible tether.

The simulation results are shown in Figure 5-5-Figure 5-10. First, the snapshots of the tether profile at different time instances with and without control are shown in Figure 5-5. Within 2400s, the system almost reaches the desired straight tether in the local vertical direction under the proposed control input, while the tether without control input continues to oscillate between the bent and straight profiles. It shows that the proposed control can quickly guide the tether from its initial shape into the desired geometric profile within a bounded region.

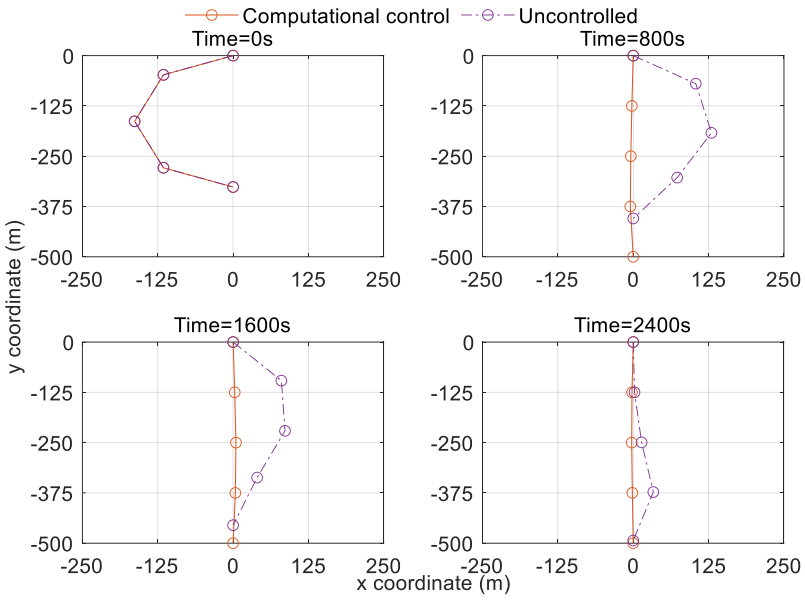

Figure 5-5 Geometric profiles of the tether with and without control at different time instances.

Next, the position errors of the main spacecraft, sub spacecraft, and tether midpoint are shown in Figure 5-6-Figure 5-9. These results show that, under the proposed controller, the position errors of the main spacecraft (Node 1), the sub spacecraft (Node 5), and the tether midpoint rapidly converge toward the desired local vertical position. In contrast, without control, the position errors of the same nodes continue to oscillate. Specifically, the *x*-coordinates of Nodes 1 and 5 oscillate about the local vertical line (x=0). At the same time, the *y*-coordinate of Node 1 remains below its desired value, whereas the *y*-coordinate of Node 5 remains above its desired value. This behavior indicates that, in the absence of control input, the tether continuously oscillates between bent and straight configurations, as illustrated in Figure 5-8. Although complete suppression of oscillations is not possible

because no actuation is applied at the internal tether nodes (Nodes 2, 3, and 4), the proposed control law substantially attenuates these oscillations relative to the uncontrolled flexible tether case.

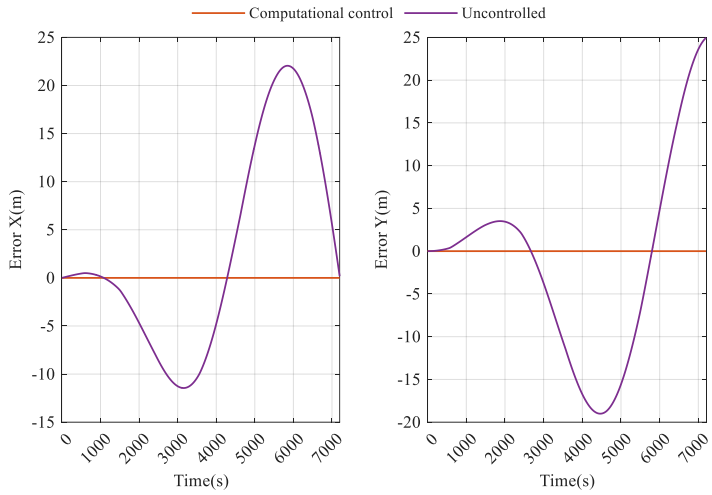

Figure 5-6 Time histories of the position error of Main spacecraft (Node 1).

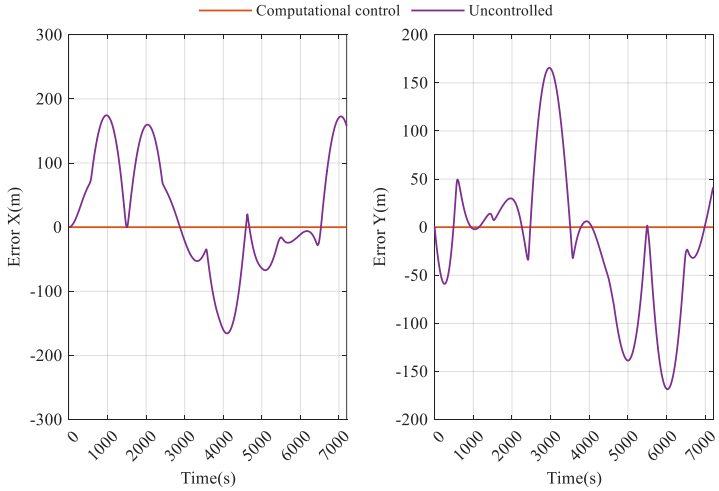

Figure 5-7 Time histories of the position error of Sub spacecraft (Node 5).

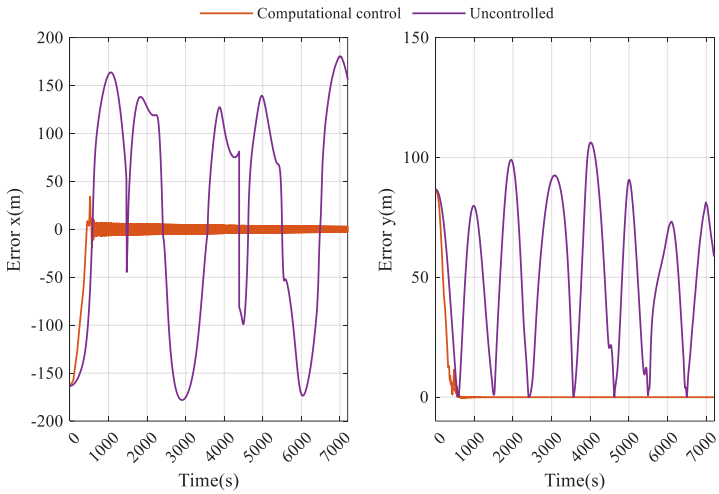

Figure 5-8 Time histories of the position error of the mid-node.

Finally, Figure 5-9 shows the time histories of the tension of each tether element under control. The results clearly indicate that when control is applied, the tether remains taut, and the tension gradually and stably converges to a bounded region as the system reaches the desired straight tether. Figure 5-10 shows that the control inputs applied to both spacecraft are bounded and periodic, enabling them to maintain their designated orbits.

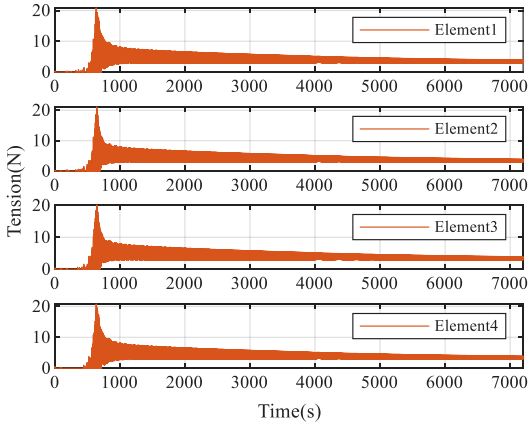

Figure 5-9 Time history of tether tension.

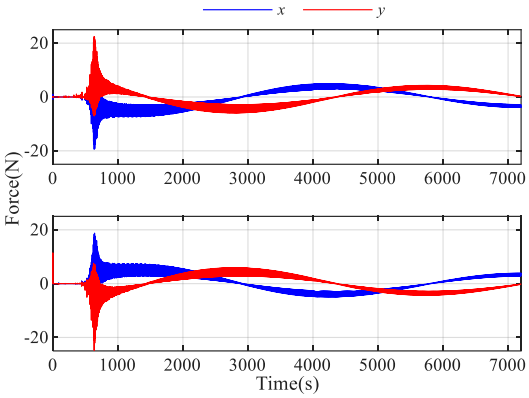

Figure 5-10 Time history of control input.

Chapter 6 CO-LOCATED COMPUTATIONAL CONTROL FRAMEWORK OF SPACE TETHERS

Summary: This chapter presents an automated finite element control framework for tethered space systems. A dual-loop control strategy is developed at the element level to preserve the full-order nonlinear dynamics, with sliding-mode control in the outer loop for robust reference generation and a PD controller with dynamic compensation in the inner loop for efficient trajectory tracking. The overall system control input is obtained by numerically assembling the individual element controllers through the standard finite element assembly procedure. The related research has been published in **Reference (6)**, as listed in Section 1.6.

6.1. Preliminaries

As illustrated in Figure 6-1, unlike conventional control strategies that are ultimately implemented on simplified system-level models, the proposed approach establishes a co-located finite element-based computational control framework by integrating controllers directly into the high-fidelity finite element discretization at the element level. This element-level integration allows control design to be carried out within the original discretized system rather than on a reduced surrogate, thereby preserving distributed dynamic characteristics and providing a unified computational basis for modeling, state

estimation, and feedback control.

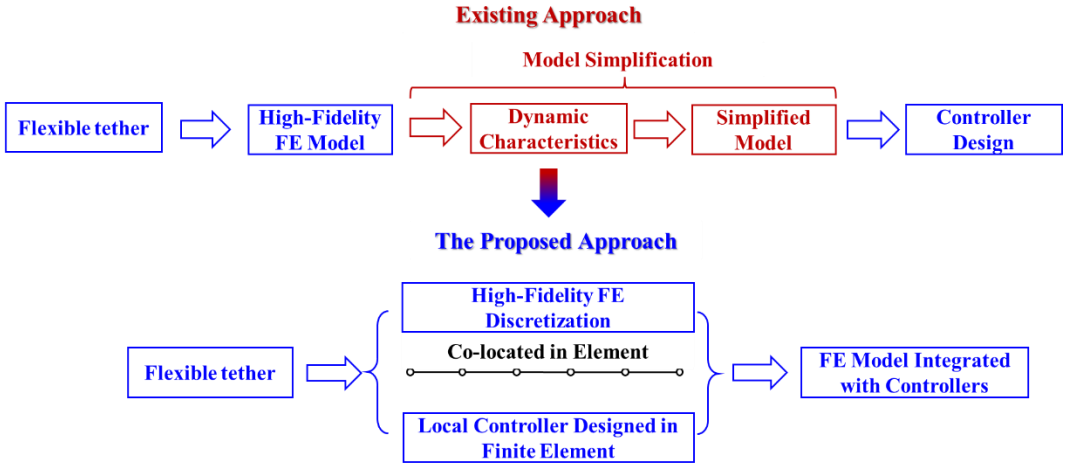

Figure 6-1 Evolution diagram of the co-located computational control.

Consider a TSS traveling in the Earth orbit, as shown in Figure 6-2. The same assumptions adopted in Chapter 5 are used here: (i) the main and sub spacecraft are modeled as lumped masses, (ii) the tether is assumed to be isotropic, elastic, and unable to resist compression, and (iii) actuators are located only on the spacecraft. Finally, for FE modeling, the tether is discretized into $n-1$ tensile-only elements connected by n nodes.

To describe the TSS motion, two coordinate systems are introduced. The global motion of the TSS is described in the global inertial coordinate frame $O-XYZ$, where the origin O is at the center of the Earth with the Z-axis aligned with the Earth's rotational axis, the X-axis directed toward the vernal equinox, and the Y-axis completing a right-handed coordinate system. The dynamics of the tether element is described in the body-fixed local coordinate frame $o_j - x_j y_j z_j$. Its origin o_j is fixed at the end of the jth node of the jth element with the y_j-axis along the tether and pointing to the $(j+1)^{\text{th}}$ node, the other end of

the element. The local tether dynamics is transformed into the global coordinate frame by the coordinate transformation.

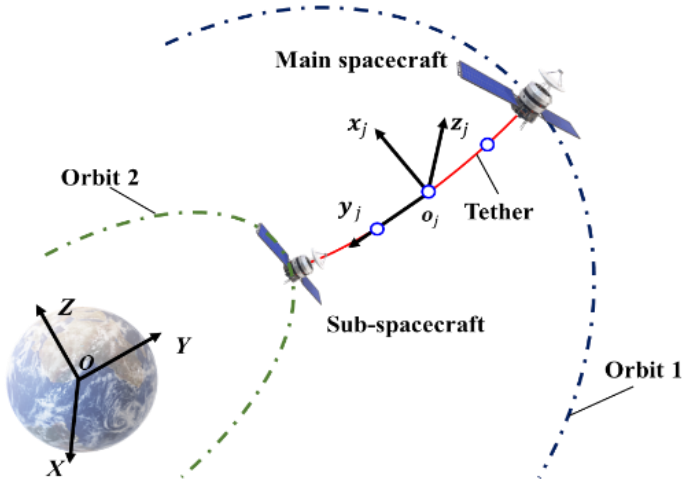

Figure 6-2 Schematic of the TSS in space.

6.2. System Model with Disturbance

Considering the approximation errors and model uncertainties, Eq. (3.12) can be rewritten

$$\boldsymbol{M}_{t,j}\ddot{\boldsymbol{X}}_{t,j}+\boldsymbol{K}_{t,j}\boldsymbol{X}_{t,j}+\boldsymbol{C}_{t,j}\dot{\boldsymbol{X}}_{t,j}-\boldsymbol{F}^{g}_{t,j}-\boldsymbol{F}^{d}_{t,j}-\boldsymbol{F}^{0}_{t,j}+\boldsymbol{d}_{j}=\boldsymbol{0} \tag{6.1}$$

where $\boldsymbol{d}_j$ represents the bounded disturbance due to approximation errors and model uncertainties.

The global governing equation of motion for the space tether is obtained by assembling Eq. (6.1) with the standard FE assembly procedure,

$$\boldsymbol{M}_t\ddot{\boldsymbol{X}}_t + \boldsymbol{K}_t\boldsymbol{X}_t + \boldsymbol{C}_t\dot{\boldsymbol{X}}_t - \boldsymbol{F}_t^g - \boldsymbol{F}_t^d - \boldsymbol{F}_t^0 + \boldsymbol{d} = \boldsymbol{0} \tag{6.2}$$

where $\boldsymbol{d} \in \mathbb{R}^{3n\times 1}$ is the total disturbance.

6.3. Design of Element Outer Loop Control

To mitigate both internal and external disturbances, the robust sliding mode control is employed by the outer loop controller to generate a reference trajectory $\boldsymbol{X}_{t,j}^r$. Let the sliding surface of the jth element as

$$\boldsymbol{s}_j = \dot{\boldsymbol{e}}_j + \lambda_j \boldsymbol{e}_j \tag{6.3}$$

$$\boldsymbol{e}_j = \boldsymbol{X}_j^d - \boldsymbol{X}_{t,j} \tag{6.4}$$

where $\boldsymbol{X}_j^d$ is the desired trajectory, $\boldsymbol{e}_j$ is the tracking error, and λ_j is a positive tuning parameter to ensure stability in Chapter 6.

Then, the time derivative of $\boldsymbol{s}_j$ is

$$\dot{\boldsymbol{s}}_j = \ddot{\boldsymbol{e}}_j + \lambda_j \dot{\boldsymbol{e}}_j \tag{6.5}$$

Using $\dot{\boldsymbol{s}}_j = -K_j^s \mathbf{I}_{6\times 6} sign\left(\boldsymbol{s}_j\right)$ for robustness leads to

$$\ddot{\boldsymbol{e}}_j + \lambda_j \dot{\boldsymbol{e}}_j = -K_j^s sign\left(\boldsymbol{s}_j\right) \tag{6.6}$$

where K_j^s is the switching gain and $\mathbf{I}_{6\times 6} \in \mathbb{R}^{6\times 6}$ is an identity matrix.

Substituting $\ddot{\boldsymbol{e}}_j = \ddot{\boldsymbol{X}}_j^d - \ddot{\boldsymbol{X}}_{t,j}$ into Eq. (6.6) yields

$$\ddot{\boldsymbol{X}}_{t,j} = \ddot{\boldsymbol{X}}_j^d + \lambda_j\left(\dot{\boldsymbol{X}}_j^d - \dot{\boldsymbol{X}}_{t,j}\right) + K_j^s sign\left(\boldsymbol{s}_j\right) \tag{6.7}$$

Replacing $\ddot{\boldsymbol{X}}_{t,j}$ with the reference acceleration $\ddot{\boldsymbol{X}}_j^r$ yields

$$\ddot{\boldsymbol{X}}_j^r = \ddot{\boldsymbol{X}}_{t,j}^d + \lambda_j \dot{\boldsymbol{e}}_j + K_i^s sign\left(\boldsymbol{s}_i\right) \tag{6.8}$$

Remark 1: The switching gain K_j^s must be carefully chosen to ensure the stability of the outer loop control in the presence of disturbances.

Define a Lyapunov function candidate as

$$V_j = \frac{1}{2}\boldsymbol{s}_j^{\mathrm{T}}\boldsymbol{s}_j \tag{6.9}$$

Differentiating Eq. (6.9) with respect to the time yields

$$\begin{aligned} \dot{V}_j &= \boldsymbol{s}_j{}^{\mathrm{T}}\dot{\boldsymbol{s}}_j = \boldsymbol{s}_j{}^{\mathrm{T}}\left(\ddot{\boldsymbol{e}}_j + \lambda_j\dot{\boldsymbol{e}}_j + \boldsymbol{d}_j\right) \\ &= \boldsymbol{s}_j{}^{\mathrm{T}}\left(-K_j^s sign\left(\boldsymbol{s}_j\right) + \boldsymbol{d}_j\right) \le \left\|\boldsymbol{s}_j\right\|_1\left(-K_j^s + \left\|\boldsymbol{d}_j\right\|_\infty\right) \end{aligned} \tag{6.10}$$

Obviously, the selection of the switching gain $K_j^s > \left\|\boldsymbol{d}_j\right\|$ will ensure

$$\dot{V}_j \le \left\|\boldsymbol{s}_j\right\|_1\left(-K_j^s + \left\|\boldsymbol{d}_j\right\|_\infty\right) < 0 \tag{6.11}$$

Thus, the outer loop control of the jth becomes robustly stable if $K_j^s > \left\|\boldsymbol{d}_j\right\|$.

6.4. Design of Element Inner Loop Control

The inner loop controller tracks the reference trajectory for the jth element. Since the element strain $\boldsymbol{\varepsilon}_{t,j}^M$ is measured by the fiber optic strain sensor, the element dynamic equation in Eq. (4.8) can be rewritten as

$$\boldsymbol{M}_{t,j}\ddot{\boldsymbol{X}}_{t,j} + \boldsymbol{C}_{t,j}\dot{\boldsymbol{X}}_{t,j} = \boldsymbol{F}_{t,j}^g + \boldsymbol{F}_{t,j}^d + \boldsymbol{F}_{t,j}^e(\boldsymbol{\varepsilon}_{t,j}^M) + \boldsymbol{u}_{t,j} \tag{6.12}$$

However, the equivalent elastic force can be represented by the strain function,

$$\boldsymbol{F}_{t,j}^{e}(\boldsymbol{\varepsilon}_{t,j}^{M}) = \boldsymbol{F}_{t,j}^{k} - \boldsymbol{K}_{t,j}\boldsymbol{X}_{t,j} \tag{6.13}$$

Substituting Eqs. (3.6) into Eq. (6.13) yields

$$\begin{aligned}\boldsymbol{F}_{t,j}^{e}(\boldsymbol{\varepsilon}_{t,j}^{M}) &= E_t A_{t,j} L_{t,j} \boldsymbol{B}_{t,j}^{\mathrm{T}} - E_t A_{t,j} L_{t,j} \boldsymbol{B}_{t,j}^{\mathrm{T}} \boldsymbol{B}_{t,j} \boldsymbol{X}_{t,j} \\ &= -E_t A_{t,j} L_{t,j} \boldsymbol{B}_{t,j}^{\mathrm{T}} \left(\boldsymbol{B}_{t,j} \boldsymbol{X}_{t,j} - 1 \right)\end{aligned} \tag{6.14}$$

The Green-Lagrange strain is defined as

$$\varepsilon_{t,j}^{M} = \frac{L_j - L_{0,j}}{L_{0,j}} = \boldsymbol{B}_{t,j}\boldsymbol{X}_{t,j} - 1 \tag{6.15}$$

Then, the equivalent elastic force $\boldsymbol{F}_{t,j}^{e}(\boldsymbol{\varepsilon}_{t,j}^{M})$ can be reformulated by substituting Eq. (6.15) to Eq. (6.14), such that,

$$\boldsymbol{F}_{t,j}^{e}(\varepsilon_{t,j}^{M}) = -E_t A_{0,j} L_{0,j} \boldsymbol{B}_{t,j}^{\mathrm{T}} \varepsilon_{t,j}^{M} \tag{6.16}$$

Thus, the element inner loop controller can be defined as

$$\boldsymbol{u}_{t,j} = \boldsymbol{M}_{t,j} \left(\ddot{\boldsymbol{X}}_j^{r} + \boldsymbol{K}_j^{p} \boldsymbol{e}_j + \boldsymbol{K}_j^{d} \dot{\boldsymbol{e}}_j \right) + \boldsymbol{C}_{t,j} \dot{\boldsymbol{X}}_j^{d} + \boldsymbol{f}_{t,j} \tag{6.17}$$

$$\boldsymbol{f}_{t,j} = -\boldsymbol{F}_{t,j}^{g} - \boldsymbol{F}_{t,j}^{d} - \boldsymbol{F}_{t,j}^{e}(\varepsilon_{t,j}^{M}) \tag{6.18}$$

where ($\boldsymbol{K}_j^{p}$, $\boldsymbol{K}_j^{d}$) are positive definite diagonal constant matrices.

Remark 2: The controller in Eq. (6.17) has a Proportional-Derivative (PD) structure given by $\boldsymbol{K}_j^{p}\boldsymbol{e}_j + \boldsymbol{K}_j^{d}\dot{\boldsymbol{e}}_j$. Furthermore, the compensation term $\boldsymbol{f}_{t,j}$ is integrated to improve the control performance.

Substituting Eq. (6.17) into Eq. (6.12) yields the error dynamic equation of the jth

element as

$$\ddot{\boldsymbol{e}}_j + \left(\boldsymbol{K}_j^d + \boldsymbol{C}_{t,j}\right)\dot{\boldsymbol{e}}_j + \boldsymbol{K}_j^p \boldsymbol{e}_j = \boldsymbol{0} \tag{6.19}$$

which guarantees exponential convergence of the tracking error $\boldsymbol{e}_j$ to zero. The stability of the element system can be proved easily.

Substituting the reference trajectory in Eq. (6.8) and trajectory error in Eq. (6.4) into Eq. (6.17) yields the designed dual-loop controller for the jth element as

$$\boldsymbol{u}_{t,j} = \boldsymbol{M}_{t,j}\left(\ddot{\boldsymbol{X}}_j^d + \lambda_j \dot{\boldsymbol{e}}_j + K_j^s sign\left(\boldsymbol{s}_j\right) + \boldsymbol{K}_j^p \boldsymbol{e}_j + \boldsymbol{K}_j^d \dot{\boldsymbol{e}}_j\right) + \boldsymbol{C}_{t,j}\dot{\boldsymbol{X}}_j^d - \boldsymbol{F}_{t,j}^g - \boldsymbol{F}_{t,j}^d - \boldsymbol{F}_i^e(\varepsilon_{t,j}^M) \tag{6.20}$$

Therefore, the dynamic equations of the jth element with control input are reconstructed as

$$\begin{cases} \boldsymbol{M}_{t,j}\ddot{\boldsymbol{X}}_{t,j} + \boldsymbol{C}_{t,j}\dot{\boldsymbol{X}}_{t,j} + \boldsymbol{K}_{t,j}\boldsymbol{X}_{t,j} - \boldsymbol{F}_{t,j}^k = \boldsymbol{u}_{t,j} + \boldsymbol{F}_{t,j}^g + \boldsymbol{F}_{t,j}^d + \boldsymbol{d}_j \\ \boldsymbol{u}_{t,j} = \boldsymbol{M}_{t,j}\left(\ddot{\boldsymbol{X}}_j^d + \lambda_j \dot{\boldsymbol{e}}_j + K_j^s sign\left(\boldsymbol{s}_j\right) + \boldsymbol{K}_j^p \boldsymbol{e}_j + \boldsymbol{K}_j^d \dot{\boldsymbol{e}}_j\right) + \boldsymbol{C}_{t,j}\dot{\boldsymbol{X}}_j^d - \boldsymbol{F}_{t,j}^g - \boldsymbol{F}_{t,j}^d - \boldsymbol{F}_{t,j}^e(\varepsilon_{t,j}^M) \end{cases} \tag{6.21}$$

Note that the proposed element-level control laws cannot be applied in isolation, because the nodal states and inter-element interaction forces, or compensation term $\boldsymbol{f}_{t,j}$, are unknown. Instead, they must be assembled element by element to form a global control law and must be solved simultaneously at the global system level. This is like FEM where equations of the model of an element cannot be solved in isolation and must be assembled into a global system equation and solved simultaneously.

Assembling dynamic equations from all elements yields the global dynamics

$$\begin{cases} \boldsymbol{M}_t\ddot{\boldsymbol{X}}_t + \boldsymbol{C}_t\dot{\boldsymbol{X}}_t + \boldsymbol{K}_t\boldsymbol{X}_t - \boldsymbol{F}_t^k = \boldsymbol{B}_t^d\boldsymbol{u}_t + \boldsymbol{F}_t^g + \boldsymbol{F}_t^d + \boldsymbol{d} \\ \boldsymbol{u}_t = \boldsymbol{M}_t\left(\ddot{\boldsymbol{X}}_t^d + \lambda\dot{\boldsymbol{e}} + K^s sign(\boldsymbol{s}) + \boldsymbol{K}^p\boldsymbol{e} + \boldsymbol{K}^d\dot{\boldsymbol{e}}\right) + \boldsymbol{C}_t\dot{\boldsymbol{X}}_t^d - \boldsymbol{F}_t^g - \boldsymbol{F}_t^d - \boldsymbol{F}_t^e(\boldsymbol{\varepsilon}_t^M) \\ \boldsymbol{e} = \boldsymbol{X}_t^d - \boldsymbol{X}_t \\ \boldsymbol{s} = \dot{\boldsymbol{e}} + \lambda\boldsymbol{e} \\ \|\boldsymbol{d}\|_\infty \le D \end{cases} \tag{6.22}$$

where $\boldsymbol{\varepsilon}_t^M$ and $\boldsymbol{F}_t^e$ are the nodal strain and tension vectors along the tether, respectively, $\lambda = \max(\lambda_j)$ is the tuning parameter, $K^s = \max\left(K_j^s\right)$ is the switch gain, D is a positive constant, $\left(\boldsymbol{K}^p, \boldsymbol{K}^d\right) \in \mathbb{R}^{3n\times 3n}$ are the assembled global gain matrices, $\boldsymbol{u}_t \in \mathbb{R}^{3n\times 1}$ is the assembled global control input to the tether system, and $\boldsymbol{B}_t^d \in \mathbb{R}^{3n\times 3n}$ is the mapping matrix from the control input to the state

$$\boldsymbol{B}_t^d = diag(\boldsymbol{b}_1, \boldsymbol{b}_2, ..., \boldsymbol{b}_n) \tag{6.23}$$

$$\boldsymbol{b}_j = \begin{cases} \mathbf{1}_{1*3}, & actuated \\ \mathbf{0}_{1*3}, & non-actuated \end{cases}, \quad (j = 1, 2, \ldots, n) \tag{6.24}$$

Equation (6.22) indicates that the total control input at a node is the superposition of contributions from all adjacent elements sharing that node. For example, if a shared node *j* connects elements *j* and (*j*+1), the total control input at node *j* depends on the states within these two elements, as well as on the inter-element interaction forces between them and their respective neighboring elements.

Furthermore, it is worth pointing out that the element-level control input in Eq. (6.17) includes two parts: (i) a direct control input generated by the element controller based on

local state information within the element, and (ii) an indirect control input transmitted through internal interaction forces between connected elements, which depend on state information from neighboring elements. Therefore, even in the absence of a local actuator, i.e., $\boldsymbol{g} = 0$ in Eq. (6.24), the control effect persists through internal force transmission, and the error dynamics in Eq. (6.19) remains controlled. This element-level controller formulation effectively captures the flexible dynamics of the system, including higher-order vibration modes that are typically unobservable to rigid-body controllers. Moreover, it significantly simplifies controller design by adopting a standardized FEM-based framework, which enables systematic and automated controller synthesis. The overall concept of the proposed framework is illustrated in Figure 6-3.

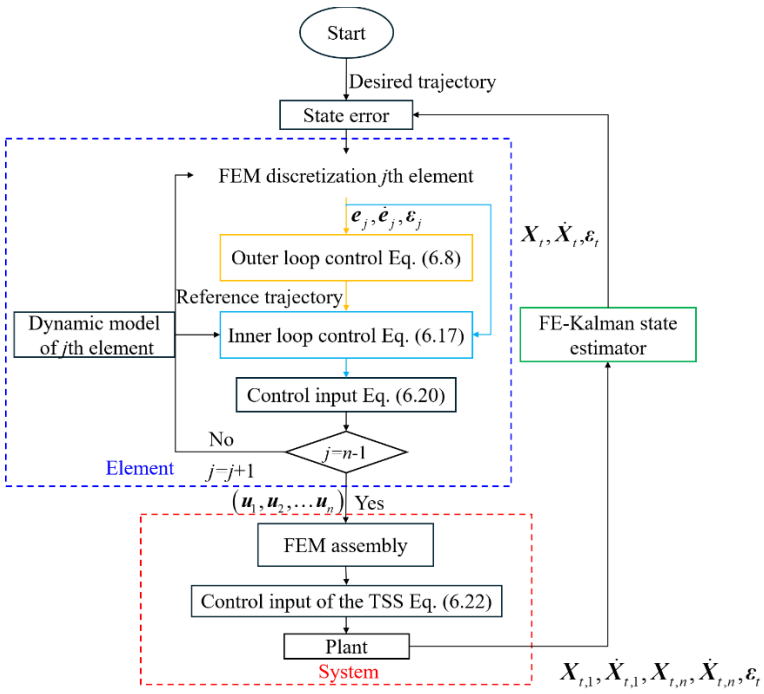

Figure 6-3 Schematic of computational control framework.

6.5. Controllability Analysis

Reformulate the dynamic system model in Eq. (6.22) in the state space form, such that,

$$\dot{\tilde{\boldsymbol{X}}} = \boldsymbol{A}_d \tilde{\boldsymbol{X}} + \boldsymbol{B}_d \boldsymbol{u}_d \tag{6.25}$$

where $\tilde{\boldsymbol{X}} = \left[\boldsymbol{X}_t^{\mathrm{T}}, \dot{\boldsymbol{X}}_t^{\mathrm{T}} \right]^{\mathrm{T}} \in \mathbb{R}^{6n\times 1}$ is the state. The expression of $\boldsymbol{A_d}$ and $\boldsymbol{B_d}$ can be written as

$$\boldsymbol{A}_d = \begin{bmatrix} \boldsymbol{0} & \mathbf{I}_{3n\times 3n} \\ -\boldsymbol{M}_t^{-1}\boldsymbol{K}_t & -\boldsymbol{M}_t^{-1}\boldsymbol{C}_t \end{bmatrix} \in \mathbb{R}^{6n\times 6n} \text{ and } \boldsymbol{B}_d = \begin{bmatrix} \mathbf{0} \\ \boldsymbol{M}_t^{-1}\boldsymbol{B}_t^d \end{bmatrix} \in \mathbb{R}^{6n\times 3n} \tag{6.26}$$

The controllability of the system can be proved using the Popov-Belevitch-Hautus (PBH) test, as described on page 133 of Ref. [58,119–121]. According to this test, the model is controllable if and only if the PBH matrix has full column rank for all eigenvalues $\lambda_e \in \mathbf{R}$ of the system, such that,

$$\text{PBH} = \left[\lambda_e \mathbf{I}_{3n\times 3n} - \boldsymbol{A}_d \quad \boldsymbol{B}_d \right] \in \mathbb{R}^{6n\times 9n} = 6n \tag{6.27}$$

Previous studies on space tethers or cables have established that their vibrations are controllable when the system boundaries are fixed [122]. Rank-deficiency arises only in the free-free configuration, where both tether ends are unconstrained and the system exhibits rigid-body motion. This implies that the internal submatrix $\left(\lambda_e \mathbf{I}_{3n\times 3n} - \boldsymbol{A}\right)_{in} \in \mathbb{R}^{(6n-6)\times(6n-6)}$, excluding the elements related to the end-point positions or rigid-body modes, remain full rank. Moreover, in the matrix $\boldsymbol{M}_t^{-1}\boldsymbol{B}_t^d$, non-zero entries appear only in the diagonal elements corresponding to the end-point coordinates. Under these conditions, the PBH matrix remains full column rank, thereby proving the

controllability of the system in Eq. (6.22).

6.6. Stability and Robustness Analysis

***Theorem* 1**: Considering the space tether in Eq. (6.22), the controller is designed at the individual element level and assembled to form a global system controller. If the parameters λ, K^s, $\boldsymbol{K}^p$ and $\boldsymbol{K}^d$ are strictly positive definite, and the disturbance $\boldsymbol{d}$ is bounded, the assembled system controller is input-to-state stable at the desired trajectory, i.e., $\boldsymbol{X}_t \to \boldsymbol{X}_t^d$ as $\boldsymbol{t} \to \infty$.

Proof:

Given that the space tether is actuated only at two tether endpoints by thrusters on tethered spacecraft, the mapping matrix is defined as $\boldsymbol{B}_t^d = diag(\mathbf{1}_{1*3}, \mathbf{0}_{1*3}, ..., \mathbf{0}_{1*3}, \mathbf{1}_{1*3})$ and is semi-positive definite.

Define a Lyapunov function candidate as

$$
\begin{aligned}
V &= V_1 + V_2 \\
V_1 &= \frac{1}{2}\boldsymbol{e}^{\mathrm{T}}\boldsymbol{K}_t\left(\mathbf{I}_{3n\times 3n} - \boldsymbol{B}_t^d\right)\boldsymbol{e} + \frac{1}{2}\dot{\boldsymbol{e}}^{\mathrm{T}}\boldsymbol{M}_t\left(\mathbf{I}_{3n\times 3n} - \boldsymbol{B}_t^d\right)\dot{\boldsymbol{e}} \\
V_2 &= \frac{1}{2}\boldsymbol{s}^{\mathrm{T}}\boldsymbol{B}_t^d\boldsymbol{s} + \frac{1}{2}\boldsymbol{e}^{\mathrm{T}}\boldsymbol{B}_t^d(\boldsymbol{K}^p + \lambda\boldsymbol{K}^d + \lambda\boldsymbol{M}_t^{-1}\boldsymbol{C}_t)\boldsymbol{e}
\end{aligned}
\tag{6.28}
$$

where the coefficient matrices ($\boldsymbol{K}_t$, $\boldsymbol{M}_t$) are positive definite matrices.

The time derivative of the V is derived as

$$
\begin{aligned}
&\dot{V} = \dot{V}_1 + \dot{V}_2 \\
&\dot{V}_1 = \boldsymbol{e}^{\mathrm{T}} \boldsymbol{K}_t \left(\mathbf{I}_{3n\times 3n} - \boldsymbol{B}_t^d \right) \dot{\boldsymbol{e}} + \dot{\boldsymbol{e}}^{\mathrm{T}} \boldsymbol{M}_t \left(\mathbf{I}_{3n\times 3n} - \boldsymbol{B}_t^d \right) \ddot{\boldsymbol{e}} \\
&\dot{V}_2 = \boldsymbol{s}^{\mathrm{T}} \boldsymbol{B}_t^d \dot{\boldsymbol{s}} + \boldsymbol{e}^{\mathrm{T}} \boldsymbol{B}_t^d (\boldsymbol{K}^p + \lambda \boldsymbol{K}^d + \lambda \boldsymbol{M}_t^{-1} \boldsymbol{C}_t) \dot{\boldsymbol{e}}
\end{aligned}
\tag{6.29}
$$

According to Eq. (6.22), $\dot{V}$ can be derived as

$$
\begin{aligned}
&\dot{V} = \dot{V}_1 + \dot{V}_2 \\
&\dot{V}_1 = \dot{\boldsymbol{e}}^{\mathrm{T}} \left(\mathbf{I}_{3n\times 3n} - \boldsymbol{B}_t^d \right) \left(\boldsymbol{F}_t^g + \boldsymbol{F}_t^d - \boldsymbol{M}_t \ddot{\boldsymbol{X}}_d - \boldsymbol{C}_t \dot{\boldsymbol{e}} + \boldsymbol{d} \right) \\
&\dot{V}_2 = \left(\dot{\boldsymbol{e}} + \lambda \boldsymbol{e} \right)^{\mathrm{T}} \boldsymbol{B}_t^d \left(\ddot{\boldsymbol{e}} + \lambda \dot{\boldsymbol{e}} \right) + \boldsymbol{e}^{\mathrm{T}} \boldsymbol{B}_t^d (\boldsymbol{K}^p + \lambda \boldsymbol{K}^d + \lambda \boldsymbol{M}_t^{-1} \boldsymbol{C}_t) \dot{\boldsymbol{e}} \\
&= \left(\dot{\boldsymbol{e}} + \lambda \boldsymbol{e} \right)^{\mathrm{T}} \boldsymbol{B}_t^d \left(-\boldsymbol{K}^p \boldsymbol{e} - \boldsymbol{K}^d \dot{\boldsymbol{e}} - \lambda \dot{\boldsymbol{e}} - K^s \mathrm{sign}\left(\boldsymbol{s} \right) + \boldsymbol{d} + \lambda \dot{\boldsymbol{e}} - \boldsymbol{M}_t^{-1} \boldsymbol{C}_t \dot{\boldsymbol{e}} \right) + \boldsymbol{e}^{\mathrm{T}} \boldsymbol{B}_t^d (\boldsymbol{K}^p + \lambda \boldsymbol{K}^d + \lambda \boldsymbol{M}_t^{-1} \boldsymbol{C}_t) \dot{\boldsymbol{e}} \\
&= -\dot{\boldsymbol{e}}^{\mathrm{T}} \boldsymbol{B}_t^d \boldsymbol{K}^d \dot{\boldsymbol{e}} - \lambda \boldsymbol{e}^{\mathrm{T}} \boldsymbol{B}_t^d \boldsymbol{K}^p \boldsymbol{e} - \dot{\boldsymbol{e}}^{\mathrm{T}} \boldsymbol{B}_t^d \boldsymbol{M}_t^{-1} \boldsymbol{C}_t \dot{\boldsymbol{e}} + \boldsymbol{s}^{\mathrm{T}} \boldsymbol{B}_t^d \left(-K^s \mathrm{sign}\left(\boldsymbol{s} \right) + \boldsymbol{d} \right)
\end{aligned}
\tag{6.30}
$$

Since the control objective of the space tether is to stay in the designed Earth orbit, and the mass of the tether is much smaller than that of the main spacecraft 28, it is reasonable to assume that there exists the relationship,

$$
\left\| \left(\mathbf{I}_{3n\times 3n} - \boldsymbol{B}_t^d \right) \left(\boldsymbol{F}_t^g + \boldsymbol{F}_t^d - \boldsymbol{M}_t \ddot{\boldsymbol{X}}_t^d \right) \right\|_\infty \ll \left\| \boldsymbol{d} \right\|_\infty \tag{6.31}
$$

With Young's inequality, the derivative of the Lyapunov function can be further expressed as

$$
\begin{aligned}
&\dot{V} = \dot{V}_1 + \dot{V}_2 \\
&\dot{V}_1 = \dot{\boldsymbol{e}}^{\mathrm{T}} \left(\mathbf{I}_{3n\times 3n} - \boldsymbol{B}_t^d \right) \boldsymbol{d} - \dot{\boldsymbol{e}}^{\mathrm{T}} \boldsymbol{M}_t^{-1} \boldsymbol{C}_t \dot{\boldsymbol{e}} \le -\dot{\boldsymbol{e}}^{\mathrm{T}} \left(\mathbf{I}_{3n\times 3n} - \boldsymbol{B}_t^d \right) (\boldsymbol{M}_t^{-1} \boldsymbol{C}_t - \frac{1}{2\varsigma} \mathbf{I}_{3n\times 3n}) \dot{\boldsymbol{e}} + \frac{1}{2} \varsigma D^2 \\
&\dot{V}_2 = -\dot{\boldsymbol{e}}^{\mathrm{T}} \boldsymbol{B}_t^d \boldsymbol{K}^d \dot{\boldsymbol{e}} - \lambda \boldsymbol{e}^{\mathrm{T}} \boldsymbol{B}_t^d \boldsymbol{K}^p \boldsymbol{e} - \dot{\boldsymbol{e}}^{\mathrm{T}} \boldsymbol{B}_t^d \boldsymbol{M}_t^{-1} \boldsymbol{C}_t \dot{\boldsymbol{e}} + \left\| \boldsymbol{B}_t^d \boldsymbol{s} \right\|_1 \left(-K^s + D \right) \le 0
\end{aligned}
\tag{6.32}
$$

If the disturbance is absent, the derivative of the Lyapunov function can be simplified

as

$$\dot{V} = -\dot{\boldsymbol{e}}^{\mathrm{T}} \boldsymbol{M}_t^{-1} \boldsymbol{C}_t \dot{\boldsymbol{e}} - \dot{\boldsymbol{e}}^{\mathrm{T}} \boldsymbol{B}_t^d \boldsymbol{K}^d \dot{\boldsymbol{e}} - \lambda \boldsymbol{e}^{\mathrm{T}} \boldsymbol{B}_t^d \boldsymbol{K}^p \boldsymbol{e} - K^s \left\| \boldsymbol{B}_t^d \boldsymbol{s} \right\|_1 \leq 0 \tag{6.33}$$

Equation (6.33) shows clearly that $\dot{V} = 0$ only if $\dot{\boldsymbol{e}} = \boldsymbol{0}$ and $\boldsymbol{B}_t^d \boldsymbol{e} = \boldsymbol{0}$. Given that V is positive definite and radially unbounded, it is concluded that the error will converge to the invariant set $S = \left\{ \boldsymbol{e}, \dot{\boldsymbol{e}} \,|\, \dot{V} = 0 \right\}$.

Substituting $\dot{\boldsymbol{e}} = \boldsymbol{0}$ and $\boldsymbol{B}_t^d \boldsymbol{e} = \boldsymbol{0}$ into the dynamic equation in Eq. (6.2) yields ,

$$\left(\mathbf{I}_{3n \times 3n} - \boldsymbol{B}_t^d \right) \boldsymbol{K}_t \boldsymbol{e} = \boldsymbol{0} \tag{6.34}$$

which leads to

$$\left(\mathbf{I}_{3n \times 3n} - \boldsymbol{B}_t^d \right) \boldsymbol{e} = \boldsymbol{0} \tag{6.35}$$

Thus, it is proved that the only point in the invariant set S is the origin $\left(\boldsymbol{e}, \dot{\boldsymbol{e}} \right) = \boldsymbol{0}$. According to LaSalle's invariance principle, all system trajectories asymptotically converge to this invariant set, which ensures that the equilibrium at the origin is globally asymptotically stable.

Now, consider the disturbance is not absent but bounded. By setting $K^s > D$ and $\varsigma = [2\lambda_{\min}(\boldsymbol{M}_t^{-1} \boldsymbol{C}_t)]^{-1}$, the derivative of the Lyapunov function in Eq. (6.32) becomes

$$\dot{V} = -\dot{\boldsymbol{e}}^{\mathrm{T}} \left((\boldsymbol{M}_t^{-1} \boldsymbol{C}_t - \frac{1}{2\varsigma} \mathbf{I}_{3n \times 3n}) + \boldsymbol{B}_t^d \left(\boldsymbol{K}^d + \frac{1}{2\varsigma} \mathbf{I}_{3n \times 3n} \right) \right) \dot{\boldsymbol{e}} - \lambda \boldsymbol{e}^{\mathrm{T}} \boldsymbol{B}_t^d \boldsymbol{K}^p \boldsymbol{e} + \frac{1}{2} \varsigma D^2 \leq 0 \tag{6.36}$$

The above inequality shows that the decrease rate of the Lyapunov function can be

offset by quadratic terms in the disturbances. According to the stability theory [123], the function of the disturbance magnitude ultimately bounds the error as

$$\left\|\boldsymbol{e}(t)\right\| \le \beta\left(\left\|\boldsymbol{e}(0)\right\|, t\right) + \gamma(D) \tag{6.37}$$

Thus, the closed-loop system is stable and robust.

6.7. Simulation and Discussion

The efficacy of the proposed computational control framework is demonstrated by two numerical simulation cases. Table 6-1 lists the tether physical and orbital parameters. In this chapter, based on the convergence analysis in the previous studies [99], the tether can be discretized into four elements, with the masses of the spacecraft lumped at the tether endpoints. To account for both parametric uncertainties in the model and external perturbations, the following disturbance is introduced into the simulation,

$$\begin{aligned}\boldsymbol{d} &= 0.1\boldsymbol{M}_t\ddot{\boldsymbol{e}} + 0.1\boldsymbol{K}_t\boldsymbol{e} + 0.1\boldsymbol{C}_t\dot{\boldsymbol{e}} + \boldsymbol{F}_t^d \\ &\le 0.1\boldsymbol{M}_t\ddot{\boldsymbol{e}}_0 + 0.1\boldsymbol{K}_t\boldsymbol{e}_0 + 0.1\boldsymbol{C}_t\dot{\boldsymbol{e}}_0 + \boldsymbol{F}_t^d\left(\boldsymbol{v}_{\max}\right)\end{aligned}$$

where $(\ddot{\boldsymbol{e}}_0, \dot{\boldsymbol{e}}_0, \boldsymbol{e}_0)$ are the initial errors of state and the condition $\|\boldsymbol{d}\|_\infty \le D$ is assumed to be satisfied. Table 6-1 lists the tether physical and orbital parameters.

Table 6-1 Physical parameters of the TSS

Parameter	Value
Mass of main spacecraft	500 kg
Mass of sub spacecraft	5 kg
Tether length	500 m
Tether cross-section Area	$1.9635\text{x}10^{-7}$ m^2
Tether Density (Aluminum)	2700 kg/m^3

Tether Young's Modulus	72 GPa
Orbital altitude of CM	600 km

The FE-Kalman state estimator is used to estimate the internal node states along the tether for feedback control.

6.7.1 Straightening an Initially Bent Space Tether

The tethered space system moves in the equatorial orbital plane (*O-XY* plane). The control objective is to straighten an initially bent tether to a straight tether in the local vertical, as shown in Figure 6-4. The tether is initially bent into a half-circle shape with both endpoints aligned with the local vertical. To describe its motion, a local coordinate frame o-*xy* in the orbital plane is introduced with the origin fixed at the main spacecraft, the *x*-axis pointing toward the direction opposite to the orbital motion, and the *y*-axis aligned with the local vertical, pointing away from the Earth's center.

The orbital motion of the tether was simulated for 2 hours with the proposed controller. The time step is 0.01s. The parameters λ_j, K_j^s, $\boldsymbol{K}_j^p$ and $\boldsymbol{K}_j^d$ of each element are chosen as

$$\begin{cases} \lambda_j = 100 \\ K_j^s = 10 \\ \boldsymbol{K}_j^p = diag\left(100,100,100,100,100,100\right) \\ \boldsymbol{K}_j^d = diag\left(70,70,70,70,70,70\right) \end{cases}$$

As a comparison, a conventional single-loop SMC strategy derived from ROM and a dual-loop SMC strategy derived from the finite element model at the system level are also employed to show the efficacy and robustness of the proposed computational control

framework, respectively. The corresponding parameters λ_s and K_s^s for the conventional single-loop SMC are chosen as

$$\begin{cases} \lambda_s = 100 \\ K_s^s = 10 \end{cases}$$

The corresponding parameters λ, K^s, $\boldsymbol{K}^p$ and $\boldsymbol{K}^d$ for the dual-loop SMC strategy at the system level are chosen as

$$\begin{cases} \lambda_s = 100 \\ K_s^s = 10 \\ \boldsymbol{K}_s^p = diag\left(100,100,100,100,100,100\right) \\ \boldsymbol{K}_s^d = diag\left(70,70,70,70,70,70\right) \end{cases}$$

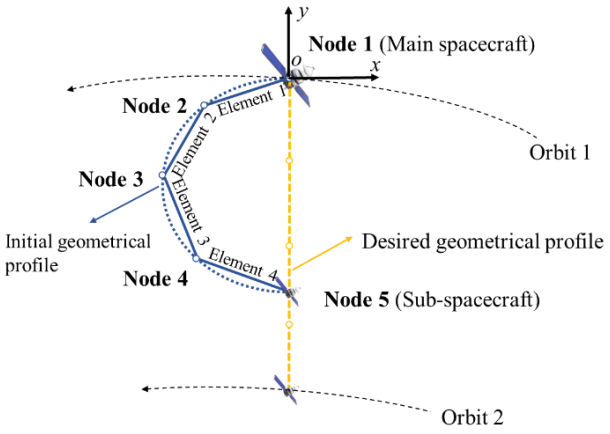

Figure 6-4 Initial and desired tether geometric configurations.

The simulation results are shown in Figure 6-5-Figure 6-10. The tether geometric profile at different time instants, with and without control, is shown in Figure 6-5. With the proposed controller, the space tether becomes straight in the local vertical within approximately 800s. In contrast, without control, the tether continues to exhibit libration.

The results indicate that the proposed computational controller surpasses two conventional strategies, thereby validating a standardized, modular, and effective control design framework for space tethers. Additionally, compared with the global computational control results shown in Figure 5-8, the co-located control achieves better suppression of tether oscillations, even in the presence of disturbances. This improved performance is attributed to the element-level controller with strain-dependent dynamic compensation, which damps the propagation of internal high-frequency modal waves within each element. In contrast, the global control approach cannot effectively attenuate these internal modes because its control law is primarily designed to regulate the overall system behavior.

The relative position errors of the two spacecraft and the midpoint of the tether (Node 3) are shown in Figure 6-6–Figure 6-8. As shown in Figure 6-6 and Figure 6-7, despite external disturbances, both spacecraft rapidly reach the desired orbital altitudes under the proposed computational control and two conventional strategies, whereas the uncontrolled tether does not. Figure 6-8 further shows that the proposed control enables rapid convergence of the tether's midpoint to the desired straight-line configuration with minimal tracking error. In contrast, the strategies derived from the ROM (SMC_ROM) and the full system model (SMC_FEM) yield significantly larger errors. This occurs because the ROM-based controller oversimplifies the tether's elastic dynamics, lacking the fidelity of the element-level design. Furthermore, the SMC_FEM fails to leverage the local interactions within adjacent elements to effectively propagate control actions from the system boundaries to the internal nodes. In the absence of control, the errors diverge,

demonstrating the system's inherent inability to achieve the required configuration passively. These results validate the effectiveness of the proposed computational control in controlling tether configuration under disturbance.

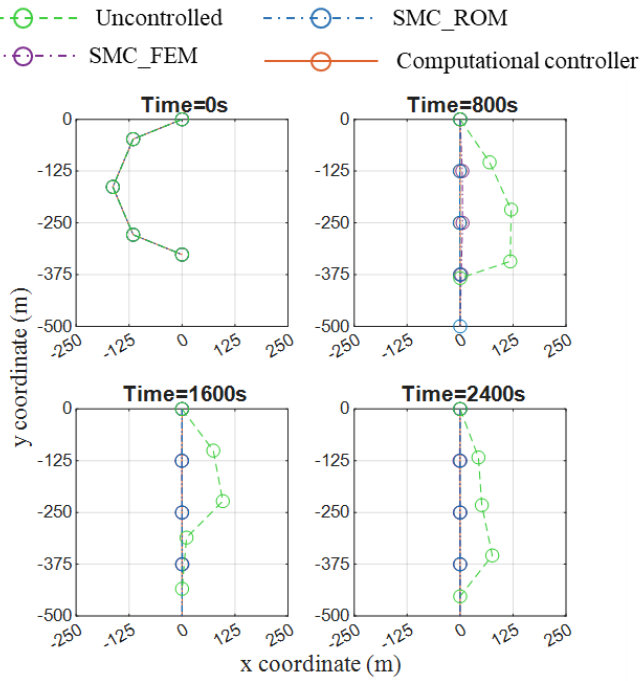

Figure 6-5 Tether configurations at different time instances with and without control input.

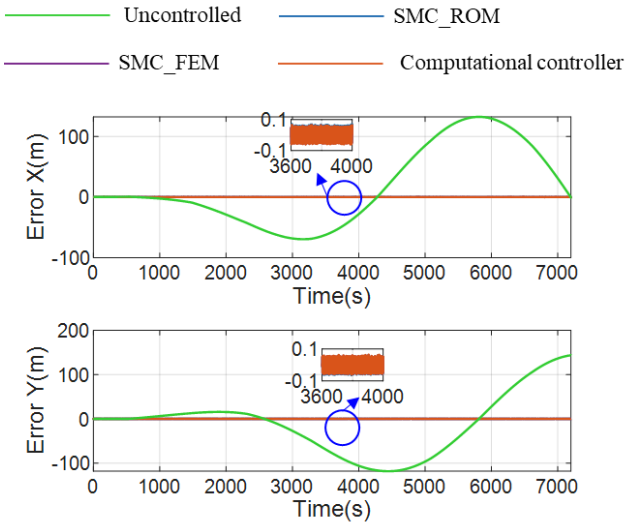

Figure 6-6 Main spacecraft position error in the global frame.

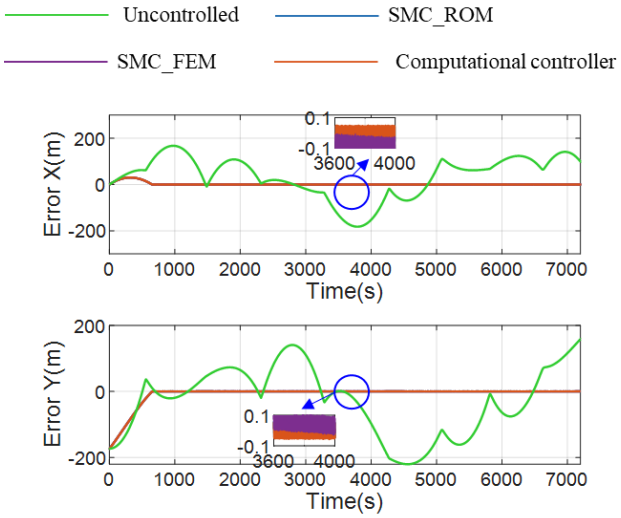

Figure 6-7 Sub spacecraft position error in the global frame.

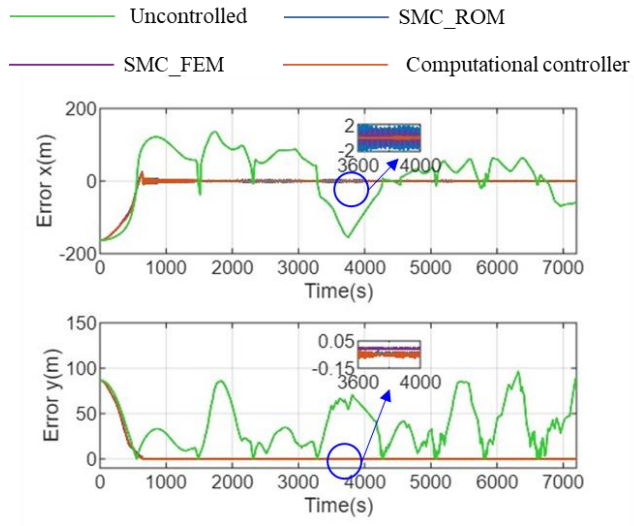

Figure 6-8 Mid-node position error in the local frame.

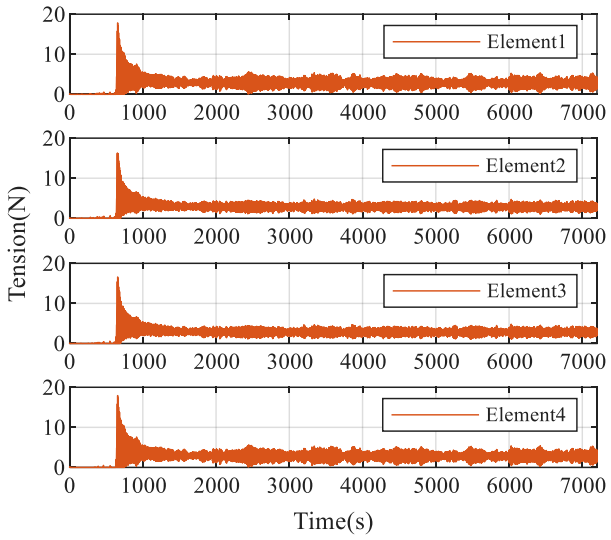

Figure 6-9 Time histories of tether tension in tether elements under computational control.

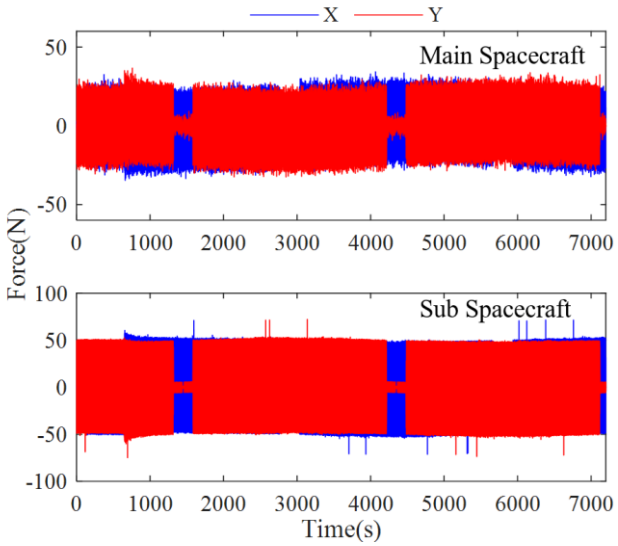

Figure 6-10 Time histories of computational control input at the main spacecraft and sub spacecraft.

Next, Figure 6-9 shows that all tether elements remain taut throughout the control process, satisfy the fundamental no-compression requirement for the tether, and gradually converge stably to a bounded region as the tether approaches the desired straight configuration. Finally, Figure 6-10 shows that the control forces applied to both spacecraft are bounded and periodic, enabling them to maintain their designated orbits despite external disturbances.

6.7.2 Orbit and Attitude Maintenance of Momentum-Exchange Tethers

Momentum-exchange tethers are widely used to deliver payloads to designated locations or transfer them to higher orbits. During tether rotation, releasing the end body imparts momentum to the payload, while the tethered system loses angular momentum,

leading to reduced velocity and a lower orbital altitude. To counteract this effect, the proposed computational control framework is applied to stabilize the tether and maintain its periodic motion following payload release events.

A consistent coordinate frame is used to describe the motion of the tether, aligned with earlier case studies. As illustrated in Figure 6-11, The tethered space system moves in the equatorial orbital plane (*O-XY* plane) and the control objectives are twofold: (1) to maintain a taut and straight tether while maneuvering the sub spacecraft to a higher orbit, and (2) to preserve the overall orbital altitude and self-rotation angular velocity of the tether system. Initially, the tether configuration consists of a straight tether aligned along the local vertical direction, with both endpoints fixed. The system begins with a certain initial self-rotation angular velocity $\omega = 0.0076 rad/s$. The payload is released at t=485.22s, when the sub spacecraft reaches the target orbit.

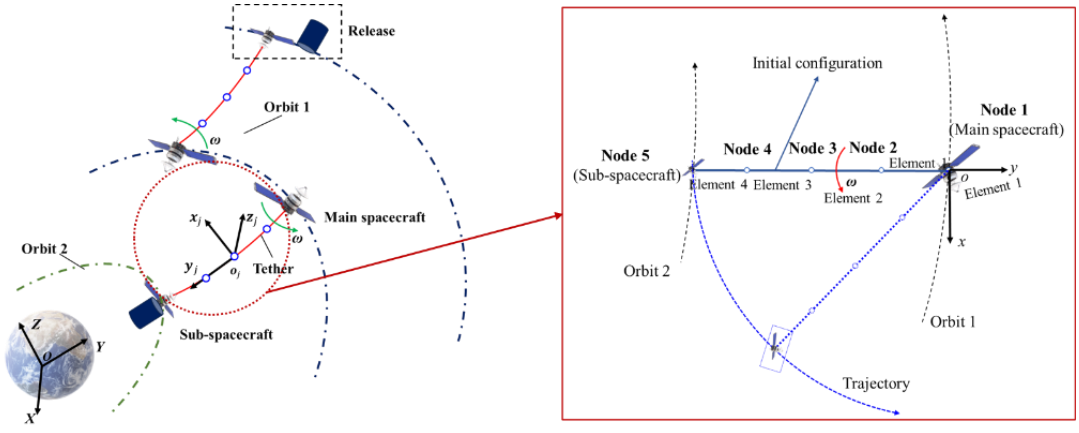

Figure 6-11 Spinning tether geometric configurations.

The orbital motion of the tether was simulated for 2 hours with and without the

proposed control input. The tether is still discretized into 4 elements, and the time step is set to 0.01s. The parameters λ_j, K_j^s, $\boldsymbol{K}_j^p$ and $\boldsymbol{K}_j^d$ for elements are assumed to be the same for all elements and are chosen as

$$\begin{cases} \lambda_j = 100 \\ K_j^s = 10 \\ \boldsymbol{K}_j^p = diag\left(10,10,10,10,10,10\right) \\ \boldsymbol{K}_j^d = diag\left(7,7,7,7,7,7\right) \end{cases}$$

To validate the efficacy and robustness of the proposed computational control framework, a dual-loop SMC strategy derived from the system-level finite element model is utilized as a benchmark. The corresponding parameters λ_s, K_s^s, $\mathbf{K}_s^p$ and $\boldsymbol{K}_s^d$ for the strategy are chosen as

$$\begin{cases} \lambda = 100 \\ K_s^s = 10 \\ \boldsymbol{K}_s^p = diag\left(10,10,10,10,10,10\right) \\ \boldsymbol{K}_s^d = diag\left(7,7,7,7,7,7\right) \end{cases}$$

Figure 6-12 shows the trajectories of the main and sub spacecraft under the proposed computational control. The main spacecraft remains in the predefined orbit, while the sub spacecraft demonstrates periodic orbital motion relative to the main spacecraft and the tether librates accordingly. Figure 6-13 compares the tether geometric configuration at various time instants with and without control. The controlled tether maintains stable orbital motion and self-rotation with significantly suppressed libration. The sub spacecraft reaches the higher orbit, and the tether remains taut and straight after payload release. In

contrast, the uncontrolled tether exhibits persistent tether libration due to its rotational dynamics.

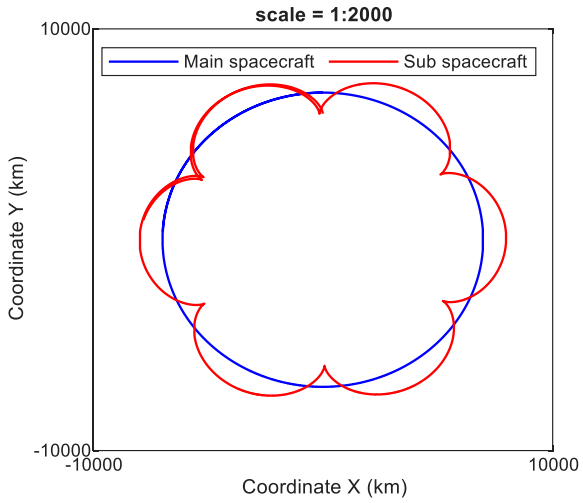

Figure 6-12 The trajectory of tether motion under the computational controller.

In addition, as shown in Figure 6-14–Figure 6-15, the tracking errors of both spacecraft indicate that the proposed control scheme enables the tether to maintain its stable periodic motion and self-rotation, even in the presence of external disturbances. Furthermore, Figure 6-16 demonstrates that, under the proposed controller, the relative position error of the tether midpoint converges toward the straight-line geometric configuration. Instead, in the absence of control, the tether exhibits persistent vibrations that cannot be effectively attenuated by passive damping alone.

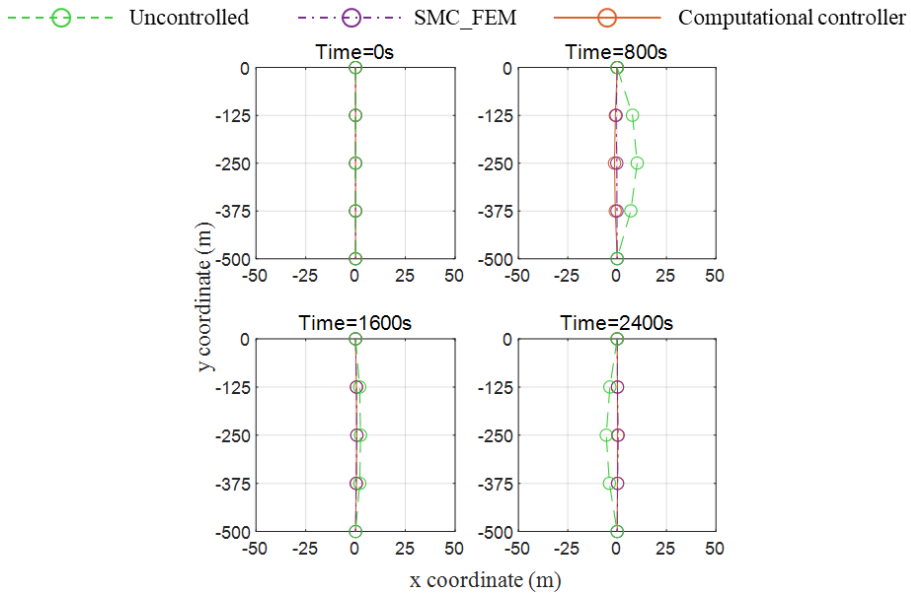

Figure 6-13 Tether configurations at different time instants with and without control.

Additionally, Figure 6-14–Figure 6-16 demonstrate that controllers designed at both the system and element levels successfully maintain stable periodic motion and rotation of the tether, even in the presence of external disturbances. As shown in Figure 6-16, the proposed controller effectively drives the tether midpoint toward the desired straight-line configuration. Notably, the proposed computational framework exhibits the superior performance of vibration suppression compared to the system-level controller (SMC_FEM). Furthermore, the results confirm that without active control, persistent tether libration cannot be suppressed by the system's passive damping alone.

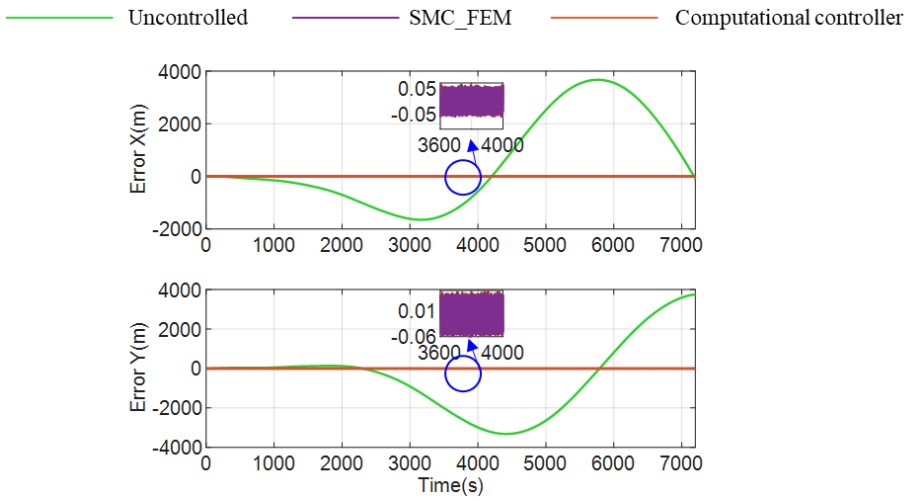

Figure 6-14 Main spacecraft position error in the global frame.

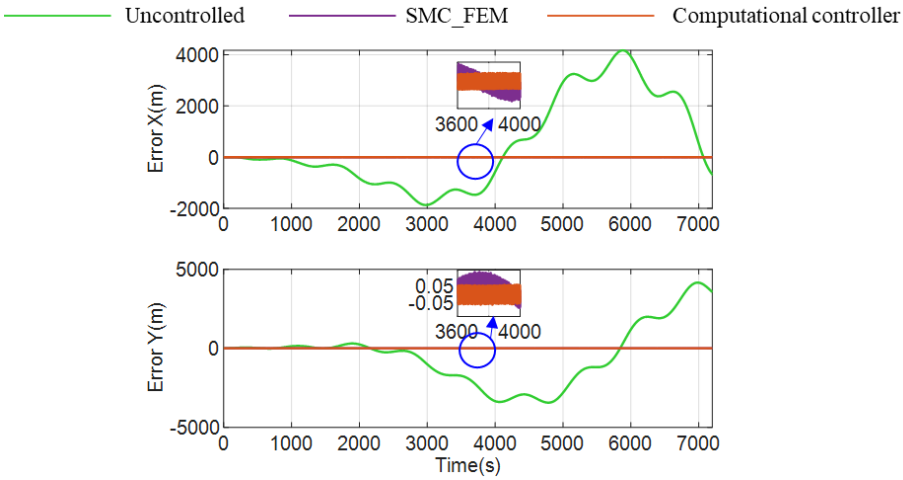

Figure 6-15 Sub spacecraft position error in the global frame.

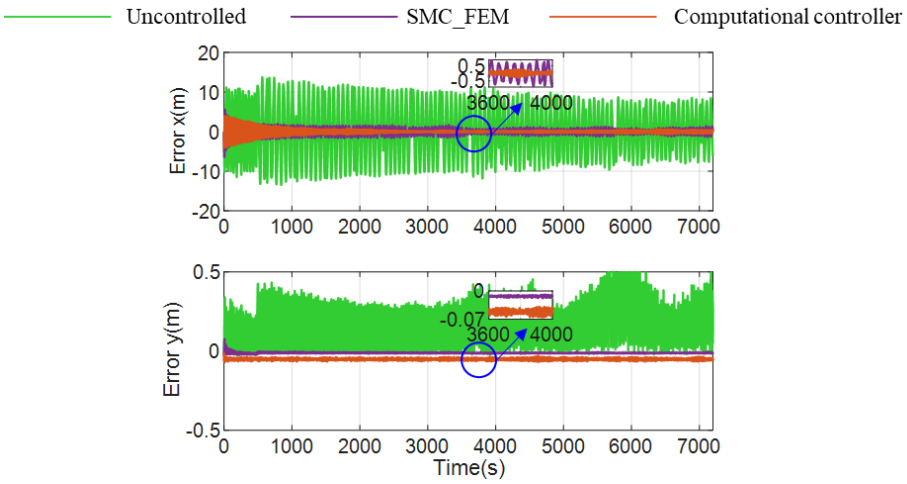

Figure 6-16 Mid-node position error in the local frame.

The time histories of the tether tension in each element and the control input forces applied to drive the tether are shown in Figure 6-17–Figure 6-18, respectively. As illustrated in Figure 6-17, the tether remains taut in all elements throughout the entire maneuver. After the payload is released into a higher orbit, the tension gradually stabilizes at a lower, bounded value. Figure 6-18 shows that the control input forces applied to both spacecraft effectively maintain their stable periodic motion and keep the tether taut and straight despite external disturbances.

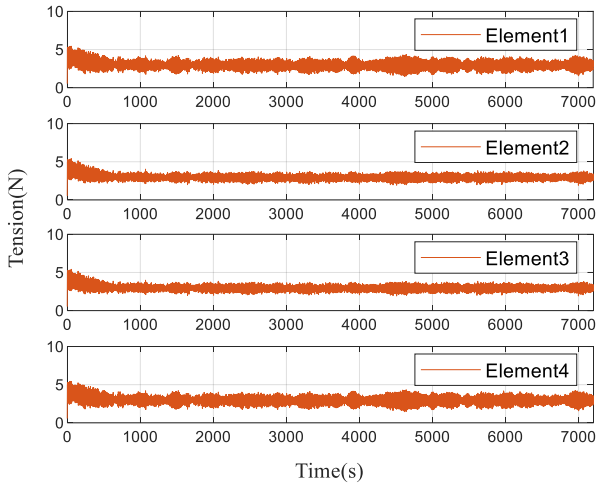

Figure 6-17 Time histories of tether tension of each element.

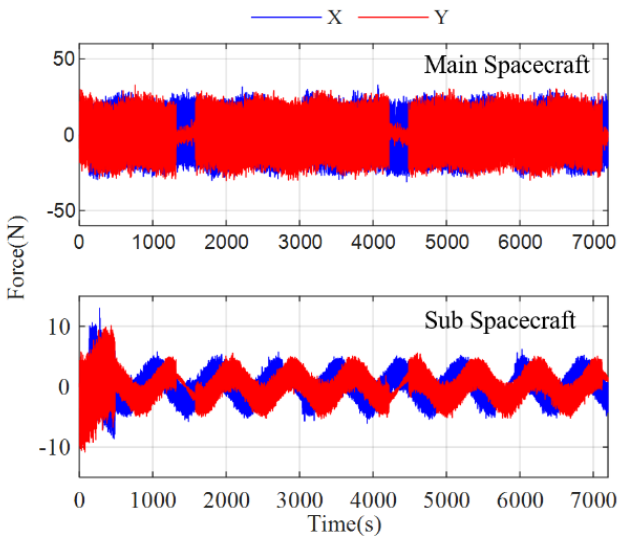

Figure 6-18 Time histories of control input at the main spacecraft and sub spacecraft.

Chapter 7 CONCLUSION AND FUTURE WORK

Summary: This chapter summarizes the main conclusions and contributions of the thesis and presents a brief discussion of future research directions.

7.1. General Conclusion

This dissertation establishes a unified finite-element-based computational framework for the high-fidelity modeling, state estimation, and computational control of TSS with strongly coupled orbital-structural dynamics. The proposed NPFEM provides a physically consistent representation of coupled multibody-elastic behavior, overcomes the limitations of conventional rigid-flexible partitioned approaches, and enables accurate characterization of large rigid-body motion, distributed deformation, tension transmission, and orbit-structure interaction. Building on this foundation, the dissertation develops a hybrid state estimation architecture that integrates position and velocity measurements, fiber optic sensing data, and virtual sensing models within a kinematic-model-based Kalman filtering framework to achieve robust full-state reconstruction of space tethers. It further formulates a computational optimal feedback control strategy for regulating the tether geometric profile by recasting the nonlinear optimal control problem as a TPBVP, thereby generating the control inputs numerically from the canonical equations for closed-loop feedback control via a moving horizon approach. In parallel, a modular computational control framework is introduced for automated controller synthesis directly in the finite

element domain, with Lyapunov-based guarantees of stability and robustness for high-dimensional nonlinear tethered systems. Collectively, these contributions unify modeling, estimation, and control within a common finite element framework, advance the theoretical and computational foundations of tethered space system dynamics, and provide a rigorous and extensible basis for future research on control-actuated tether systems, distributed sensing, contact dynamics, multidisciplinary design optimization, and long-duration mission applications.

7.2. Thesis Contribution

This dissertation focuses on developing a unified, automated framework for dynamic modeling, state estimation, and control design for TSS. The main contributions of this study are summarized as follows.

7.2.1 Unified Elastic Dynamic Model of TSS

The proposed unified position-based finite element framework provides a physically consistent and robust basis for modeling tethered spacecraft systems by treating both spacecraft and tethers within a single elastic formulation. Its main contribution is the ability to accurately resolve strongly coupled orbital-structural dynamics, including large overall motion, elastic deformation, transient effects, tension propagation, and orbit-structure interaction, even in complex multi-spacecraft configurations. Because environmental perturbations are naturally incorporated into the governing equations, their influence on

both structural and orbital behavior can be captured without additional interface-level treatment. The numerical studies show that the framework maintains high fidelity under strongly coupled conditions and, due to its scalable and automation-compatible formulation, offers strong potential for future use in optimization, control, and integrated mission design for advanced tethered space applications.

7.2.2 Robust FE-Kalman State Estimator for Flexible Space Tethers

This dissertation further contributes a unified state estimation framework for flexible space tethers, significantly advancing current capabilities for distributed full-state reconstruction. By integrating position and velocity sensing, fiber optic strain-based reconstruction, and virtual sensing within a common observer formulation, the study enables accurate and robust estimation of internal tether dynamics. Thus, it overcomes a central limitation of existing tether estimation strategies, namely the difficulty of recovering distributed internal states with sufficient fidelity for dynamic applications. The proposed framework not only strengthens the methodological basis for tether state estimation, but also provides an extensible foundation for future developments in sensing, monitoring, and control of advanced tethered space systems.

7.2.3 Global Computational Control Framework for Flexible Space Tethers

This dissertation proposed a computational optimal feedback control framework for underactuated space tethers, where actuation is limited to the tether ends. The framework

combines a high-fidelity finite element model with an FE-Kalman state estimator to achieve accurate and efficient geometric profile regulation. Unlike traditional approaches that often depend on reduced-order approximations and analytically derived control laws, the proposed method works directly with high-fidelity system models, preserving physical detail and modeling accuracy. It also supports automated, algorithm-driven controller design, which makes the approach readily extendable to a broad class of elastic systems. In addition, control inputs are generated through numerical solution procedures rather than fixed closed-form laws, offering greater flexibility and adaptability for complex nonlinear dynamics. Numerical results confirm that the framework can effectively drive the tether toward its desired configuration, thereby establishing an extensible high-fidelity control strategy for advanced tethered space applications.

7.2.4 Co-Located Computational Control for Flexible Space Tether

A modular computational control framework is further developed, enabling controller synthesis for space tethers to be performed directly within the finite element domain in a systematic, algorithmic manner. Rather than relying on a single monolithic controller for the fully discretized system, the proposed approach introduces standardized element-level control laws that are synthesized locally and then assembled over the finite element mesh to generate the overall control law, analogous to finite element assembly in computational mechanics. A central contribution of this framework is that it designs controllers directly on the finite element mesh, thereby preserving the full nonlinear dynamics of the original

system and avoiding the fidelity loss commonly associated with reduced-order control approaches. This capability is especially important for flexible tethered space systems, in which internal deformation, wave propagation, and modal interactions play a fundamental role in the overall response. The framework achieves an end-to-end automated methodology that unifies finite element modeling, dynamic characterization, state estimation, controller synthesis, and controller assembly, thereby reducing reliance on manual gain tuning, ad hoc mode selection, and extensive pre-dynamic analysis. Additionally, building on these advantages, the element-level formulation further advances global computational control by enabling more direct regulation of localized tether dynamics, thereby improving control of internal deformation, high-frequency modal behavior, and wave propagation through strain-dependent dynamic compensation.

7.3. Future work

The following research is summarized as follows to continue and expand the current work.

(i) Improve the computational efficiency of the proposed framework to enhance its practical viability, particularly through the incorporation of physics-informed neural networks for accelerated computation and potential real-time implementation in the configuration control of flexible space tethers.

(ii) Extend the proposed framework to the analysis of electric sail and solar sail systems, thereby broadening its applicability to a wider class of large-scale

flexible space structures.

(iii) Generalize the computational control framework to encompass a broader category of flexible dynamical systems beyond flexible tethers, with the objective of establishing a more universal control methodology for distributed-parameter and highly coupled nonlinear systems.

(iv) Develop an AI-enabled computational control framework through the integration of reinforcement learning and physics-informed neural networks, with the aim of achieving more adaptive, efficient, and autonomous control of complex flexible space systems.

(v) Once the computational efficiency of the proposed framework is further improved, experimental validation of the computational controller will constitute an important direction for future research. Ground-based experiments using an air-bearing platform would provide a practical means of evaluating the controller's performance, robustness to modeling uncertainties, and effectiveness in suppressing tether oscillations under realistic disturbance conditions.

Bibliography

[1] V. Aslanov, A. Ledkov, Dynamics of tethered satellite systems, Elsevier, 2012.

[2] K.E. Tsiolkovsky, Gryozy o Zemle i Nebe (Dreams of Earth and Sky), Arkhiv Akademii Nauk SSSR, Moscow, 1895. (Reprinted by USSR Academy of Sciences, 1959).

[3] Y.N. Artsutanov, V Kosmos na Elektrovoze (Into Space by Funicular), Komsomolskaya Pravda (1960).

[4] G. Colombo, E.M. Gaposchkin, M.D. Grossi, G.C. Weiffenbach, The «Skyhook»: A shuttle-borne tool for low-orbital-altitude research, Meccanica 10 (1975) 3–20.

[5] G. Vontiesenhausen, Tethers in space: Birth and growth of a new avenue to space utilization, 1984.

[6] J.A. Carroll, Tether applications in space transportation, Acta Astronautica 13 (1986) 165–174.

[7] V.V. Beletskiĭ, E.M. Levin, Dynamics of space tether systems, Univelt Incorporated, 1993.

[8] Y. Chen, R. Huang, L. He, X. Ren, B. Zheng, Dynamical modelling and control of space tethers: a review of space tether research, Nonlinear Dynamics 77 (2014) 1077–1099.

[9] M. Cartmell, D. McKenzie, A review of space tether research, Progress in Aerospace Sciences 44 (2008) 1–21.

[10] P. Huang, F. Zhang, L. Chen, Z. Meng, Y. Zhang, Z. Liu, Y. Hu, A review of space tether in new applications, Nonlinear Dynamics 94 (2018) 1–19.

[11] S.G. Tragesser, H. San, Orbital maneuvering with electrodynamic tethers, Journal of Guidance, Control, and Dynamics 26 (2003) 805–810.

[12] A.F. Ferreira, R.V. Moraes, A.F. Prado, O.C. Winter, A mathematical study of the tethered slingshot maneuver using the elliptic restricted problem, Nonlinear Dynamics 102 (2020) 1585–1609.

[13] J. Liu, G. Li, Z.H. Zhu, M. Liu, X. Zhan, Automatic orbital maneuver for mega-constellations maintenance with electrodynamic tethers, Aerospace Science and Technology 105 (2020) 105910.

[14] H. Yang, C. Wang, H. Lu, A. Li, F. Pavel, Event-triggered sliding mode control of spinning tether system for fly-around observation, Aerospace Science and Technology (2025) 111197.

[15] R. Haiping, R. Zhong, L. Pengjie, Fuel-optimal deorbit scheme of space debris using tethered space-tug based on pseudospectral method, Chinese Journal of Aeronautics 34 (2021) 210–223.

[16] B. Yu, Z.H. Zhu, Out-of-plane chaotic motion and suppression for tethered tug-debris systems with thrust perturbation, Communications in Nonlinear Science and Numerical Simulation 123 (2023) 107273.

[17] P. Sun, C. Wang, H. Lu, A. Li, Y. Zabolotnovb, Adaptive robust fault-tolerant control of spinning tether system for space debris removal, Acta Astronautica 228 (2025) 191–203.

[18] L. Field, D. Bourabah, E.M. Botta, Online Estimation and Control of Tethered

Debris Using Tension and Feature Tracking, Journal of Guidance, Control, and Dynamics 48 (2025) 443–449.

[19] K.M. Martin, D.F. Landau, J.M. Longuski, Method to maintain artificial gravity during transfer maneuvers for tethered spacecraft, Acta Astronautica 120 (2016) 138–153.

[20] X. Gou, A. Li, H. Tian, C. Wang, H. Lu, Overload control of artificial gravity facility using spinning tether system for high eccentricity transfer orbits, Acta Astronautica 147 (2018) 383–392.

[21] H. Tian, A. Li, C. Wang, Finite time non-singular sliding mode control for spinning tether system with prescribed performance under artificial gravity mission, Advances in Space Research 71 (2023) 2467–2480.

[22] N.A. Pallotta, M.C. Bazzocchi, Optimization of tethered artificial gravity assists for capture about binary asteroids in the circular restricted three-body problem, Acta Astronautica 228 (2025) 285–294.

[23] Z. Zhang, H. Yang, B. Jiang, V. Cocquempot, Y. Cheng, Decentralised fault-tolerant control of tethered spacecraft formation: an interconnected system approach, IET Control Theory & Applications 11 (2017) 3047–3055.

[24] C. Luo, H. Wen, D. Jin, S. Xu, Dynamics of a flexible multi-tethered satellite formation in a Halo orbit with uncertain parameters, Communications in Nonlinear Science and Numerical Simulation 99 (2021) 105828.

[25] B. Yu, K. Ji, Z. Wei, D. Jin, In-plane global dynamics and ground experiment of a linear tethered formation with three satellites, Nonlinear Dynamics 108 (2022) 3247–3278.

[26] S. Li, Z. Zheng, Y. Wang, J. Yuan, An adaptive fault tolerant control method for electromagnetic formation spacecraft with external disturbances, Advances in Space Research 73 (2024) 6177–6193.

[27] B.C. Edwards, DESIGN AND DEPLOYMENT OF A SPACE ELEVATOR, Acta Astronautica 47 (2000) 735–744. https://doi.org/10.1016/S0094-5765(00)00111-9.

[28] G. Li, Z.H. Zhu, On libration suppression of partial space elevator with a moving climber, Nonlinear Dynamics 97 (2019) 2107–2125. https://doi.org/10.1007/s11071-019-05108-0.

[29] V.S. Aslanov, A double pendulum anchored at the surface of a moon below the L1 libration point: the impossibility of building a space elevator, Nonlinear Dynamics 113 (2025) 12959–12970. https://doi.org/10.1007/s11071-025-11071-w.

[30] G. Shi, Z.H. Zhu, Flexible-rigid dynamics and vibration suppression of slender structures on partial space elevator, Applied Mathematical Modelling 150 (2026) 116326. https://doi.org/10.1016/j.apm.2025.116326.

[31] C. Luo, H. Wen, D. Jin, T. Chen, H. Hu, Novel Partial Space Elevator via an Electrodynamic Tether for Cargo Transportation, Space: Science & Technology 5 (n.d.) 0287. https://doi.org/10.34133/space.0287.

[32] S. Yu, Dynamic Model and Control of Mass-Distributed Tether Satellite System, Journal of Spacecraft and Rockets 39 (2002) 213–218. https://doi.org/10.2514/2.3822.

[33] V.V. Sidorenko, A. Celletti, A “Spring–mass” model of tethered satellite systems: properties of planar periodic motions, Celestial Mechanics and Dynamical Astronomy 107

(2010) 209–231. https://doi.org/10.1007/s10569-010-9275-5.

[34] R. Qi, F. Yao, S. Lu, Z. Jiang, Stabilization of Tethered Tug–Debris System with Residual Liquid Fuel, Journal of Guidance, Control, and Dynamics 44 (2021) 880–888. https://doi.org/10.2514/1.G005676.

[35] B.S. Yu, Z.H. Zhu, Symmetric and asymmetric dynamics of a tethered satellite in nontypical planes, Acta Astronautica 202 (2023) 585–594. https://doi.org/10.1016/j.actaastro.2022.11.019.

[36] G. Li, Z.H. Zhu, Dynamic Modeling of Space Electrodynamic Tether System Using the Nodal Position Finite Element and Symplectic Integration, in: IMECE2014, Volume 4A: Dynamics, Vibration, and Control, 2014. https://doi.org/10.1115/IMECE2014-38568.

[37] X. Wang, J. Zhao, H. Wang, H. Song, Z. Luo, Q. Han, Dynamic modeling and simulation of rigid-flexible coupling cable system by absolute nodal coordinate formulation, Scientific Reports 12 (2022) 13558. https://doi.org/10.1038/s41598-022-17731-w.

[38] Y. Zhang, X. Jiang, Z. Bai, J. Guo, C. Wei, Dynamics and rebound behavior analysis of flexible tethered satellite system in deployment and station-keeping phases, Defence Technology 18 (2022) 509–523. https://doi.org/10.1016/j.dt.2021.04.007.

[39] S. Singh, M. Mastrogiuseppe, Multibody modelling of tether and capture system for dynamic simulations of In-Air Capturing, Acta Astronautica 218 (2024) 59–69. https://doi.org/10.1016/j.actaastro.2024.02.008.

[40] W. Gołębiowski, R. Michalczyk, M. Dyrek, U. Battista, K. Wormnes, Validated

simulator for space debris removal with nets and other flexible tethers applications, Acta Astronautica 129 (2016) 229–240. https://doi.org/10.1016/j.actaastro.2016.08.037.

[41] C. Lambert, M. Nahon, An Aerostat Positioning System with Cable Control, IFAC Proceedings Volumes 41 (2008) 779–784. https://doi.org/10.3182/20080706-5-KR-1001.00134.

[42] V.J. Modi, R.P. Pidgeon, Dynamics and control of a flexible tethered system with offset, Acta Astronautica 32 (1994) 255–265. https://doi.org/10.1016/0094-5765(94)90078-7.

[43] J. Kang, Z.H. Zhu, W. Wang, A. Li, C. Wang, Fractional order sliding mode control for tethered satellite deployment with disturbances, Advances in Space Research 59 (2017) 263–273. https://doi.org/10.1016/j.asr.2016.10.006.

[44] A.K. Yadav, B.S. Kushvah, Controlling the libration motion of tethered satellite system using sliding mode control scheme, AIP Conference Proceedings 2435 (2022) 020052. https://doi.org/10.1063/5.0083540.

[45] Y. Li, A. Li, C. Wang, Back-stepping sliding mode control for libration control of large swing angles of electrodynamic tether system, Advances in Space Research 72 (2023) 231–242. https://doi.org/10.1016/j.asr.2023.03.021.

[46] Y.-L. Kuo, Dynamics and control of a tethered satellite system based on the SDRE method, International Journal of Aerospace Engineering 2016 (2016) 3610507.

[47] Z. Ma, G. Sun, Adaptive sliding mode control of tethered satellite deployment with input limitation, Acta Astronautica 127 (2016) 67–75.

https://doi.org/10.1016/j.actaastro.2016.05.022.

[48] J. Kang, Z.H. Zhu, Hamiltonian formulation and energy-based control for space tethered system deployment and retrieval, Transactions of the Canadian Society for Mechanical Engineering 43 (2019) 463–470.

[49] G. Li, Z.H. Zhu, Estimation of flexible space tether state based on end measurement by finite element Kalman filter state estimator, Advances in Space Research 67 (2021) 3282–3293.

[50] J. Yang, G. Chen, M. Zhang, G. Li, J. Liu, Velocity Observer Design for Tether Deployment in Hamiltonian Framework, Aerospace 11 (2024) 1047.

[51] K. Nakanishi, H. Kojima, T. Watanabe, Trajectories of in-plane periodic solutions of tethered satellite system projected on van der Pol planes, Acta Astronautica 68 (2011) 1024–1030.

[52] G. Zhao, L. Sun, S. Tan, H. Huang, Librational characteristics of a dumbbell modeled tethered satellite under small, continuous, constant thrust, Proceedings of the Institution of Mechanical Engineers, Part G: Journal of Aerospace Engineering 227 (2013) 857–872.

[53] N. Ismail, M. Cartmell, Three dimensional dynamics of a flexible motorised momentum exchange tether, Acta Astronautica 120 (2016) 87–102.

[54] J. Theron Carter, M. Greene, Simulation of single tether systems, Simulation 58 (1992) 42–48.

[55] Z. Zhu, Dynamic modeling of cable system using a new nodal position finite

element method, International Journal for Numerical Methods in Biomedical Engineering 26 (2010) 692–704.

[56] A.A. Shabana, Dynamics of multibody systems, Cambridge university press, 2020.

[57] C. Yang, Y. Gong, An enhanced absolute nodal coordinate formulation for efficient modeling and analysis of long torsion-free cable structures, Applied Mathematical Modelling 123 (2023) 406–429.

[58] F. Sun, Z. Zhu, M. LaRosa, Dynamic modeling of cable towed body using nodal position finite element method, Ocean Engineering 38 (2011) 529–540.

[59] G. Li, G. Shi, Z.H. Zhu, Three-dimensional high-fidelity dynamic modeling of tether transportation system with multiple climbers, Journal of Guidance, Control, and Dynamics 42 (2019) 1797–1811.

[60] C. Du, Z.H. Zhu, Dynamic characterization and sail angle control of electric solar wind sail by high-fidelity tether dynamics, Acta Astronautica 189 (2021) 504–513.

[61] Z.H. Zhu, B.H. Pour, A nodal position finite element method for plane elastic problems, Finite Elements in Analysis and Design 47 (2011) 73–77. https://doi.org/10.1016/j.finel.2010.09.008.

[62] Q. Zhang, Z.H. Zhu, Elastodynamic analysis of rotating solids by novel nodal position finite element method, European Journal of Mechanics-A/Solids 109 (2025) 105478.

[63] F. Yao, C. Li, Z.H. Zhu, Advanced 3D Hamiltonian nodal position finite element method for nonlinear dynamic analysis of rotating solids, Computers & Structures 307

(2025) 107634.

[64] L. Hongshi, Y. Hang, W. Changqing, L. Aijun, Nonlinear deformation and attitude control for spinning electrodynamic tether systems during spin-up stage, Nonlinear Dynamics 112 (2024) 7011–7027.

[65] C. Du, Z.H. Zhu, C. Wang, A. Li, T. Li, Evaluation of E-sail parameters on central spacecraft attitude stability using a high-fidelity rigid-flexible coupling model, Astrodynamics 8 (2024) 271–284.

[66] E. Netzer, T.R. Kane, Estimation and control of tethered satellite systems, Journal of Guidance, Control, and Dynamics 18 (1995) 851–858.

[67] G. Li, Z.H. Zhu, S. Meguid, Libration and transverse dynamic stability control of flexible bare electrodynamic tether systems in satellite deorbit, Aerospace Science and Technology 49 (2016) 112–129.

[68] R. Zhong, Z. Z. H., Dynamic Analysis of Deployment and Retrieval of Tethered Satellites using a Hybrid Hinged-Rod Tether Model, International Journal of Aerospace and Lightweight Structures (IJALS) 01 (2011) 239. https://doi.org/10.3850/S2010428611000146.

[69] G. Shi, G. Li, Z. Zhu, Z.H. Zhu, A virtual experiment for partial space elevator using a novel high-fidelity FE model, Nonlinear Dynamics 95 (2019) 2717–2727. https://doi.org/10.1007/s11071-018-4718-8.

[70] P. Williams, Electrodynamic Tethers Under Forced-Current Variations Part II: Flexible-Tether Estimation and Control, Journal of Spacecraft and Rockets - J

SPACECRAFT ROCKET 47 (2010) 320–333. https://doi.org/10.2514/1.45733.

[71] G. Fang, Y. Zhang, P. Huang, F. Zhang, State estimation of double-pyramid tethered satellite formations using only two GPS sensors, Acta Astronautica 180 (2021) 507–515. https://doi.org/10.1016/j.actaastro.2020.12.043.

[72] G. Li, Z.H. Zhu, Model predictive control for electrodynamic tether geometric profile in orbital maneuvering with finite element state estimator, Nonlinear Dynamics 106 (2021) 473–489. https://doi.org/10.1007/s11071-021-06869-3.

[73] G. Fang, Y. Zhang, P. Huang, F. Zhang, State estimation of a three-inline space tethered system with geometric constraints, Advances in Space Research 69 (2022) 1550–1563. https://doi.org/10.1016/j.asr.2021.11.003.

[74] Q. Zhang, E.G. Asri, Z.H. Zhu, Space tether system state estimation using distributed fibre optical strain measurement, inverse finite element method and Kalman filter, Acta Astronautica 211 (2023) 435–446. https://doi.org/10.1016/j.actaastro.2023.06.020.

[75] A.A. Teik Hong, R. Varatharajoo, Y.-C. Chak, Review of deployment controllers for space tethered system, Advances in Space Research 75 (2025) 3933–3949. https://doi.org/10.1016/j.asr.2024.11.061.

[76] W. Chen, F. Zhang, Strict finite-time sliding mode control for a tethered space net robot, Chinese Journal of Aeronautics 36 (2023) 325–335.

[77] Q. Zhang, Z.H. Zhu, Computational control framework for tethered space systems using finite element method, Acta Astronautica 228 (2025) 595–606.

https://doi.org/10.1016/j.actaastro.2024.12.013.

[78] G. Xing-wang, L. Ai-jun, G. Yang-yang, W. Chang-qing, Fractional order attitude stability control for sub-satellite of tethered satellite system during deployment, Applied Mathematical Modelling 62 (2018) 272–286.

[79] C. Luo, T. Chen, H. Wen, D. Jin, Learning-based control for deployment and retrieval of a spinning tethered satellite formation system, Acta Astronautica 225 (2024) 788–800.

[80] G. Sun, Z. Zhu, Fractional-order tension control law for deployment of space tether system, Journal of Guidance, Control, and Dynamics 37 (2014) 2057–2062.

[81] X. Li, G. Sun, C. Xue, Fractional-order deployment control of space tethered satellite via adaptive super-twisting sliding mode, Aerospace Science and Technology 121 (2022) 107390.

[82] X. Zhang, F. Wu, M. Liu, X. Chen, Fractional-order robust fixed-time sliding mode control for deployment of tethered satellite, Acta Astronautica 209 (2023) 172–178.

[83] J. Kang, Z.H. Zhu, L.F. Santaguida, Analytical and experimental investigation of stabilizing rotating uncooperative target by tethered space tug, IEEE Transactions on Aerospace and Electronic Systems 57 (2021) 2426–2437.

[84] B. Su, F. Zhang, P. Huang, Stability analysis and RBF neural network control of second-order nonlinear satellite system, IEEE Transactions on Aerospace and Electronic Systems 59 (2023) 4575–4589.

[85] G.T. Mase, R.E. Smelser, G.E. Mase, Continuum mechanics for engineers, CRC

press, 2009.

[86] J.N. Reddy, An introduction to the finite element method, in: Dynamics of Earth's Fluid System, CRC Press, 2026: pp. 199–226.

[87] E.L. Wilson, A. Ibrahimbegovic, Use of incompatible displacement modes for the calculation of element stiffnesses or stresses, Finite Elements in Analysis and Design 7 (1990) 229–241. https://doi.org/10.1016/0168-874X(90)90034-C.

[88] J.H. White, Self-linking and the Gauss integral in higher dimensions, University of Minnesota, 1968.

[89] J. Wang, J.-K. Chen, S. Liao, An explicit solution of the large deformation of a cantilever beam under point load at the free tip, Journal of Computational and Applied Mathematics 212 (2008) 320–330. https://doi.org/10.1016/j.cam.2006.12.009.

[90] H. Kim, H. Hee Yoo, J. Chung, Dynamic model for free vibration and response analysis of rotating beams, Journal of Sound and Vibration 332 (2013) 5917–5928. https://doi.org/10.1016/j.jsv.2013.06.004.

[91] G. Wei, P. Lardeur, F. Druesne, A new solid-beam approach based on first or higher-order beam theories for finite element analysis of thin to thick structures, Finite Elements in Analysis and Design 200 (2022) 103655. https://doi.org/10.1016/j.finel.2021.103655.

[92] R. Azzara, M. Filippi, E. Carrera, Geometrically nonlinear transient analyses of rotating structures through high-fidelity models, Composite Structures 343 (2024) 118265.

[93] J. CHUNG, H.H. YOO, DYNAMIC ANALYSIS OF A ROTATING

CANTILEVER BEAM BY USING THE FINITE ELEMENT METHOD, Journal of Sound and Vibration 249 (2002) 147–164. https://doi.org/10.1006/jsvi.2001.3856.

[94] T. Inoue, Y. Ishida, T. Kiyohara, Nonlinear Vibration Analysis of the Wind Turbine Blade (Occurrence of the Superharmonic Resonance in the Out of Plane Vibration of the Elastic Blade), Journal of Vibration and Acoustics 134 (2012). https://doi.org/10.1115/1.4005829.

[95] B. Zhang, H. Ding, L.-Q. Chen, Super-harmonic resonances of a rotating pre-deformed blade subjected to gas pressure, Nonlinear Dynamics 98 (2019) 2531–2549. https://doi.org/10.1007/s11071-019-05367-x.

[96] B. Valverde-Marcos, B. Muñoz-Abella, P. Rubio, L. Rubio, Influence of the rotation speed on the dynamic behaviour of a cracked rotating beam, Theoretical and Applied Fracture Mechanics 117 (2022) 103209. https://doi.org/10.1016/j.tafmec.2021.103209.

[97] G. Li, Multibody Dynamics and Control of Tethered Spacecraft Systems, (2019).

[98] F. Gao, J. Li, F. Dong, Y. Ji, G. Sun, Dynamic modeling and control strategy for tethered satellite systems in orbital debris management, Acta Mechanica Sinica 41 (2025) 524262.

[99] G. Li, Z.H. Zhu, Multiphysics finite element modeling of current generation of bare flexible electrodynamic tether, Journal of Propulsion and Power 33 (2017) 408–419.

[100] N. Pavlis, S. Kenyon, J. Factor, S. Holmes, Earth gravitational model 2008, in: Society of Exploration Geophysicists, 2008: pp. 761–763.

[101] J. Picone, A. Hedin, D.P. Drob, A. Aikin, NRLMSISE-00 empirical model of the atmosphere: Statistical comparisons and scientific issues, Journal of Geophysical Research: Space Physics 107 (2002) SIA-15.

[102] J. Chung, G. Hulbert, A time integration algorithm for structural dynamics with improved numerical dissipation: the generalized-α method, (1993). https://asmedigitalcollection.asme.org/appliedmechanics/article-abstract/60/2/371/423023 (accessed April 1, 2026).

[103] W. Kabsch, A solution for the best rotation to relate two sets of vectors, Foundations of Crystallography 32 (1976) 922–923.

[104] C.A. Felippa, B. Haugen, A unified formulation of small-strain corotational finite elements: I. Theory, Computer Methods in Applied Mechanics and Engineering 194 (2005) 2285–2335.

[105] E.J. Haug, Computer-aided kinematics and dynamics of mechanical systems, Volume II: Modern Methods, (2022).

[106] J. Simo, N. Tarnow, The discrete energy-momentum method. Conserving algorithms for nonlinear elastodynamics, Zeitschrift Für Angewandte Mathematik Und Physik ZAMP 43 (1992) 757–792.

[107] J. Simo, N. Tarnow, M. Doblaré, Non-linear dynamics of three-dimensional rods: Exact energy and momentum conserving algorithms, International Journal for Numerical Methods in Engineering 38 (1995) 1431–1473.

[108] C. Liu, W. Wang, J. Kang, Z.H. Zhu, Spin deployment of Hub-Spoke tethered

satellite formation with sliding mode tether tension control, Advances in Space Research 71 (2023) 2509–2520. https://doi.org/10.1016/j.asr.2022.11.001.

[109] I. Floris, J.M. Adam, P.A. Calderón, S. Sales, Fiber Optic Shape Sensors: A comprehensive review, Optics and Lasers in Engineering 139 (2021) 106508. https://doi.org/10.1016/j.optlaseng.2020.106508.

[110] M. Gherlone, P. Cerracchio, M. Mattone, M. Di Sciuva, A. Tessler, An inverse finite element method for beam shape sensing: theoretical framework and experimental validation, Smart Materials and Structures 23 (2014) 045027.

[111] H.K. Khalil, M. Minor, Nonlinear control, (2015).

[112] R. Hermann, A. Krener, Nonlinear controllability and observability, IEEE Transactions on Automatic Control 22 (2003) 728–740.

[113] P. Lakshmanan, V. Modi, A. Misra, Dynamics and control of the tethered satellite system in the presence of offsets, Acta Astronautica 15 (1987) 1053–1057.

[114] J.R. Ellis, Modeling, dynamics, and control of tethered satellite systems, (2010).

[115] T. Meng, W. He, Lyapunov-based control of a tethered satellite system, IET Control Theory & Applications 10 (2016) 956–964.

[116] S. Haghighat, H.H. Liu, J.R. Martins, Model-predictive gust load alleviation controller for a highly flexible aircraft, Journal of Guidance, Control, and Dynamics 35 (2012) 1751–1766.

[117] D.Q. Mayne, J.B. Rawlings, C.V. Rao, P.O. Scokaert, Constrained model predictive control: Stability and optimality, Automatica 36 (2000) 789–814.

[117] J.B. Rawlings, D.Q. Mayne, M.M. Diehl, Model predictive control: theory, computation, and design, Nob Hill Publishing Madison, WI, (2020).

[119] A.K. Misra, Dynamics and control of tethered satellite systems, Acta Astronautica 63 (2008) 1169–1177.

[120] G. Li, Z. Zhu, Long-term dynamic modeling of tethered spacecraft using nodal position finite element method and symplectic integration, Celestial Mechanics and Dynamical Astronomy 123 (2015) 363–386.

[121] H. Ding, X. Yin, Z.H. Zhu, L. Zhang, A high accurate hamiltonian nodal position finite element method for spatial cable structures undergoing long-term large overall motion, Communications in Nonlinear Science and Numerical Simulation 70 (2019) 203–222.

[122] F.J. Sun, Z.H. Zhu, M. LaRosa, Dynamic modeling of cable towed body using nodal position finite element method, Ocean Engineering 38 (2011) 529–540. https://doi.org/10.1016/j.oceaneng.2010.11.016.

[123] E.D. Sontag, Input to state stability: Basic concepts and results, in: Nonlinear and Optimal Control Theory: Lectures given at the CIME Summer School Held in Cetraro, Italy June 19–29, 2004, Springer, 2008: pp. 163–220.